



## The nearby SuperNova Factory: from CCDs to cosmology.

Emmanuel Gangler

### ► To cite this version:

Emmanuel Gangler. The Nearby SuperNova Factory: From CCDs to Cosmology. Cosmology and Extragalactic Astrophysics [astro-ph.CO]. Claude Bernard University - Lyon I, 2011. <tel-00854994>

HAL Id: tel-00854994

<https://tel.archives-ouvertes.fr/tel-00854994>

Submitted on 28 Aug 2013

HAL is a multi-disciplinary open access archive for the deposit and dissemination of scientific research documents, whether they are published or not. The documents may come from teaching and research institutions in France or abroad, or from public or private research centers.

The multidisciplinary open archive HAL is intended for the deposit and dissemination of research-level scientific documents, published or not, from French or foreign educational and research establishments, public or private laboratories.

University of Lyon, F-69622, France;  
University of Lyon 1, Villeurbanne; CNRS/  
IN2P3, Institute of Nuclear Physics of Lyon.

Memory for obtaining a

## **Authorization to direct research**

Presented by

**Mr. Emmanuel GANGER**

---

## **The nearby SuperNova Factory: from CCDs to cosmology.**

---

To be defended on September 29, 2011 before the jury composed of:

Mr. Réza Ansari Rapporteur Mr. Pierre  
Astier Rapporteur Mr. Jules Gascon Mr.  
Jean Orloff Mr. James  
Rich Mr. Gérard Smadja

Rapporteur



*“Dicebat Bernardus Carnotensis nos esse quasi  
nanos, gigantium humeris incidentes, ut possi-  
mus plura eis et remotiora videre, non utique  
proprii visus acumine, aut eminentia corporis,  
sed quia in altum subvehimur et extollimur  
magnitudine gigantea. »*

John of Salisbury



# Thanks

As I finish writing this booklet, it will be difficult for me to pay tribute by name to all those who have, in one way or another, contributed to making it possible, whether they are the friends who once lent me their sofa bed, the colleagues with whom the research is carried out on a daily basis, all those who have in one way or another advised or inspired me. Just as a tree can be enough to symbolize a forest, behind the few people whose names will appear below there are many others who hide in the shadows.

My first thoughts are for my parents and my teachers, for all those who educated me, from the smallest sections to the largest: the task of awakening minds is indeed one of the noblest there is, and it would be criminal not to pay tribute to the dedication of all these teachers, a task often thankless and unfortunately less and less valued by our society. From Madame Tolmer, elementary school teacher to Pierre Astier, thesis director, by way of Jean-Paul Bouchoux, and so many others, please be wholeheartedly thanked for your precious work.

However, there would be no teachers without students; all those I have taught, all those I have had the pleasure of supervising, or rather of directing according to the current academic newspeak , have contributed their little stone to this accreditation. Their names are Fatima, Stéphane, Nathalie P., Olivier, Léonie... and all of them have given me something in return. Among them, three deserve special mention: Satya Gontcho, who made a strong impression on me at the dawn of his university studies and to whom I wish the best for his career as a future researcher, Nathalie Blanc, who showed me that supervising a doctoral student was not always an easy exercise, and Nicolas Chotard, who showed me, on the contrary, that it could be a real pleasure, and who provided a mass of work that I would have been incapable of taking on alone. I will never thank him enough.

My thanks also go to my close colleagues, to all those with whom I have shared moments in and outside of research, whether they are former members of the LPNHE neutrino team, or at IPNL in the Heavy Ion team and of course in the Supernova group. There would be far too much to say and things far too personal to fully pay tribute to them. I share with some of them almost 10 years of joint research, as is the case for Yannick Copin and Gérard Smadja, historical members and true pillars of the group, and whose scientific level as well as ardor made the creation of this group a success. I have known others for even longer, like Alain Castera or the great Duduche. What can I say, except that I have a thought of course for the doctoral students who are with us or have already left, from Sébastien Bongard to Mickaël Rigault via Clément Buton, as well as for all the post-docs who too often only pass through, Gaelle Boudoul, Ludovic Saugé, and of course Rui Pereira, to whom the entire collaboration owes a great deal.

Beyond my close colleagues, I owe a lot to all those who worked for the SNfactory collaboration, whether at CRAL, LBL or LPNHE, as well as to all the French supernovists. Even if the relationships between institutes are not always obvious, the emulation and

## THANKS

---

Scientific competitions are highly stimulating, and I consider many of them friends as well as colleagues.

Finally, without the unwavering support of Bernard Ille, director of IPNL, I would certainly not be writing these lines: I owe him a great deal, as well as to the entire laboratory. Certainly, when I first set foot there, my first reaction, upon seeing the entrance hall falling into disrepair, was: "I absolutely do not want to be assigned here ." You, colleagues at IPNL who are reading these lines, secretary, librarian, technician, engineer, researcher, teacher, know that you quickly convinced me that this apprehension was unjustified, and that the long road we have traveled together was worth it. And for those who are not part of this laboratory, they should be content to know that the hall has recently been repainted, which proves that the AERES is finally useful!

Research is a big family, and over the course of my career I have been able to forge contacts and connections, have fruitful and intelligent discussions with many colleagues from other laboratories, particularly during my time at the commission, and now at the LPC. This list would be far too long to compile; I only hope that we will be given opportunities to interact again, and for a long time to come. Among these, I would like to warmly thank those who kindly agreed to be part of the jury, and in particular the reviewers for their careful reading.

But the family I want to think about now is the more modest one, who supported me during the few months I was putting this manuscript into shape and the long years when I sometimes came home a little late. Hélène, Gabriel and Félix, it is now time for me to take care of you too, but that is another story, and one that will be told another time.

# Table of Contents

<b>Preamble</b>	<b>1</b>
<b>1 Type 1a Supernovae: An Observable for Cosmology</b>	<b>3</b>
1.1 The Standard Candle Method.	3
1.1.1 Scale of distances in the Universe.	4
1.1.2 BA in cosmology.	7
1.2 The Supernova Object	9
1.2.1 Progenitor	9
1.2.2 Explosion	12
1.2.3 Standardization	13
Contributions	15
<b>2 Nearby Supernova Factory</b>	<b>17</b>
2.1 Scientific objective	18
2.2 Search for supernovae	19
2.3 Spectrophotometry: the SNIFS instrument	22
2.4 Data collection	25
2.4.1 The various types of poses.	25
2.4.2 Instrument operation.	27
2.4.3 Online data quality.	28
2.5 Data Reduction	29
2.5.1 Image processing.	29
2.5.2 Reconstruction of the cube.	30
2.5.3 Extracting the stream	31
2.5.4 Calibration	33
2.5.5 Galactic Subtraction	33
2.5.6 Analysis of light curves.	33
2.5.7 Data quality	36
Contributions	39
<b>3 Use and implementation of CCDs for spectrography</b>	<b>41</b>
3.1 General principle of a CCD sensor.	42
3.1.1 Signal formation	42
3.1.2 Hardware implementation	43
3.2 Reception and qualification of SNIFS CCDs	45
3.3 Instrumental signatures and preprocessing algorithm	45
3.3.1 Pedestal	45
3.3.2 Noise and playback artifacts	46

**TABLE OF CONTENTS**


---

3.3.3 Gain .....	47
3.3.4 Cosmetic defects .....	50
3.3.5 Charge transfer efficiency .....	52
3.3.6 Bias .....	54
3.3.7 Dark current .....	55
3.3.8 Uniformity .....	58
3.3.9 Remanence .....	61
3.3.10 Cosmic .....	61
3.3.11 (No)-Linearity .....	63
Contributions .....	65
<b>4 Analysis of spectral variability</b>	<b>67</b>
4.1 Automatic calculation of indicators .....	68
4.2 Spectral indicators .....	71
4.2.1 Silicon lines .....	71
4.2.2 Calcium Lines .....	74
4.2.3 Principal component analysis .....	76
4.3 The maximum color law .....	79
4.3.1 Color law or extinction law .....	79
4.3.2 Calculation of magnitudes .....	81
4.3.3 Corrections by intrinsic parameters . 4.3.4 color law .....	82
4.3.5 Results .....	85
Contributions .....	86
<b>In conclusion</b>	<b>87</b>
<b>Annexes</b>	<b>91</b>
<b>A Other works</b>	<b>91</b>
A.1 NOMAD .....	91
A.1.1 Reconstruction .....	91
A.1.2 Analysis .....	92
A.2 Heavy Ions .....	92
A.2.1 ALICE .....	92
A.2.2 NA60 .....	93
A.3 ToMuVol .....	94
<b>Other contributions</b>	<b>95</b>
<b>List of figures</b>	<b>97</b>
<b>List of tables</b>	<b>99</b>
<b>References</b>	<b>101</b>

# Preamble

Notwithstanding the stylistic figure imposed by the academic exercise that constitutes this work, which would like to present a professional and intellectual career in a teleological manner, the career of a researcher is not a long, quiet river. Despite a natural injunction to dig the same furrow in order to know the smallest nuggets and the smallest pitfalls until having exhausted its substance, it is made of chance, sudden hopes, accidents along the way, and diversions of all kinds. After a thesis at the LPNHE spent chasing plump neutrinos, extended by a year thanks to the institution that was the National Service in Cooperation, the vagaries of the assignment to the CNRS, confused by the learned apothecary calculations of various directions, led me to the IPNL in the heavy ions group, on a theme quite far from my concerns. Young, anxious to respect a sort of moral contract whose terms were nevertheless biased, I therefore got involved for four years in the liberation of quarks from their condensates or rather in various instrumental devices supposed to observe it, before taking advantage of the impromptu creation of a group dedicated to the observation of supernovae for cosmological purposes to return to my original aspirations. That was in 2001, and I'm still working on it.

The vagaries of existence were to remind me of their presence in 2006, however, the year I moved to Clermont-Ferrand for family reasons. There was no longer any question of wasting the know-how acquired over the years by pursuing new problems, so I continued to maintain the IPNL with my assiduity while forging links with the LPC in order to find sufficient connivance there to be able to pursue work of cosmological interest. However, I needed an anchor in one of the laboratory's projects, a sort of ritual intended to show my credentials, and the opportunity to contribute to a muography experiment of the Puy de Dôme having presented itself in 2009, I began to collaborate on this project alongside my initial investigations.

In this context, reporting on the various topics I have been involved in would have led to a motley, even indigestible juxtaposition of facts, questions, and various contributions. In order to maintain consistency, I have therefore preferred to focus in this document on the theme that defines me the most, the one that is the continuation of my childhood dreams of looking at the stars: observational cosmology.

However, the following will not be a comprehensive review of all the work carried out, but rather a journey through it, from the cosmological motivations and questions about supernovae, which will be the subject of the first chapter, the description of the SNfactory experiment and the general scheme of data reduction, discussed in the following chapter, with a more detailed presentation of the instrument's CCD sensors in a chapter dedicated to them, to the first results of the analysis in the last chapter. At the end of each of these chapters, a list of the related work will be gathered. However, I will not entirely ignore the other activities mentioned in this preamble, a brief list of which can be consulted in the appendix.

**PREAMBLE**

---

# Chapter 1

## Type 1a Supernovae: a observable for cosmology

### Summary

1.1 The standard candle method . . . . .	3
1.1.1 Scale of distances in the Universe. . . . .	4
1.1.2 BA in cosmology. . . . .	7
1.2 The Supernova Object . . . . .	9
1.2.1 Progenitor. . . . .	9
1.2.2 Explosion . . . . .	12
1.2.3 Standardization. . . . .	13
Contributions . . . . .	15

### 1.1 The standard candle method

Determining distances in the Universe is a fantasy of the observer, in fact, the dimension depth is only accessible by calculation, the primary data provided to us being generally in two dimensions, convertible into spherical coordinates with some calculations of astrometry. History has taught us, however, to be wary of hasty judgments made on this third dimension, the Universe having not stopped expanding since the determinations of Aristarchus of Samos in the 3rd century BC who placed the sun at 19 Earth-Moon radii ([Heath, 1913](#)). Indeed, this measurement which gave an approximate scale of the distance of the various planets was the origin of Tycho Brahe's original geocentric mode system which does not could admit that the Earth was moving because this should have given rise to an observable parallax for the stars of the fixed sphere. Bradley's observations in the 18th century ended to prove that it was indeed the Earth that was moving, and therefore that the stars were indeed further than the dimensions of the solar system, parallax measurements in the following century by Bessel having made it possible to determine the distance of the closest of them to some 105 times the distance between Earth and the Sun, or several light years. A new revolution in size of the Universe took place in the 1920s when Hubble demonstrated that the stars in our Way Milky Way visible in a distinct way, were representative only of a very local universe, and that galaxies were in fact clusters of stars located millions of light years away, and whose speed of removal was relative to their distance: the idea of an expanding universe was born. Also, the current image of a universe constrained by an origin of time, if it represents the state

CHAPTER 1. TYPE 1A SUPERNOVAE: AN OBSERVABLE FOR COSMOLOGY

---

of art regarding the standard model of the Big Bang may one day be challenged , even if we currently lack the observational means to test ages much younger than primordial nucleosynthesis or multiverse scenarios such as those implied by the chaotic inflation theories of [Linde \(1983\)](#).

### 1.1.1 Scale of distances in the Universe

Since observational cosmology is concerned with the macroscopic properties of the Universe, we will need to determine distances on scales where the paradigm of a homogeneous and isotropic universe applies, which can be defined as several times the comoving radius of the sound horizon at the time of freezing of baryon acoustic oscillations, or 153.3 Mpc ([Komatsu et al., 2009; Percival et al., 2010](#)). To define a distance on such scales, several probes will have to be used, each adapted to a particular measurement regime. We will not attempt to be exhaustive here on these methods; the interested reader will find a review in [Freedman and Madore \(2010\)](#), but only to give an overview of the problems that may concern the measurement of the distances of supernovae.

The physical phenomenon that allows us to determine distances on the scale of the solar system is the invariance of the speed of light. This allows us to define the meter from the second, itself defined to within  $10^{-14}$ . Conversion to distance in the solar system is done by radar echo measurements and by tracking satellites, which constitute as many witness masses as defined in general relativity. This allows distances to be determined at the solar system level with great precision: thus, the Astronomical Unit is defined to within only 3 meters, or a relative precision of  $10^{-11}$  [USNO et al. \(2011\)](#).

This accuracy is largely sufficient when using the motions of the Earth or probes to determine the distances of nearby stars by the parallax method. The best catalog currently available is that of Hipparcos, which provides a median accuracy of 0.8 mas ([Perryman et al., 1997; van Leeuwen, 2007](#)) and can go down to 0.1 mas for some of the brightest objects. Thus, we can have a geometric measurement for the nearby Universe down to distances of the order of a kiloparsec. The launch in 2012 of the Gaia satellite, which will operate on the same principle as Hipparcos, should make it possible to improve the precision obtained by one to two orders of magnitude, down to a few tens of mas ([Perryman et al., 2001](#)).

While the distances of nearby galactic objects can be determined by measuring their parallax, other methods are required to measure more distant objects.

One of the most widespread generic methods is that of standard candles. Given an object of luminosity L, it is possible to determine its distance, called luminosity, by measuring the flux F received from it:

$$F = \frac{L}{4\pi d^2} \quad (1.1)$$

The problem is then to find objects that are both bright enough to be observed from a distance, and whose brightness is identical from one object to another, or at least can be determined by empirical corrections. In the order of accessible distances, this method covers the end of the red giant branch (TRGB) ([Lee et al., 1993; Rizzi et al., 2007, and references therein](#)) the Cepheids,<sup>1</sup> (see e.g. [Madore and Freedman, 1991; Freedman et al.,](#)

<sup>1</sup>Abundant literature naturally accompanies each of these indicators. The references indicated here are far from exhaustive; we have simply distinguished a few steps, which allow the curious reader to access a more complete vision through the included references and the network of citations.

## 1.1. THE STANDARD CANDLE METHOD

---

2001; Sandage et al., 2006), Type II supernovae (Schmidt et al., 1992), Type Ia supernovae (or SNIa, detailed below), and GRBs (Bloom et al., 2003). However, not all of these indicators have the same precision, and only those for which reproducibility is ensured by a physical mechanism that also allows the first order of variability to be constrained are currently usable: the standardization of Type II supernovae or GRBs is far from being competitive in cosmology measurements, even if it would open the way to interesting ranges in redshift.

The standardization of objects often follows a similar pattern, with details depending on the object in question. The luminosity of red giants is constrained by the ignition time of the star's helium core: since the core is formed from a gas of degenerate electrons, only the ignition temperature of the reaction is taken into account, which is itself constrained by nuclear physics. Thus, the only corrections to be made to the luminosity will be the mass of the envelope and metallicity effects. Cepheid physics, on the other hand, constrains the period-luminosity-color relationship, or Leavitt's law (Madore and Freedman, 1991) : in fact, the Stefan-Boltzman law links luminosity to the radius and temperature of the object. The radius defines the natural pulsation, and therefore the period of oscillation of objects, while the temperature is measured by their color. Taking into account the narrow region of parameter space that allows instability to develop in stars burning their helium, a first-order period-luminosity relationship emerges, with a small color correction to be made. This first-order view must nevertheless be qualified because of metallicity effects, which affect the constants involved in the correction relationship. Finally, regarding SNIa, the underlying physical principle is the existence of the Chandrasekhar mass limit for degenerate-core objects, which constrains the initial conditions of the explosion and therefore the quantity of 56Ni produced, which can be reconstructed by measuring the light curve—we will detail this process later. Metallicity effects are expected to intervene at second order on the standardization relationships, but they have not been formally detected to date.

For the three objects considered, we therefore obtain the following general correction scheme: effects related to the variabilities permitted by physical laws must be taken into account, under which metallicity is a second-order phenomenon likely to cause measurement bias, and which must therefore be controlled. However, the situation is complicated by the presence of dust on the line of sight, which requires additional correction. Indeed, absorption by these causes a reduction in the measured flux, as well as reddening because absorption is greater in the blue. The law of Cardelli et al. (1989) allows to relate the color difference with respect to a non-extinguished object,  $E(B - V)$  to the total absorption AV as a function of a single parameter,

, in

$$RV = \frac{AV}{E(B - V)} \quad (1.2)$$

Knowing the average value of  $RV = 3.1$ , measured in the Milky Way, it is therefore possible in principle to correct for dust extinction. However, this requires a reference point for the colors, and also either to constrain RV or to assume that its value in other galaxies is similar to that measured in the Milky Way. This color correction is one of the dominant sources of uncertainty in the candle method.

standard, especially for SNIa.

However, it is not enough to know how to reduce to an average brightness to obtain a distance scale: it is also necessary to have sufficient statistics of objects whose distance is determined by another method which defines the zero point. As regards

## CHAPTER 1. TYPE 1A SUPERNOVAE: AN OBSERVABLE FOR COSMOLOGY

---

Cepheids, the Large Magellanic Cloud has long been the primary distance standard, and has served as a point of comparison for more than 21 different techniques (Benedict et al., 2002). Its different metallicity from that of the Milky Way and other spiral galaxies, however, makes it a poor standard, and the most precise measurement to date (Riess et al., 2011) actually uses the galaxy NGC 4258 as the primary standard. This active galaxy, 7.2 Mpc away, indeed harbors at its center an accretion disk that appears edge-on and has maser emission linked to the 616  $\text{\AA}$  523 radio transition of water. Measuring the Doppler shift using VLBI observations of this emission and monitoring it over a period of about ten years allows us to model the geometry of the accretion disk. This leads to a precision of 3% on its distance (Humphreys et al., 2008), a precision that is currently limiting for the determination of the Hubble constant.

Type Ia supernovae do not have such a geometrically accessible zero point; an absolute measurement of their distances, or what amounts to the same thing, their absolute magnitude, must pass through a secondary reference: they are supernova host galaxies whose distance can also be determined using Cepheids. The distances of eight of these galaxies were thus determined with a precision of 2% relative to NGC 4258, which, taking into account the uncertainty in the corrected mean magnitude of the supernovae and that in the distance of the anchor, makes it possible to determine an absolute distance scale to within 4.1%.

However, using Cepheids as Type Ia supernovae only allows the determination of the distance of certain objects: for example, only 59 galaxies have a distance estimate made using Cepheids. For spiral galaxies, the so-called Tully-Fischer method, which uses an empirical relationship between the rotational velocity plateau and the luminosity of the object, allows the determination of distances up to a redshift of 0.04 (Tully and Fisher, 1977; Courtois et al., 2011).

However, the most commonly used distance indicator is the redshift  $z$  induced by the expansion of the universe. This is only an indirect measure based on the measurement of the Hubble constant and a cosmological model at large distances, and which allows the conversion of recession velocities into distance. The most precise direct measurement of the latter is based on the distance estimate made by Riess et al. (2011), and gives  $H_0 = 74.8 \pm 3.1 \text{ km s}^{-1}\text{Mpc}^{-1}$ . Observation of the cosmic microwave background provides an independent estimate of the Hubble constant, but requires a cosmological assumption: the results of the first 5 years of WMAP in the framework of the  $\Lambda$ CDM model provide  $\text{km s}^{-1}\text{Mpc}^{-1}$  (Dunkley et al., 2009; Komatsu et al., 2009). While this result is similar  $H_0 = 71.9 \pm 2.7^{+2.6}_{-2.7}$  to that provided by the direct measurement, it depends on the cosmological assumption used and in the more general case of a curved universe, the additional measurement of BAOs and SNIa must be used to constrain the value of  $H_0$ .

The scale of distance measurement in the universe can therefore be summarized as follows: in our Milky Way, precision will be obtained by parallax measurements; in the nearby Universe, the greatest number of determinations will be provided by the Tully-Fisher method, while the best precision will be given by measurements of red giants, Cepheids, or that of the rare galaxies with maser emission. Finally, at greater distances, only the measurement of the redshift is generally accessible. In this context, the observation of SNIa takes on its full interest: it is one of the rare measurements that is both precise and accessible on large scales, and which allows us to compare a distance measurement with the redshift, and thus to reconstruct the history of the expansion of the universe. Moreover, as we will see in the next section, the determination of the 0 point and therefore the anchoring to a scale determined by another method is not necessary to constrain the cosmological parameters.

---

 1.1. THE STANDARD CANDLE METHOD
 

---

**1.1.2 BA in Cosmology**

Copeland et al. (2006) having made an extensive review on the subject, we will limit ourselves to summarizing the main points. The approximation in which cosmological studies are placed is that of the homogeneous and isotropic universe, which corresponds to scales for which the perturbations linked to the structures are averaged. The Friedman-Lemaître equations applied to the Robertson-Walker metric make it possible to determine the evolution of the scale parameter  $a(t)$  as a function of the various constituents of the universe, characterized by their equation of state  $p_i = w_i \rho_i$ . In some cases, it may be useful to use an effective equation of state  $p_i = w(z)$  that depends on the redshift,  $z$ . By writing the equation for the geodesic of a photon, it then becomes possible to relate the luminosity distance to the cosmological

$$\frac{dy}{dt} = \frac{1+z}{H_0 \sqrt{\bar{\gamma}_k + \frac{1}{2}S \bar{\gamma}_k^{1/2}}} \quad \text{if } \bar{\gamma}_k = 0$$

Or

$$dL = \frac{1+z}{H_0} dz \quad \text{if } \bar{\gamma}_k = 0 \quad (1.3)$$

$$dL = \frac{1+z}{H_0} dz \quad \text{if } \bar{\gamma}_k = 0 \quad (1.4)$$

with

$$h(z) = (1+z)^2 \bar{\gamma}_k + \bar{\gamma}_i \exp \left( \int_0^z \frac{1+w_i(z)}{1+z} dz \right)^{1/2} \quad (1.5)$$

where  $\bar{\gamma}_i = 8\bar{\gamma}_G \bar{\gamma}_i / (3H_0^2)$  represents the ratio of the density of constituent  $i$  to the critical density  $\bar{\gamma}_i$ , the curvature,  $\bar{\gamma}_k = \sinh$  for  $\bar{\gamma}_k < 0$  (closed universe) or  $\bar{\gamma}_k = \sinh$  for  $\bar{\gamma}_k > 0$  (open universe) or at the present epoch,  $\bar{\gamma}_k = 1$ ;  $S = \sinh$  for  $\bar{\gamma}_k < 0$  (closed universe) or at the present epoch,  $\bar{\gamma}_k = 1$ ; and  $H_0$  is, according to the notation, the Hubble constant at the present epoch.

In the case of a flat universe ( $\bar{\gamma}_k = 0$ ) comprising only matter and a cosmological constant of state equation  $w(z) = \bar{\gamma}_1$ , or  $\Lambda$ CDM model, this last expression is greatly simplified because

$$h(z) = (1+z)^3 \bar{\gamma}_m + \bar{\gamma}_\Lambda \quad (1.6)$$

The use of SNIa to constrain cosmological parameters therefore requires the simultaneous observation of fluxes and redshifts. It should be noted that the Hubble constant,  $H_0$ , is degenerate with the average luminosity of supernovae in the expression for the flux (Eq. 1.1), and is therefore not an observable constrained by the sole measurement of supernovae in the absence of an otherwise known zero point. Measurements made at the end of the last century are at the origin of the discovery of the accelerated expansion of the Universe (Riess et al., 1998; Perlmutter et al., 1999) and of the current concordance model. The combined data from supernovae, BAOs and WMAPs thus give  $\bar{\gamma}_\Lambda = 0.726 \pm 0.015$  and constrain to 95% CL the curvature  $0.0179 < \bar{\gamma}_k < 0.0081$  as well as the dark energy equation of state  $0.14 < 1+w < 0.12$  (Komatsu et al., 2009), which validates the plausibility of the  $\Lambda$ CDM model.

The observation of an accelerated expansion leads to several possible interpretations, and we will only mention a few of them. Einstein's equations relate the metric to the energy-momentum tensor by

$$G_{\mu\nu} + \bar{\gamma} g_{\mu\nu} = 8\bar{\gamma} T_{\mu\nu} \quad (1.7)$$

CHAPTER 1. TYPE 1A SUPERNOVAE: AN OBSERVABLE FOR COSMOLOGY

---

The accelerated expansion is the consequence of a non-zero cosmological constant, but limiting ourselves to this leads to new questions: first of all, the energy density implied by the cosmological constant is  $\dot{\gamma} = 10^{47} \text{ GeV}^4$  which is lower by many orders of magnitude than what is predicted by particle physics mechanisms, unless there are very precise compensation mechanisms: this is called fine tuning. While string theory offers some clues to obtain a low value of  $\dot{\gamma}$  via certain compactification scenarios, this approach is not yet conclusive. The anthropic principle is also invoked: in the context of an inflationary universe model that can predict an infinity of realizations with different  $\dot{\gamma}$  values, such as that of Linde, only universes where this value allowed the birth of Man can be, by definition, observed. This principle has the main disadvantage that it is hardly falsifiable, and we will leave the reader to judge its scientific relevance.

If the presence of a simple cosmological constant is not satisfactory, we can consider in Einstein's equations the term in  $\dot{\gamma}g_{\mu\nu}$  in the other member of the equation where it plays the role of an energy - hence the term dark energy. The modeling then comes down to determining the properties of one or more fields  $\dot{\gamma}$  whose dynamics would reproduce that of dark energy as observed. Among these models, those called quintessence models involve a scalar field equipped with a standard form of action

$$S = dx \int \frac{1}{2} \dot{\gamma} g_{\mu\nu} \dot{\gamma} \frac{d^4x}{2} - \frac{1}{2} \dot{\gamma} V(\dot{\gamma}) \quad (1.8)$$

and the challenge is to arrive at a coherent model that reproduces the phenomenon of dark energy by taking into account all observables, while opening up avenues on the nature of the  $\dot{\gamma}$  field inspired by particle physics models: supergravity models are prime candidates, as are those involving the axion, a pseudo-Goldstone boson that naturally explains the low value of  $\dot{\gamma}$ . These different models predict different forms for  $V(\dot{\gamma})$  and are therefore falsifiable.

Another interpretation is to consider the acceleration of the expansion as a modification of the laws of general relativity: it is then a matter of modifying the left-hand side of the Einstein equation by incorporating  $\dot{\gamma}$  into the dynamics. The so-called f(R) models are among the most studied (see e.g. [Sotiriou and Faraoni 2010](#) for a review), and proceed from the replacement of the Einstein-Hilbert action by

$$S = \frac{1}{2k_2} \int d^4x \sqrt{-\dot{\gamma}g} f(R) \quad (1.9)$$

With  $f(R) \approx R$  in the usual regime, but which deviates from it in the low acceleration regime.

Finally, the last approach consists not in accepting the presence of  $\dot{\gamma}$  as such or in seeking its causes in the form of dark energy or modifications of Einstein's equations, but in showing that the induced phenomenon can be explained by neglecting certain phenomena, in particular the effects of inhomogeneities - a review can be found in [Buchert \(2008\)](#). The main effect of inhomogeneities is to induce in an averaged description of Einstein's equations an apparent repulsive term of the same sign as a cosmological constant, called the backreaction term. Although the state of the work is not sufficient to determine its magnitude, this effect is nevertheless known to exist.

These various interpretations all offer an observable phenomenological consequence in terms of the effective equation of state,  $w(z)$ . If current accuracies are sufficient to constrain  $w(z = 0)$ , the improvement of measurements and the reduction of uncertainties, both statistical and

---

## 1.2. THE SUPERNOVA OBJECT

systematics, is necessary to discriminate between the various models and provide a measure of the variation as a function of  $z$ . Current work on supernovae is part of this perspective.

## 1.2 The Supernova Object

Type Ia supernovae are spectrally defined by the absence of hydrogen and helium lines, and by the presence of a prominent Si II  $\lambda 6355$  line. They are also characterized by their nebular spectrum, which still contains broad lines, while that of type Ic supernovae has well-defined emission lines. While they are well distinguished spectrally, the mechanism of their explosion is still widely debated, and the related questions can be summarized as follows. First, several hypotheses are possible regarding the progenitor: two classes of models are in fact invoked, the so-called simply degenerate (SD) models, in which only a single white dwarf is involved, or the doubly degenerate models, which result from the coalescence of two compact cores. Then, the development of the explosion itself gives rise to numerous hypotheses, first on the ignition site, then on the nature of the propagation: deflagration or detonation, possibly followed by a second detonation. Finally, the synthesis of the spectra starts from the composition of the ejecta and deduces the temporal spectral evolution. But even if it only involves well-known physical processes of light transport, it requires large computational times, and does not allow easy resolution of the inverse problem: given an observed spectral series of supernova, what is the composition and velocity structure of the ejecta? We will therefore briefly review these factors of uncertainty on our understanding of the object, in order to underline the importance and the difficulties linked to a necessarily empirical modeling of the flux received from the object.

### 1.2.1 Progenitor

The progenitor question, while generating abundant literature, benefits from very few review articles, and even then they are old or partial ([Branch et al., 1995](#); [Kotak, 2008](#)). The mechanism behind the explosion of SNIa was initially proposed by [Hoyle and Fowler \(1960\)](#), who determined that type I supernovae (the Ia/Ib/c distinction dates from 1990) were due to the thermonuclear explosion of white dwarfs. [Whelan and Iben \(1973\)](#) proposed the single degenerate or SD mechanism, by which this explosion was due to a C+O white dwarf in a binary system accreting matter from a companion until it approached sufficiently close to the Chandrasekhar mass of  $1.4 M_{\odot}$ . The nature of this companion could be either a star on the main sequence or a red giant. Shortly after, [Iben and Tutukov \(1984\)](#) and [Webbink \(1984\)](#) introduced the double degenerate or DD mechanism, by which the explosion results from the coalescence of two degenerate cores. Although nothing is currently decided between these two mechanisms, it is established that one of the objects must be a degenerate C+O core: indeed, the ignition of a He-type white dwarf will occur when it reaches  $0.7 M_{\odot}$  and will certainly produce  $^{56}\text{Ni}$ , but not all the intermediate elements observed in supernova spectra, which therefore excludes this progenitor as a natural pathway for the production of SNIa. As for O+Ne+Mg cores approaching the Chandrasekhar mass, they are expected to implode into neutron stars rather than produce SNIa. In any case, the presence of a C+O white dwarf implies a star with a mass between 3 and  $8 M_{\odot}$ ,

---

<sup>2</sup>See references cited by [Branch et al. \(1995\)](#)

## CHAPTER 1. TYPE 1A SUPERNOVAE: AN OBSERVABLE FOR COSMOLOGY

---

as for its companion in the case of a simply degenerate model, it must be at a less evolved stage of its stellar sequence, and may therefore be less massive.

In order to distinguish the two classes of scenarios, several observations can be invoked. First, the existence of several subclasses of supernovae opens the question of the coexistence of several mechanisms. Indeed, based on spectral characteristics [Branch et al. \(2006\)](#) defined several subclasses: normals, whose representative type is 1994D, subluminous or type 1999bg, supernovae with narrow Si ii  $\lambda\lambda$ 6355 lines, also known as overluminous of type 1991T (of which SN2002cx could be a distinct subtype, [Li et al., 2003](#)), and finally a class defined by broad Si ii  $\lambda\lambda$ 6355 lines also linked to a strong velocity gradient of this line over time ([Benetti et al., 2005](#)). Finally, let us mention the so-called super-Chandrasekhar supernovae, such as 2003fg or 2007if, whose luminosity can only be explained by a mass of 56Ni greater than the Chandrasekhar mass. The questions that arise when faced with such a typology are the existence of a continuum of physical conditions allowing passage from one to the other, or of different conditions, which could support the existence of several mechanisms.

The bolometric luminosity of the supernova is related to the mass of synthesized 56Ni to the first order ([Arnett, 1982](#)). It can be measured by observing light curves ([Stritzinger et al., 2006](#)). The observed dispersion is large, from 0.2 to 1.0  $M_\odot$  ([Howell et al., 2009](#)), but compatible with an explosion at the Chandrasekhar mass, and therefore with an SD-type scenario. However, subluminous supernovae of type 1991bg have a reconstructed mass less than 0.1  $M_\odot$ , and one may wonder if they obey the same explosion mechanism, or if they would be the trace of sub-Chandrasekhar explosions. Finally, SN2007if is the most luminous object ever observed, and SNfactory data have allowed the reconstruction of  $M_{56\text{Ni}} = 1.6 M_\odot$  ([Scalzo et al., 2010](#)). This object can only be explained in a DD framework, however, its spectral characteristics are well identified and different from so-called normal supernovae. If the DD model were dominant, one would expect a very wide range of binary systems that could lead to an explosion, and one should have a continuum of produced masses. These observations would rather favor the SD model as the main pathway for the production of SNIa, with in addition a sub-dominant DD pathway and perhaps some sub-Chandrasekhar explosions.

The study of the circumstellar medium allows us to search for the presence of ejecta from the white dwarf companion in the SD case. In particular, one would expect to find the presence of hydrogen or helium in the early spectra of the objects, and such an observation was made on SN2005gj by the SNfactory collaboration ([Aldering et al., 2006](#)). However, only two such objects could be observed, and they exhibit particular spectral characteristics: these objects are not necessarily representative of the dominant production channel. Furthermore, one would expect an observable hydrogen signal in the nebular phase, which has not been observed. [Patat et al. \(2007\)](#) detected absorption by Na i D lines attributed to material expanding at a speed of 100 km/s around a supernova, SN2006X, which indicates an SD-type mechanism, provided that the object is representative of ordinary supernovae. Soft X-ray emission related to material absorbed by the companion is another signature of circumstellar material. Recently, an estimate of this flux by [Gilfanov and Bogd'an \(2010\)](#) in early-type galaxies showed that it was too low compared to what was expected in an SD scenario, triggering a controversy: the results reinterpreted by [Hachisu et al. \(2010\)](#) show that the phase during which the object is an X-ray emitter is shorter than expected, making the observations finally compatible with the SD scenario.

As for direct searches for the white dwarf's companion, they are delicate before the explosion because the objects in question are of low magnitude. In the case of the SD model,

## 1.2. THE SUPERNOVA OBJECT

---

The evolution of the object during its mass accretion passes through a stage where the accreted hydrogen ignites in repetitive flashes. The recurring nova system RS Ophiuchi which exhibits flashes every 22 years has been identified as a progenitor of SNIa [Walder et al. \(2008\)](#). However, due to the regular decrease of the companion orbit due to mass transfer, it is not yet possible to say whether the SNIa from this system will be of type SD or DD. The search for white dwarf binary systems that coalesce in a sufficiently short time to give rise to SNIa also allows the study of the DD channel, and a catalog has been established by [Napiwotzki et al. \(2004\)](#). However, the great diversity of initial conditions gives rise to only one candidate as a progenitor for an SNIa out of the 120 studied. Archive images from the Hubble Space Telescope have been used to search for traces of bright stars at the site of supernova explosions, but have so far only allowed the placing of loose limits of the order of 4 to 9 Myr on the mass of the companion ([Maoz and Mannucci, 2008](#)). Finally, in the SD case, it is possible to search for the remnant of the companion after the explosion, which blew away part of the envelope, creating a hole in the ejecta structure ([Marietta et al., 2000](#)) and could be a source of variability in the received flux. Finally, [Ruiz-Lapuente et al. \(2004\)](#) claimed to have found such a candidate in the remnant of Tycho Brahe's supernova, located at a distance of 2 to 5 kpc, but this result is controversial [Ihara et al. \(2007\)](#). As we can see, the direct search for progenitors is not conclusive.

The different models must also be compatible with the SNIa explosion rate as a function of the age of the progenitor, or DTD for delayed time distribution, which is observable through a reconstruction of the history of star formation. Whether the rates measured by distant surveys (see e.g. [Brandt et al., 2010](#)) or those inferred from galaxy clusters ([Maoz et al., 2010](#)), observations have been consistent for several years with a mechanism involving two populations, even if there is a continuum between the two: one that would explode quickly after star formation, with half of the events, called fast, included in the first 420 Myr to 1 Gyr, and a second component, called delayed, which can produce explosions up to a Hubble time. The association of these components with different progenitor natures is still delicate: we certainly observe that so-called fast supernovae are more luminous on average, and on the other hand are favored by SD type mechanisms, whereas DD type mechanisms are more compatible with delayed supernovae. However, the observed number of supernovae, whether one invokes one or the other mechanism or a mixture of the two, is insufficient to reproduce the iron enrichment of the universe, and on the other hand there is no clear link between the explosion mechanism and observed luminosity: nothing says that the difference in luminosity between fast and delayed does not come from composition effects of the progenitor, such as its metallicity.

While it is difficult to draw definitive conclusions about the nature of the progenitor, the SD scenario has long been preferred, even though not all of its predictions are observed, and it likely coexists with other explosion mechanisms. However, recent research shows a renewed interest in the DD scenario, which satisfies many observational constraints, even though simulations of the explosion in this mode still struggle to reproduce the observed spectra. The main drawback of this scenario is its inability to predict the spectra observed after the explosion. However, the general nature of the scenario is not the only one influencing the variations in received luminosity: the nature of the environment plays a role, and one of the burning questions currently concerns the differences related to the nature of the host galaxies, in the absence of being able to directly test the nature of the progenitor. Thus, if supernovae are intrinsically more luminous in active star-forming galaxies, it would seem that the current standardization procedures that we will describe later are not sufficient to fully interpret the observed differences ([Sullivan et al., 2010; Lampeitl et al., 2010](#)).

CHAPTER 1. TYPE 1A SUPERNOVAE: AN OBSERVABLE FOR COSMOLOGY

---

### 1.2.2 Explosion

While there are several scenarios for the progenitors of SNIa, the principles governing the physics of the explosion past the initial instant are fairly well understood, even if the fine modeling of the turbulent propagation of the thermonuclear flame front over orders of magnitude from millimeters to thousands of kilometers is beyond the reach of computers and it is necessary to make approximations. A clear review of the state of the art in this field can be found in [Ropke et al. \(2011\)](#), of which we will only recall the broad outlines.

Under the SD scenario, as the Chandrasekhar mass is approached, the central density becomes sufficient to allow carbon fusion. This is not initially explosive, as heat is transported convectively and turbulently, until the temperature increase is sufficient to cause hot spots and initiate a flame front. The distribution of these hot spots is still largely unconstrained, however, and this is an important assumption in the modeling.

Once the explosion has initiated, the only robust scenario involves a deflagration whose front must be turbulent ([Nomoto et al., 1984](#)) : in fact the density is almost constant throughout the white dwarf, and a detonation would only produce elements of the iron group, to the detriment of the intermediate elements (Si, Ca, Mg, S) which are observed in the spectra. A laminar deflagration, on the other hand, would be affected by too rapid an expansion of the envelope, and would extinguish quickly. However, the turbulent deflagration model produces only 0.3 M $\odot$  of 56Ni, which is insufficient to account for normal SNIa - but could be a mechanism to explain some particular SNIa, such as SN2002cx. To produce sufficient 56Ni, one must assume the transition from flame propagation to detonation, a scenario proposed by [Khokhlov \(1991\)](#). The spectra and light curves obtained under this scenario are consistent with observations ([Kasen et al., 2009](#)).

However, another mechanism, long little studied, allows us to reproduce the observed spectra: that of the double detonation of a white dwarf below the mass of Chandrasekhar. The principle is as follows: the outer layer of the white dwarf, consisting of helium from the accretion of matter from a companion, ends up detonating in certain accumulation regimes . This detonation generates a shock wave capable of initiating a secondary detonation of the C+O nucleus, as well as a preheated object at the time this second detonation occurs, which allows the synthesis of intermediate elements. Assuming that the helium layer is sufficiently thin, it is possible to achieve satisfactory agreement with the spectra of observed supernovae ([Sim et al., 2010](#)).

Finally, simulations involving DD progenitors only produce SNIa if the mass of the two degenerate cores is similar, and the explosion produces only a subluminous event, of the 1991bg type. From a simulation perspective, this channel is not dominant. However, the study of white dwarf coalescences shows that in the case of an asymmetric binary, the lighter core breaks up, giving rise to a ring of matter gradually accreted by the companion, which opens a way to rehabilitate this model as the main formation channel.

What will interest the cosmologist in this discussion on the explosion mechanism are the sources of variations from one object to another. The most studied model from this point of view is delayed detonation. The luminosity of the object is driven to the first order by the mass of 56Ni produced. A variation in the ignition conditions—linked to the turbulent structure during the nuclear combustion of carbon—may help explain it, but this only pushes the questioning upstream to a poorly controlled stage of the process. Another expected effect is that of the variation in the metallicity of the progenitor ([Timmes et al., 2003; Howell](#)

---

## 1.2. THE SUPERNOVA OBJECT

**et al., 2009).** Indeed, the initial presence of CNO in the white dwarf progenitor produces  $^{22}\text{Ne}$  when it leaves the main sequence to burn its helium. This neutron-rich nucleus will disrupt explosive nucleosynthesis by producing stable  $^{58}\text{Ni}$  and  $^{54}\text{Fe}$ . A more metallic environment will therefore produce a less luminous supernova, which has been highlighted via environmental effects, even if their amplitude induces a lower variation in luminosity than what is observed. Finally, it should be noted that in the framework of a double detonation model, as well as in the framework of the coalescence of two binaries, the initial mass of the white dwarf is not constrained, which provides a natural mechanism to explain a variation in the mass of  $^{56}\text{Ni}$  produced.

In addition to the more or less significant production of  $^{56}\text{Ni}$ , other phenomena can induce spectral variations of objects. The presence of a turbulent front can indeed induce a more or less significant mixing of the synthesized material, but as shown by [Woosley et al. \(2007\)](#), it is necessary to introduce a correlation between the degree of mixing and the mass of  $^{56}\text{Ni}$  produced to find the experimental curves linking the maximum luminosity and the shape of the light curve. Finally, since there is a source of asymmetry in explosions, whether it is the helium ignition point in the double detonation model ([Kromer et al., 2010](#)), or an explosion shifted from the center due to convection induced by carbon combustion in the delayed detonation model ([Maeda et al., 2010](#)), or a plane of symmetry in the DD case, the direction of the observer relative to the explosion system can explain part of the observed spectral variations.

### 1.2.3 Standardization

The current state of theoretical modeling of supernova explosions therefore does not allow the spectral energy distribution to be predicted with sufficient precision to directly determine a distance from the observed flux and the spectral characteristics of the object. An empirical standardization procedure will be required. Despite all the sources of variability cited, the luminosity of supernovae can be remarkably well described by a two-parameter model: color and shape of the light curve. About ten different models have been used in the past, but they generally use the same principles, although with notable differences. We will focus on MLCS2K2 ([Jha et al., 2007](#)) and SALT2 ([Guy et al., 2007](#)), which are among the most widely used, and this will highlight the differences between the various approaches, with SALT2 being, in our opinion, the most conceptually advanced.

The first decision to make when building a model is to take into account the absolute flux of the object. MLCS2K2 is thus a distance estimator, in the sense that it directly links the properties of the light curves to an absolute magnitude: at the end of the fitting of a supernova to the model, the magnitude provided is directly comparable to the distance modulus. In contrast, in SALT2, only the parameters of the light curve are adjusted: the phase at maximum, the observed brightness,  $m_B$  which is a shape parameter accounting for the brighter-slower relationship and  $c$  which describes the color of the object. The correction to be made to the adjusted brightness in order to minimize the residuals in the Hubble diagram is only defined in a second step, by

$$\mu_B = m_B - B - M + \gamma x_1 + \gamma c \quad (1.10)$$

where  $M$  is the absolute magnitude, and  $\gamma$  and  $c$  are adjusted parameters. This formulation is very close to that of MLCS2k2, except for a few details. The latter is in fact written at most

## CHAPTER 1. TYPE 1A SUPERNOVAE: AN OBSERVABLE FOR COSMOLOGY

of brightness

$$bX mX = MX + \mu_0 + Px\ddot{y} + Qx\ddot{y}^2 + ax + \frac{0}{RV} \quad (1.11)$$

where  $MX$  is the absolute magnitude in X-band,  $\mu_0$  the distance modulus,  $\ddot{y}$  the light curve shape parameter, which can be related to  $x_1$  by a polynomial expansion, and  $A_0$  the absorption in V-band, which defines the object's color via a law of the type [Cardelli et al. \(1989\)](#). The functional appearance is similar, apart from a quadratic term in  $\ddot{y}$ : the spectral formation is indeed non-linear, and it is not surprising that the modeling must take this into account. For example, at most the Si ii  $\ddot{y}6355$  line is known to saturate and vary non-linearly with Si ii  $\ddot{y}5972$ , (see for example [Branch et al. \(2009\)](#)). However, [Conley et al. \(2008\)](#) have shown that the effect of this quadratic term is ultimately small. Several differences remain, however, important: first, MLCS2K2 assumes that the color of the supernova is solely due to extinction by dust from the host galaxy: this amounts to fixing the

$bX$  parameter  $RV$  as well as the functional form  $ax + \frac{0}{RV}$  SALT2 uses a color law free, and attributes the color effect to a mixture of intrinsic supernova and extrinsic effects such as extinction. It turns out that the choice of  $RV$  is therefore decisive for standardization, and after several studies ([Hicken et al., 2009b](#)), it appeared that the best value is  $RV = 1.7$ , close to the value implied by the  $\ddot{y}$  of the SALT2 fit, but far from the galactic average of  $RV = 3.1$ . The reason for this difference will be discussed in the last chapter of this work, and the apparent inconsistency between the two values has caused much ink to flow: the difference amounted to saying that the properties of the dusts were different depending on the probe used to measure them, unless it could be explained by the intrinsic properties of the SNIa.

The other major difference in terms of model implementation is that MLCS2K2 only considers broadband light curves, whereas SALT2 relies on a modeling of the spectral energy distribution:

$$S(\ddot{y}, \ddot{y}) = x_0 S_0(\ddot{y}, \ddot{y}) [1 + x_1 S_1(\ddot{y}, \ddot{y})] \exp[\ddot{y}c CL(\ddot{y})] \quad (1.12)$$

where  $S$  is the spectral energy distribution depending on the wavelength  $\ddot{y}$  and the phase  $\ddot{y}$ ,  $S_i$  spectral patterns,  $(x_i, c)$  parameters fitted to the light curves and  $CL(\ddot{y})$  a phase-independent color law. Training the MLCS2K2 model must therefore use numerous filter corrections related to the red shift to bring them back into the bands in the resting frame, or K corrections. For this, they use an external spectral model, which does not take into account the stretch corrections, whereas SALT2 directly integrates the number of photons received into the bandwidth of the observational filter, i.e. without making any K corrections strictly speaking.

The choice to make a distance estimator also implies differences concerning the training batch: in the case of MLCS2K2, it is indeed necessary to have a reliable distance estimator for it, and therefore to restrict oneself in redshift in order to be polluted neither by particular velocities nor by cosmological effects — unless the entire training is readjusted once the cosmological parameters have been determined. Finally, the last conceptual problem of MLCS2K2 comes from the consideration of absorption in the formalism: the zero point of the latter is indeed not known, and defining an ensemble without extinction, for example by selecting only supernovae in elliptical galaxies, on the one hand considerably reduces the statistics available for training, and on the other hand does not guarantee the absence of dust, for example linked to circumstellar material. The model

---

## 1.2. THE SUPERNOVA OBJECT

**MLCS2k2** then takes into account a prior on the intrinsic color dispersion of supernovae to define its zero, which is a source of systematic bias.

However, even if the SALT2 model is conceptually better defined, a number of questions remain: indeed, the cosmological adjustment shows that the standardization of objects is not perfect, and that it is necessary to take into account an intrinsic dispersion in luminosity from one object to another of the order of 0.09 magnitudes ([Guy et al., 2010](#)). Moreover, the interpretation of the adjusted value of  $\bar{y} = 3.1$  in terms of extinction leads to  $RV = 2.1$ , a value significantly lower than the average observed in the Milky Way or the Magellanic Clouds. Is this due to exotic properties of dust depending on the environment, which would lead to evolutionary effects that would have to be taken into account, or is it linked to absorption in the immediate vicinity of the SNIA, as proposed by [Goobar \(2008\)](#), or to an intrinsic color component of the object that would have the effect of distorting the interpretation in terms of dust, or finally to poor consideration of intrinsic dispersions ([Chotard et al., 2011](#)) ?

The answer to these questions requires improving the empirical modeling of supernovae , possibly supported by clues from their theoretical understanding, even if the latter is insufficient to provide a numerical model. In particular, the questions to be clarified are the following: How many intrinsic parameters are we able to discern? Should quadratic or even higher-order correction terms be taken into account?

Is the color related to an extinction, and if so, is the law of the latter compatible or not with the galactic value? To answer these questions, a reference batch in the Hubble flow (i.e. not affected by particular velocities) is necessary to allow a reconstruction of the spectral energy distribution by means of a minimal interpolation.

This is one of the goals of the Nearby Supernova Factory experiment.

## Contributions

Although the cosmological considerations contained in this chapter have not given rise to any research work per se, their knowledge is necessary for anyone wishing to do cosmology , and has served as a basis for the presentations I made at the LPC prospective days (2007 and 2010) in order to promote an activity on the LSST. Furthermore, they have served as a basis for numerous public conferences: Newton, from gravitation to the apple, Head in the stars, The Origin of the elements or What is our Universe made of, as well as several radio broadcasts and other actions aimed at the general public (science festival, science bar, CRAL festival, etc.). Finally, the very good TIPE internship of Satya Gontcho that I supervised had as its subject the extraction of cosmological parameters from data from the first year of SNLS.

As for the considerations on supernova physics, in addition to supporting the analysis described in Chapter 4, they have given rise to publications from the SNfactory collaboration of which I am a signatory. In [Aldering et al. \(2006\)](#), we reported our observations of an SNIA exhibiting a thin hydrogen line, SN2005gj, which demonstrates the presence of circumstellar material linked to the progenitor, for which an initial mass greater than  $4M_{\odot}$  can be hypothesized. In [Thomas et al. \(2007\)](#), we show the presence of unburned carbon at low speeds in SN2006D, an observation consistent with pure deflagration scenarios, unlike delayed detonations for which the presence of unburned carbon should only appear at very high speeds. Finally, we have published two papers concerning the supernova super-Chandrasekhar 2007if, [Scalzo et al. \(2010\)](#) and [Childress et al. \(2011\)](#).

Other articles relate more to cosmology itself: the relevance of SNfactory is described in [Kerschhaggl et al. \(2011\)](#), while [Bailey et al. \(2009\)](#) develops

## CHAPTER 1. TYPE 1A SUPERNOVAE: AN OBSERVABLE FOR COSMOLOGY

---

a new method of standardization. Finally, the content of [Chotard et al. \(2011\)](#) will be the subject of chapter 4 .

# Chapter 2

# Nearby Supernova Factory

## Summary

The observation of supernovae comes up against a pitfall: the object is transient, and it is necessary to detect it and take the necessary measures during the limited time when it is observable, of the order of fifteen days before the maximum brightness to a few months afterwards. The nebular phase of the object, observable on Earth about a year after the initial explosion, is not bright enough to be usable in cosmology, which therefore focuses on the period preceding the maximum and the thirty to fifty days which follow, during which the Bolometric luminosity is driven by the period of  $^{56}\text{Co}$ , about 77 days. The first measures consisted of "Cowboy" campaigns, where the aim was to obtain time from telescope in advance for a few nights, including spectroscopy facilities, and to make a quick online discount hoping for good fishing. However, the arrival of the surveys large field such as the SNLS (Astier et al., 2006; Guy et al., 2010 and refs. included) or SDSS (Frieman et al., 2008; Kessler et al., 2009) has significantly changed the situation, by allowing regular photometric monitoring of the same fraction of the sky, essential for reducing systematic uncertainties. However, these cosmological redshift surveys suffer of a limiting signal-to-noise ratio for spectral studies and the results have long incorporated a heterogeneous batch of nearby supernovae: it is only recently that we have from an extended batch of 185 supernovae obtained by the CfA survey (Hicken et al., 2009a).

---

## CHAPTER 2. NEARBY SUPERNOVA FACTORY

---

The Nearby Supernova Factory (SNfactory, [Aldering et al., 2002](#)) collaboration was established in 2001, at a time when there were only 17 nearby supernovae ( $z < 0.15$ ) contributing to the Hubble diagram. It focused on acquiring spectrophotometric time series of about 300 nearby SNIa but within the Hubble flow ( $0.03 < z < 0.08$ ), the area that can best contribute to increasing the lever arm for determining cosmological parameters, as confirmed by [Linder \(2006\)](#). Obtaining not photometric measurement points but absolutely calibrated spectrophotometric time series in flux gave rise to a batch of data without direct competitor. This required the development of a dedicated instrument, an integral field spectrograph for spectrophotometry, SNIFS , and the instrument was permanently mounted on the UH 2.2m telescope in Hawaii in April 2004. The main data collection of the experiment took place from 2005 to 2008, with reference acquisitions in 2009 and 2010 once supernovae had become undetectable.

Since 2011, a new series of data acquisitions has been underway, with a slightly different scientific objective, and a new supernova source, the PTF project ([Law et al., 2009](#)). In parallel, a scientific follow-up to the experiment would consist of acquiring a sample of spectrophotometric time series at higher redshifts, in order to directly study the evolution effects. The FIREBALL project, to whose proposal we contributed but which was not selected, constituted a first step towards reaching  $z = 0.5$ . However, the observation time cost of obtaining high signal-to-noise spectra in the early universe makes a time request difficult to obtain until the scientific case has been fully established by analyzing the SNfactory data. It is indeed crucial to determine whether a subset of correctly measured phases can capture most of the object's variability, or whether photometric methods such as those that will be implemented by LSST can suffice to obtain them.

### 2.1 Scientific objective

With a spectrotemporal series of 300 nearby SNIa, the scientific objectives of SNfactory are as follows:

- The first objective was to reduce statistical uncertainties related to the small number of nearby objects available: in fact, nearby supernovae constrain the LH2 nuisance parameter present in the expression of the received flux. This implies taking supernovae in the Hubble flow, i.e.  $z > 0.03$  in order to minimize the uncertainty related to the particular velocities of the host galaxies. On the other hand, obtaining a sufficient signal-to-noise ratio requires restricting ourselves to luminous objects, hence an initial limit for object selection at  $z = 0.08$ . A batch of 300 supernovae, with a flux calibration of a few percent, is indeed sufficient to reach the point from which the improvement of the cosmological figure of merit<sup>1</sup> begins to stagnate when including 2000 supernovae between  $0.3 < z < 0.9$  as planned for the SNAP space project. The arrival of important photometric batches of supernovae since 2009 (CfA, SDSS) has however put into perspective the impact of the SNfactory batch on the Hubble diagram, and the SNF-II project now focuses on the joint use of SNfactory data with photometric measurements available for the same objects, which was not the case for phase I of the experiment, in which only a few SNfactory supernovae can be compared with photometry data from other sources;

---

<sup>1</sup>defined by the Dark Energy Task Force as the inverse of the area of the uncertainty contour on the first two parameters of the dark energy equation of state.

## 2.2. SEARCH FOR SUPERNOVAE

---

– The resulting data set is, however, essential for training empirical models: the presence of directly calibrated data in the form of energy spectral density with phase tracking on the evolution of the object greatly simplifies the modeling of this density. Even in the absence of model improvement, the SNfactory set is intended to serve as a reference; – The presence of reference spectra also allows measurements to be made that are free from K corrections. Indeed, on our data it is possible to directly integrate synthetic filters redshifted by an arbitrary amount, and thus to construct Hubble diagrams in comparable filter systems, where the filter system of the photometric surveys is fixed once and for all. This method, in its initial stages, cannot be extended to photometric surveys, but it potentially allows us to provide reference spectra as close as possible to those of distant objects for the calculation of these K corrections in the absence of any underlying modeling; – Spectral series also allow for the improvement of supernova modeling: in fact, an SNfactory spectrum potentially contains 2000 measurement points, whereas photometry typically only obtains 5. The search for correlations between spectral structures and the luminosity of the object opens up avenues for improving modeling. [Nugent et al. \(1995\)](#) paved the way by showing a possible correlation between Si and Ca line ratios with the absolute magnitude of the objects. Since then, many spectral indicators have been studied, but apart from the equivalent depth of the Si II  $\lambda$ 4131 line ([Arsenijevic et al., 2008](#)) or the correlations of the Si II  $\lambda$ 6355 velocity with the colors of objects [Wang et al. \(2009\)](#), the link between indicators and standardization is still a fallow subject. The studies carried out on this subject will be the subject of the last part of this work as well as of Nicolas [Chotard's thesis \(2011\)](#). The presence of correlation between the spectral properties and the luminosity of objects will therefore make it possible on the one hand to potentially improve the modeling of the spectral energy distribution, by clarifying the mystery of the color law, or by providing other intrinsic variabilities than the stretch or its variants ([Chotard et al., 2011](#)); – Spectral indicators—or any other metrics developed on spectra—will also provide leverage for studying evolutionary effects: indeed, the parameter space sampled at low redshift is likely to be different from that sampled in a younger universe, or to depend on the nature of the host galaxy, as discussed in the previous chapter. Even if secondary variability of objects plays only a small role compared to the decrease in residuals in the Hubble diagram, their monitoring will be a strong indication of the uncertainty in extrapolation made between low and high redshifts; – Finally, obtaining calibrated time series of spectroscopy will allow us to study a new way of comparing nearby and distant supernovae: a study is underway within the collaboration to determine whether it is possible to match supernovae that differ only by extinction. If this is the case, it would then become possible to establish a Hubble diagram of identical pairs, which would therefore not suffer from biases related to standardization procedures. This method is, however, only in the exploratory stage ([Fakhouri et al., 2011](#)).

## 2.2 Search for supernovae

A spectroscopic monitoring project requires a standalone supernova detection program. This requires scanning a sufficient volume of the universe. As part of the

## CHAPTER 2. NEARBY SUPERNOVA FACTORY

---

For nearby SNIa, two methods exist: the first consists of optimizing search efficiency by targeting only known galaxy clusters. This is the strategy on which the otherwise heterogeneous batch of supernovae near CfA is based (Hicken et al., 2009a). The disadvantage of this technique is a selection bias depending on the supernova environment; however, it is the only one that currently allows a sufficient discovery rate at very low redshift. SNfactory, on the other hand, uses a so-called untargeted, or blind search, methodology intended to reproduce the methodology of high- $z$  searches. This involves scanning several hundred square degrees (noted) across the sky per night, and after data reduction, searching for SNIa candidates. The data were provided by the QUEST-II camera on the Palomar 1.2m, with a sensitive area of 9.6 and equipped with 4 filters (Baltay et al., 2007). The search for supernovae is grafted onto the NEAT asteroid search program, which explains why the search is carried out in the R band, with a limiting magnitude of 21, which is not limiting in relation to the spectroscopic monitoring capabilities, for which the limiting magnitude in V is 19.5, which corresponds to the maximum luminosity of a supernova at  $z = 0.13$ , i.e. beyond the target limit of  $z < 0.08$ .

One of the difficulties of the research, conducted by our American colleagues in conjunction with other programs, is that the sky areas of interest for supernovae do not coincide with those of the main program: in particular, the search for asteroids is concentrated on the plane of the ecliptic, where the search for supernovae would tend to avoid it. Finally, to ensure a sufficient filling rate of the spectroscopic observation tail, it is necessary to be able to ideally follow around ten objects, while typing two or three per night. This implies both a sufficient flow of candidates to observe, which is provided by the 450 observed on average per night, but also sufficient purity of the candidates. Unlike rolling search surveys, which revisit the same fields regularly and can perform a posteriori sorting, the alert must be made as close as possible to the first detection. A boosted decision tree method has been developed to provide sufficient purity of candidates (Bailey et al., 2007), and therefore a sufficiently reduced list of objects submitted for manual verification before being sent to spectroscopy for confirmation. However, it is regrettable that the bias resulting from this procedure has not been extensively evaluated, particularly with regard to the distance to the galactic center, which will limit certain studies covering our entire sample.

In total, the supernova search yielded more than 7000 detections, of which 1031 supernovae were identified, over a total area covered of about  $2\text{y sr}$  (see Table 2.1 and Figure 2.1). Since the supernova search was not immediately operational with the expected rate, we used public supernova sources. This was also the

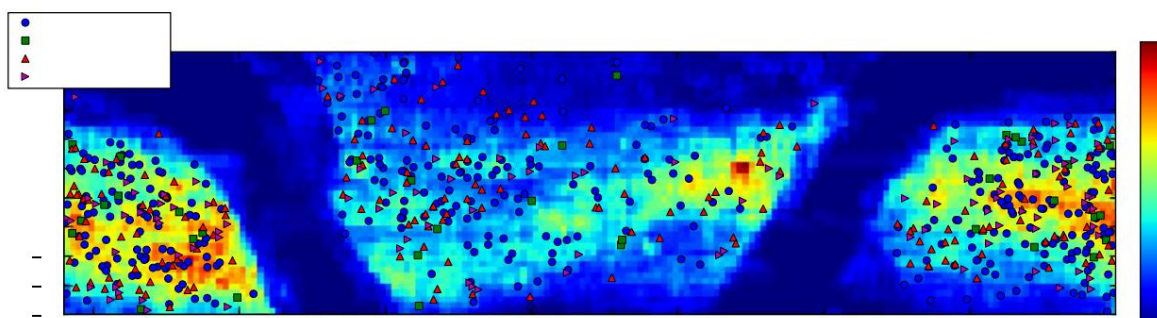


Fig. 2.1: Portion of the sky observed by the QUEST-NEAT program, with the indication of confirmed supernova detections as well as spectra of candidates.

---

## 2.2. SEARCH FOR SUPERNOVAE

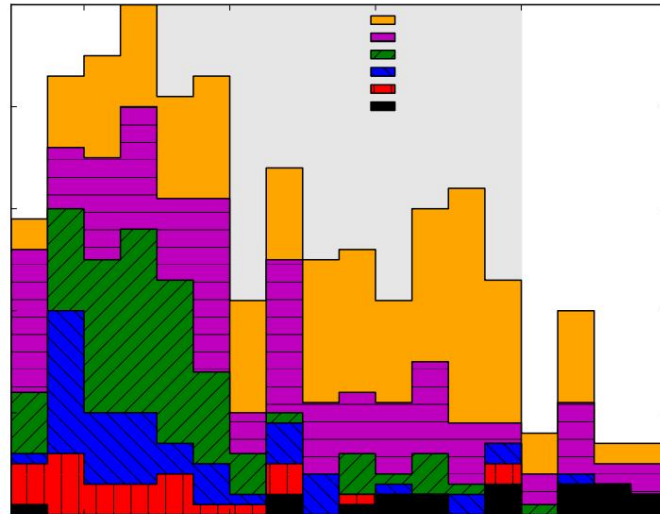
---

**Tab. 2.1: Sample of supernovae from the program.** The " QUEST " line indicates the whole detections submitted for decision, the line " + spectrum " indicates the number of SNfactory objects for which a spectrum was acquired, the " Other " line the number of objects speculated outside the source SNfactory. Finally, the " Total followed " line indicates the number of SNIa with at least 6 spectra along the light curve. The " Detection " column indicates the total number of detections made, and the following indicates their origin: ONI is the abbreviation for Unidentified Object (flying or not), " Error " indicates a subtraction artifact, " Variable " a variable star and we distinguish SN candidates of confirmed SNs, some of which were confirmed by measures other than our spectroscopy. The table below gives details by type of supernova.

Source	ONI	Detections	AGN	Error	Asteroid	Variable	Candidate	SN	SN		
QUEST	7017	888	489	261	2453	1031	1136			759	
+ spectrum	859	42	5	27	4		74			41	660
Others	-	-	-	-	-		-			12	90
<b>Total followed</b>	<b>199</b>						<b>194</b>	<b>2</b>			<b>3</b>

Source	Total	SN	Untyped	Ia	Ib/c	SNII/IIn		
QUEST	1031		407	396	37		191	
+spectrum	660		67	380	36		177	
Others	90		3	64	6		17	
<b>Total followed</b>	<b>199</b>		-	<b>194</b>	<b>2</b>			<b>3</b>



**Fig. 2.2: Number of supernovae available in the range  $0.01 < z < 0.1$ , depending on the sources.** The SNfactory target area is shown in gray, i.e.  $0.03 < z < 0.08$

---

**CHAPTER 2. NEARBY SUPERNOVA FACTORY**


---

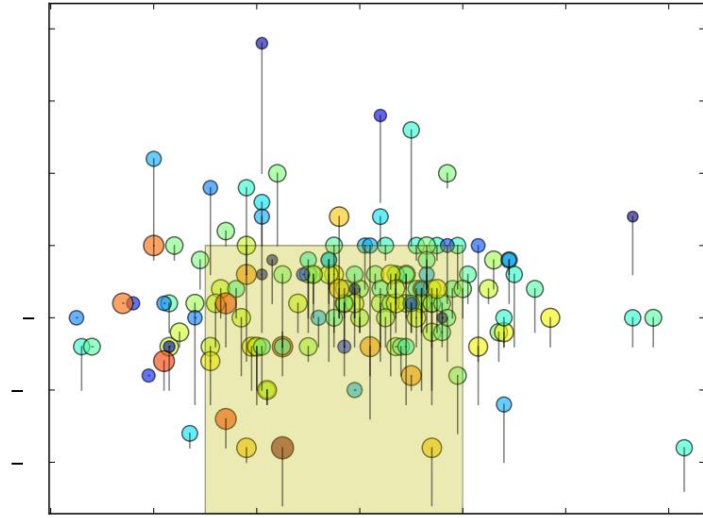


**Fig. 2.3: Distribution of tracked SNIa as a function of redshift and phase of the first spectrum. The area of the circles is proportional to the number of acquired spectra, highlighted by a color code, the vertical lines represent the latency delay between detection by QUEST, given by the lower end of the line, and the first SNfactory spectrum. The rectangle represents the target fiducial area of the project.**

case when a public supernova was of sufficient interest to trigger a follow-up. In total, 190 supernovae are available for cosmological analysis, with more than 6 spectra taken along their light curve for a total of 3017 spectra, or an average of 15.5 spectra per object. Figure 2.2 shows the redshift of supernovae in the SNfactory sample, limited to the useful redshift domain. In the Hubble stream, from  $z > 0.04$  the accumulated data fill an existing gap, and can therefore play an important role in calibrating objects in the Hubble stream, and serve as an anchor point for the Hubble stream diagram. Figure 2.3 shows the phase distribution of supernovae, the phase here being that determined at discovery. The median phase of the first spectrum is -4 days before the maximum, and 90% of the monitored supernovae have a first spectrum before their maximum brightness. The average time between the acquisition of the first spectrum and discovery is 2.7 days.

### 2.3 Spectrophotometry: the SNIFS instrument

Transient object spectrophotometry is an innovative technique that requires the construction of a dedicated integral field spectrograph, SNIFS (Lantz et al., 2004), whose optical scheme is described in Figure 2.4. The incident beam of the telescope is distributed between 3 optical channels: on the one hand, an imaging and guiding assembly composed of two attached CCDs constitutes the so-called photometric channel of the instrument, on the other hand a fraction of the incident field can be returned thanks to a movable prism towards a dichroic plate, which separates the beam between two spectrography channels. In addition, a second light input channel for calibration, which reproduces the beam opening as well as the vignetting

### 2.3. SPECTROPHOTOMETRY: THE SNIFS INSTRUMENT

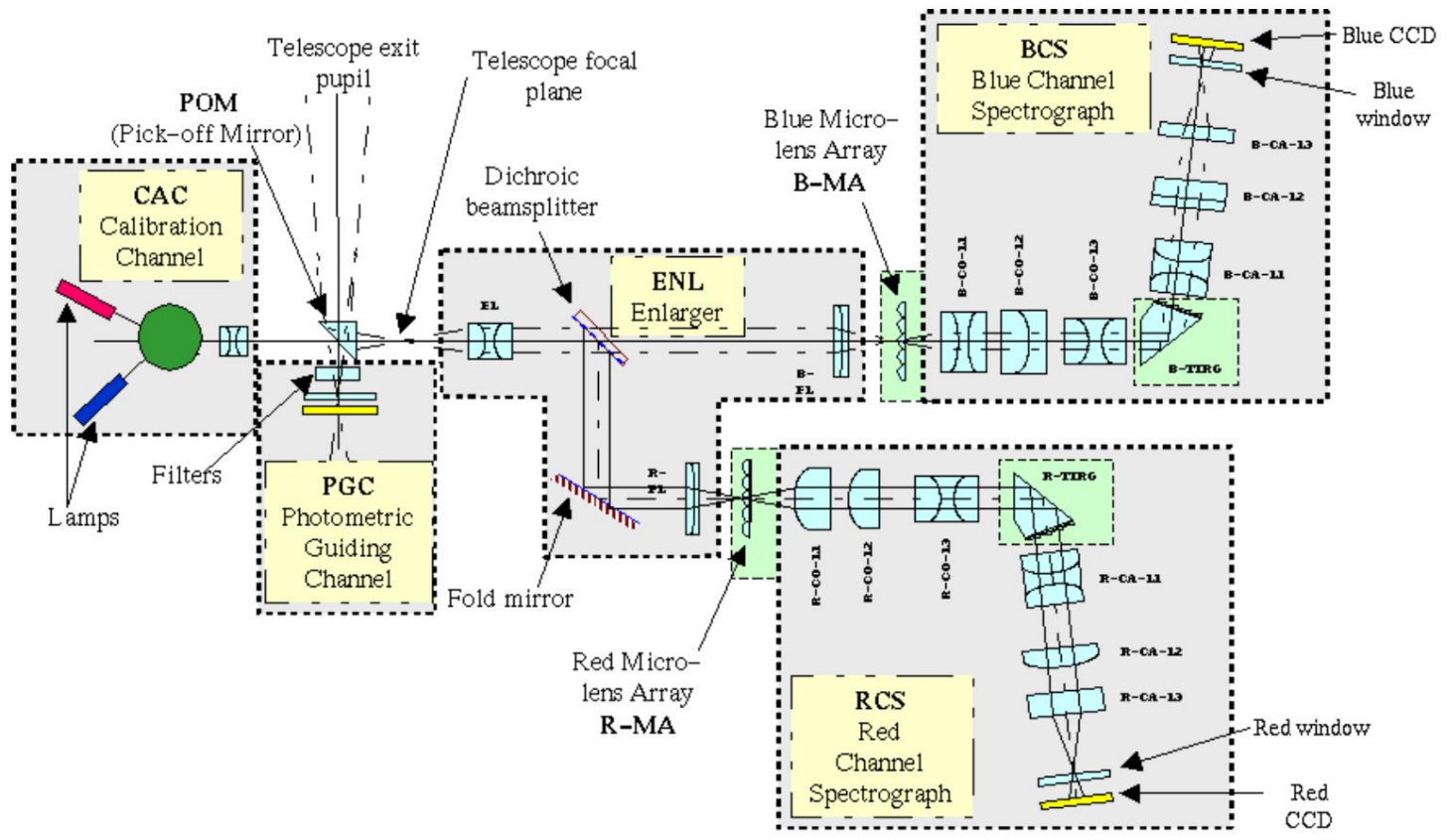


Fig. 2.4: Optical diagram of the SNIFS instrument.

when the reflecting prism is removed to illuminate the spectroscopy channels with lamps, either continuous spectrum or arc.

The spectral range is from 3200 to 10000  $\text{\AA}$ , which covers the entire extended visible range, in order to sample the largest possible part of the spectral structures of supernovae. Over such a range of more than one octave, it was necessary to make two channels, separated by a dichroic with a cut-off wavelength at 5400  $\text{\AA}$ . A 15x15 microlens array covering 6"  $\times$  6" then cuts the incident field into as many spaxels and the image of the corresponding micropupils is diffracted by a grism, blazed so as to optimize the flux in order 1 at the average wavelength of the channel considered, before being projected onto a CCD detector, with a rotation angle of 3.8 $\text{\AA}$ , so that the 225 spectra do not overlap on the detector. Each channel is optimized in its surface treatments and its optical design with respect to the wavelength concerned, the blue channel being sampled at 2.4  $\text{\AA}$ , the red channel at 2.9  $\text{\AA}$ , in order to respect the Shannon criterion for spectral resolution.

The photometric and guidance channel (see Figure 2.5) fulfills several roles. It is used to make the observed fields coincide with the finding charts when acquiring a new target and to image a reference field not far from the object studied in this field, as well as to perform their photometry in order to have the coefficients allowing the calibration of the exposure in relation to a reference exposure taken during photometric night. In order to monitor the absorption by the atmosphere in different

<sup>2</sup>Point Spread Function, related to atmospheric turbulence, pointing control and optical aberrations.

## CHAPTER 2. NEARBY SUPERNOVA FACTORY

---

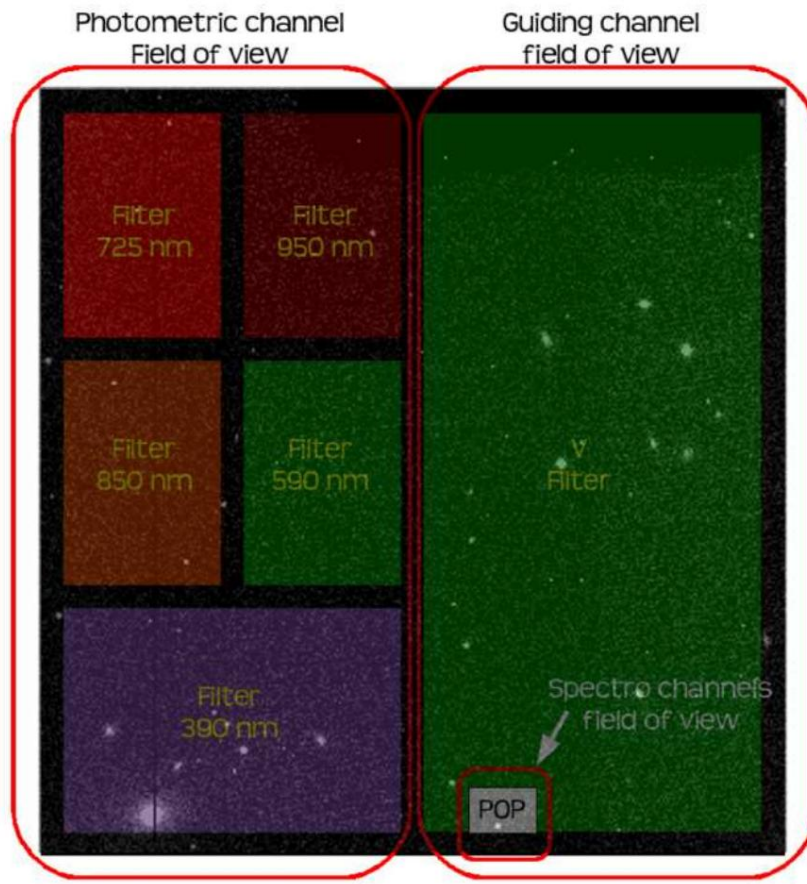


Fig. 2.5: Schematic of the photometric path. On the left, the CCD equipped with a multifilter, on the right, the guide path, with indication of the location of the deflecting mirror (POP).

wavelengths, this channel is equipped with a multifilter. Furthermore, since the instrument is mounted on a folded Cassegrain focus, it is necessary to ensure guidance with the same instrument as the measuring one, the usual guide channel of the telescope not receiving light because of the deflecting mirror. The photometric channel is therefore double, composed of two adjoining CCDs, one used for photometry, the other for guiding and clocked rapidly during the exposure. The field covered by these two CCDs is  $9.4 \times 9.4$  oversampled at  $0.14''$  per pixel, in order to be able to precisely measure the shape of the PSF.

This instrument was mounted on the UH telescope in Hawaii in 2004, during a long-term mission followed by 3 months of commissioning, during which the acquisition scripts had to be tested in situ. Science data collection began in 2004, but the actual mode of operation was not stabilized until 2006, with a rate on the sky doubled compared to the initial estimates: we observe for 40% of the telescope time, with one night of observation every 2 or 3 nights, and a winter break typically from December to March.

Winter nights are certainly longer, but experience has shown us that weather conditions lead to a high rate of lost nights.

---

## 2.4. DATA COLLECTION

### 2.4 Data collection

#### 2.4.1 The various types of poses

The data taken by the instrument are of several types: on the one hand, science exposures on supernovae, which consist of an initial rapid acquisition of the object, a comparison with the pointing charts in order to place the object in the spectrograph field and followed by an acquisition of spectra for typically 30 minutes, and on the other hand, exposures intended for calibration. Figure 2.6 shows as an example a sample of these exposures concerning the supernova SNF20080522-000 taken on June 5, 2008, in the red channel of the spectrograph, and which will serve as a guideline in this chapter. Calibration exposures are of several types:

- BIAS and DARK exposures : these are exposures during which the CCDs are read without having been illuminated. They are ideally taken at night - because of possible light leaks into the instrument - when the telescope is closed due to bad weather. In practice, light leaks are negligible except when the dome is open in broad daylight, and these exposures are also taken during the day, in particular to regularly drain the CCDs;
- ARC exposures : these are exposures during which the instrument is illuminated by arc lamps , argon for the R channel, mercury-cadmium for the B channel, in order to locate the positions of the spectra on the CCDs. Indeed, the movements of the telescope induce mechanical flexions in the instrument which can cause displacements of up to 6 pixels, which is the order of magnitude of the interval between two spectra. Also, these exposures are used to finely calibrate the spectra in wavelength. However, the studies we have carried out show that there is a mechanical hysteresis, and that it is not possible to tabulate the centroids of the arcs by tilting the telescope outside of dark time. It is therefore necessary to have one ARC exposure per science exposure;
- CONTINUOUS exposures : these are exposures during which the CCDs are illuminated by continuous spectrum lamps. These exposures are used to provide a relative flux calibration of the 225 spectra of each channel. This calibration will depend on two components: the first is a transmission of the instrument considered as fixed during a given night, and obtaining a micro-lens response curve by micro-lens is done thanks to a limited number of exposures, taken at the beginning, middle and end of the night: it is indeed necessary to limit the time devoted to these exposures which takes up the science acquisition time. Furthermore, the dichroic filter is sensitive to variations in atmospheric humidity, and the adsorption of water molecules will slightly shift its bandwidth. The correlation between its variations and the humidity measured by a probe does not, however, allow for an off-line correction, and the most robust method consists of measuring the bandwidth in situ by acquiring a CCD area reduced to around ten spectra — which allows for a rapid reading — during the comparison stage of the current pointing of the telescope with the pointing charts;
- DOME poses : the internal calibration channel of the instrument does not allow the photometric channel of the instrument to be illuminated to calculate uniformity (or flat field) corrections. This was the mission of DOME-type exposures, in which an external lamp illuminates the dome (with a reflector screen before the latter is torn off by a gust of wind) which is imaged by the instrument. However, internal reflections did not ultimately allow uniform illumination to be obtained, which complicated the task of photometric reduction ([Pereira, 2008](#)). DOME exposures also allow comparison of the fluxes of the photometric channel with those of the spectrograph, which has given rise to some ad hoc studies. Moreover, unlike internal calibration lamps which saturate the channels

## CHAPTER 2. NEARBY SUPERNOVA FACTORY

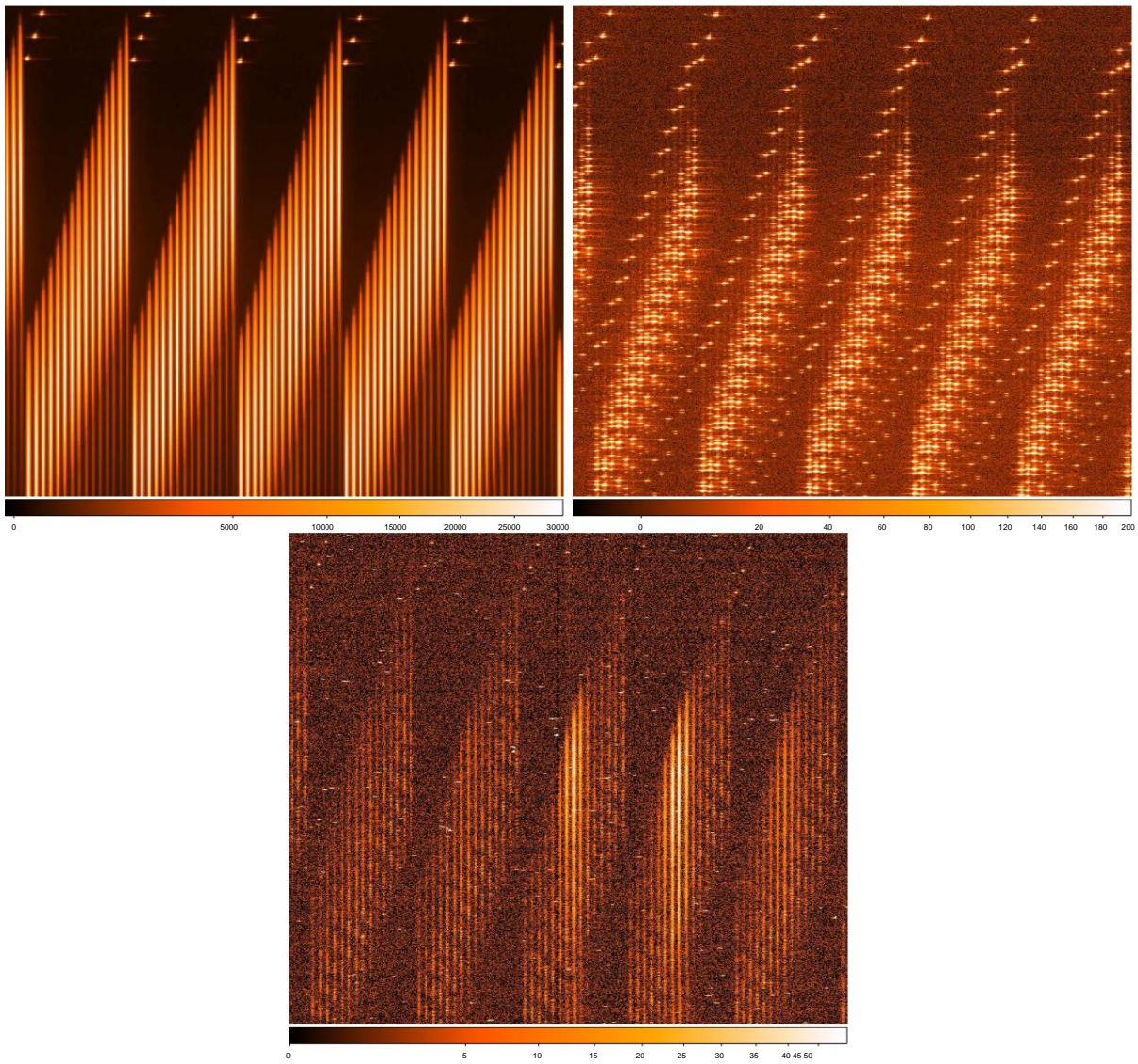


**Fig. 2.6:** Appearance of the different spectra projected onto the CCDs in the red channel. At the top left, a calibration pose using a continuous spectrum lamp. We observe at the top of the pose of the order 0 of diffraction, and at the bottom a residue of order 2, visible on a high-resolution image light intensity. The 225 SNIFS spectra are arranged in packets of 15 so as not to overlap. Top right, a pose using an ARC lamp, intended to adjust the position spectra with respect to known wavelengths. A careful eye will be able to see the presence of a diffuse background, linked either to parasitic reflections of light in the spectrograph, either to long-distance effects of the PSF of the spectrograph. Below, a science pose: we observes that only the spectra of the medium have a high signal-to-noise ratio, linked to the presence of an object centered in the field. On the side, the spectra have some bright lines: these are rays of the sky. Finally, many cosmic stars are also visible in the form of points white. The vertical scale has been compressed on all these images to show all orders of diffraction.

## 2.4. DATA COLLECTION

---

spectroscopy in a few seconds, DOME exposures have a possible exposure time of up to 1000 seconds, which is ideal for studying the linearity of detectors;

- SKY exposures : unlike DOME exposures , the incident light flux of these exposures cannot be controlled. They are nevertheless used to qualify the quality of the flat field obtained after calibration by CONTINUOUS exposures . However, they are not part of the automatic data reduction chain and are only used for control purposes;
- StdStar exposures : these exposures are not a particular type of exposure, as they are scientific exposures, but for which the spectro-imaged object is a spectrophotometric standard star. These stars fall into two categories: 29 long standard stars, including white dwarfs absolutely calibrated via a theoretical model such as GD71 ([Bohlin, 2007](#)), with exposure times greater than 100 seconds, and 10 bright standard stars, with exposure times of 1 s, from the HR catalog. These stars are used for the absolute flux calibration of the instrument, which is done via a modeling of the atmospheric transmission.

This allows us to obtain a transmission model per night of observation. Furthermore, repeated measurements of these stars—we have around 200 measurements for the main ones—allow us to verify the quality of our photometric calibration, by considering them as if they were Supernova type and by comparing the stability of their light curves;

- FinalRef exposures : these are in fact scientific exposures taken one year after the detection of the supernova, intended to provide a reference for the host galaxy of the latter. Indeed , the final step in data reduction is to separate the contributions of supernovae from those of their host.

### 2.4.2 Instrument Operation

All of these various poses are managed through a schedule established each night and read by an automated instrument control script, AIC, which sequentially calls sh scripts that schedule the sequences of logical instructions, sending low-level commands to software agents through the director system. There are 5 of these agents, three of them control the instrument's CCDs through a lotuspci card that communicates with a LeachBox, one of them is an interface agent with a PC104 that controls the moving parts of the instrument, filter wheel, deflection mirror, collimator focusing motors and cameras, as well as the lighting of the lamps, and finally, a last agent communicates with the telescope control system, the piloting of which is therefore totally automated, the human operators (TO) being there only for operations requiring privileges, such as reinitializing the system or deactivating the safety features linked to a defective probe.

Data collection is done remotely, via 3 computers at the summit accessible by a dedicated gateway, made necessary by the frequency of computer attacks against the official gateway of the telescope, which run VNC servers. A chat channel using the commercial system AIM allows shifters to communicate with each other, as well as with the TO. This channel also has Crowbot ([Poon et al., 2008](#)), a robot used for the transmission of high-level information as well as for recording conversations, the parameters passed by the scripts also being recorded, but directly at the data collection level. An electronic logbook system is also in place to report the status of scheduled operations, and serve as a starting point for overnight post-processing operations.

Finally, an online data processing and data control system was implemented to provide direct analysis elements to shifters. SNfactory was thus a pioneering experiment in the remote control of its instruments ([Antilogus et al., 2008](#)).

## CHAPTER 2. NEARBY SUPERNOVA FACTORY

---

### 2.4.3 Online data quality

In the context of online data quality monitoring, the speed of processing and issuing an alert is crucial, in order to allow the observer to have rapid feedback, ideally before having started the acquisition of a new pose which risks being affected in the event of a failure. The first level of online analysis therefore turns on the preprocessed data and uses a statistical analysis of the histogram of the values observed on the CCD pixels. Indeed, as shown in Figure 2.7, the shape of this histogram depends on the type of pose observed, and certain quantities will be relevant to define an illumination level of the pose. The analysis uses the following data:

- The average level after cutting at 5 $\sigma$ , which is representative of both the level of the poses

**BIAS** and **DARK**, but which can also spot a significant sky background;

- The level corresponding to the quantile of the 1% brightest pixels, representative of the level in poses with continuous spectra, such as **CONTINUOUS** poses, **SKY** poses and **DOME** poses.
- The level corresponding to the quantile of the brightest 1% pixels, indicative of the level of certain poses of science;
- The level corresponding to the quantile of the 10 $\sigma$  brightest pixels, representative of

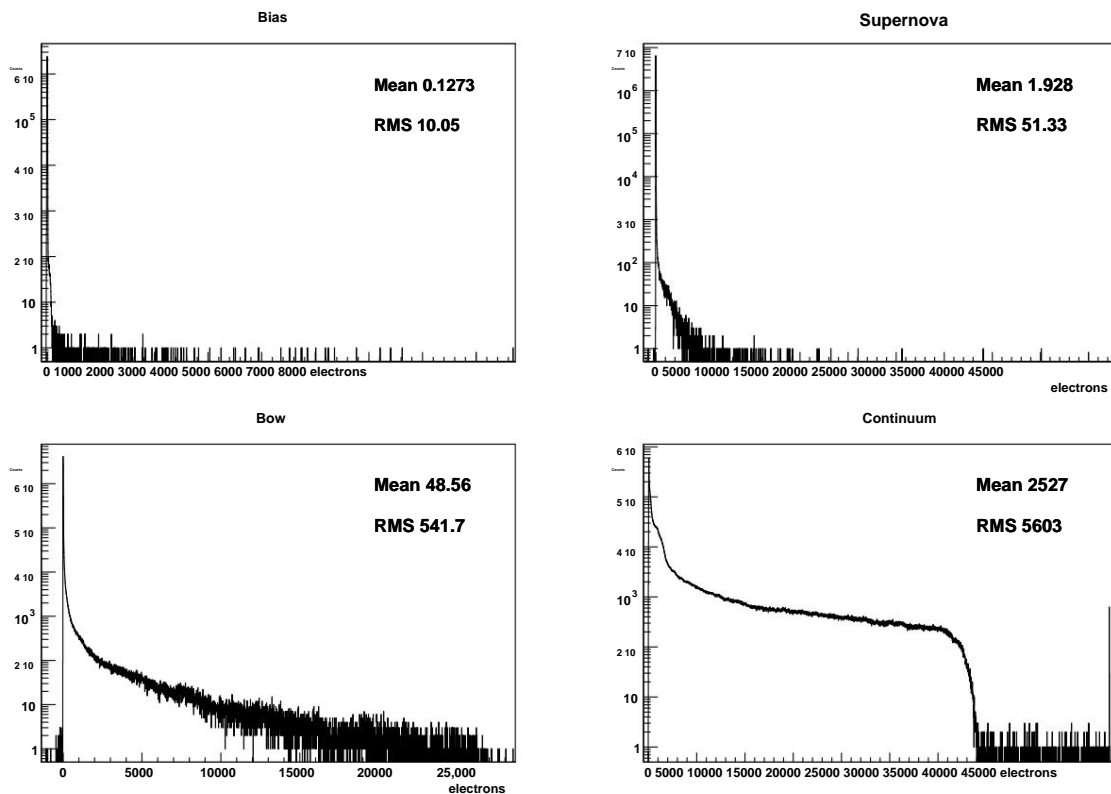


Fig. 2.7: Histograms of the signal observed on all CCD pixels as a function of the exposure type. The peak around 0 corresponds to the non-illuminated pixels, while the shape of the histogram of the illuminated pixels depends on the exposure type. The tail of the distribution contains both pixels affected by cosmic rays and so-called hot pixels with a high dark current. Finally, for **CONTINUOUS** exposures, the logical saturation linked to the 0th order of diffraction is observed at approximately 47,000 electrons.

---

## 2.5. DATA REDUCTION

some science poses, as well as Arcs poses;

- The number of saturated pixels, knowing that the presence of orders 0 of the diffracted beam implies that their number is non-zero, typically up to  $10^3$  ; – The noise level measured in the overscan (see chapter 3, supposedly stable; – And finally the number of pixels whose level is lower than the average minus  $5 \sigma$ , a number which should ideally be lower than  $10^3$  taking into account the non-Gaussianities of the incident signal.

A set of approximately 100 cuts has been established, allowing the detection of the most common major operating faults, including saturation of the physical signal, calibration lamps that no longer work, or the presence of corrupted exposures during their reading. The only error that cannot be detected with certainty is the absence of an object at the spectrograph input, the presence of sky lines can be confused with a signal before extraction: at most, it is possible to issue a "Warning" when the detected level is too low. Quality control therefore includes, but in a second step, manual control by the observer of the spatial vignettes of the signal reconstructed in the cube.

The online data quality system is also interfaced with the offline database. line, in order to label poses deemed bad and remove them from the reduction pipeline.

## 2.5 Data Reduction

### 2.5.1 Image processing

SNfactory data reduction is achieved through a cascade of elementary processes that fit together to form a reduction pipeline. The first step, called preprocessing, consists of subtracting the instrumental signatures of the CCDs from the raw exposures. We will detail this step further in Chapter 3. Once these signatures have been subtracted, the signal deposited on the CCD is calibrated in electrons per pixel. The result of the resulting exposure for SNF20080522-000, for the night of June 5, 2008, also called night 157, is shown at the bottom of Figure

Before moving on to the actual cube extraction step, stray light must be subtracted.

This process is actually ill-defined, as ideally, it would be necessary to adjust at the same time

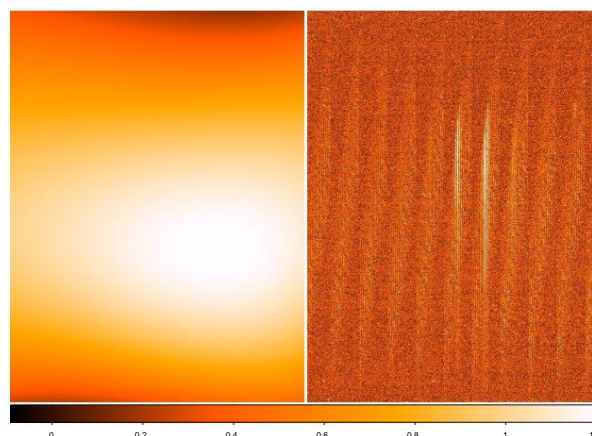


Fig. 2.8: Left: Stray light map for the science pose. It should be noted that the maximum amplitude of the stray light does not correspond to the maximum amplitude of the incident light (right), which makes the simple explanation by a poor consideration of the wings of the PSF implausible .

## CHAPTER 2. NEARBY SUPERNOVA FACTORY

---

the extracted signal and the continuous background noise by minimizing the subtraction residuals at the pose. However, extracting spectra one by one is already a computationally intensive process , and such a global minimization has not been considered for practical reasons. Therefore, an ad hoc treatment is applied, which consists of passing a minimum filter after a median filter to search for local minima with a window large enough to encompass the signal-free regions located in the inter-spectrum between two sets of 15 microlenses. A spline interpolation is then performed in the regions around these local minima, restricted to a signal height of  $\pm 3\bar{y}$  around the median of the region. We estimated the zero bias of this procedure at 0.2 electrons, while at high signal, the amplitude of the subtraction is of the order of 2%. Nonlinearity studies carried out by Monte Carlo simulations no longer seem to implicate this step of the process at the end of the calibration chain as a source of nonlinearity. An example of the reconstructed pattern of the diffuse light in the science pose already taken as an example is visible in figure 2.8, the maximum amplitude being 1.2 electrons, for an incident signal sharp at 78 electrons.

### 2.5.2 Reconstruction of the cube

The extraction of spectra to produce the 3D cube was the responsibility of Y. Copin, and is described by numerous SNfactory theses, we refer the reader to that of Nathalie [Blanc \(2006\)](#) for a condensed version, or to that of Yannick [Copin \(2000\)](#) in the context of another instrument for a more detailed version. We will limit ourselves here to saying that the ARC pose associated with the science pose, after having been preprocessed, is analyzed in order to determine the offset with respect to a reference ARC pose. This shift is then used to shift the optical model which gives  $C(i_0, j_0 | \bar{y}, l)$ , the centroids in CCD coordinates associated with the lens  $l$  for the wavelength  $\bar{y}$ , as well as the horizontal profile of the associated PSF, called cross-dispersion,  $G(i | \bar{y} | i_0 | \bar{y}, l)$ . A so-called optimal signal extraction is then applied which gives the reconstructed flux as a function of  $(j, l)$ , then interpolated in wavelength to give a flux as a function of  $(\bar{y}, l)$ . The ARC poses are then also extracted to refine the calibration

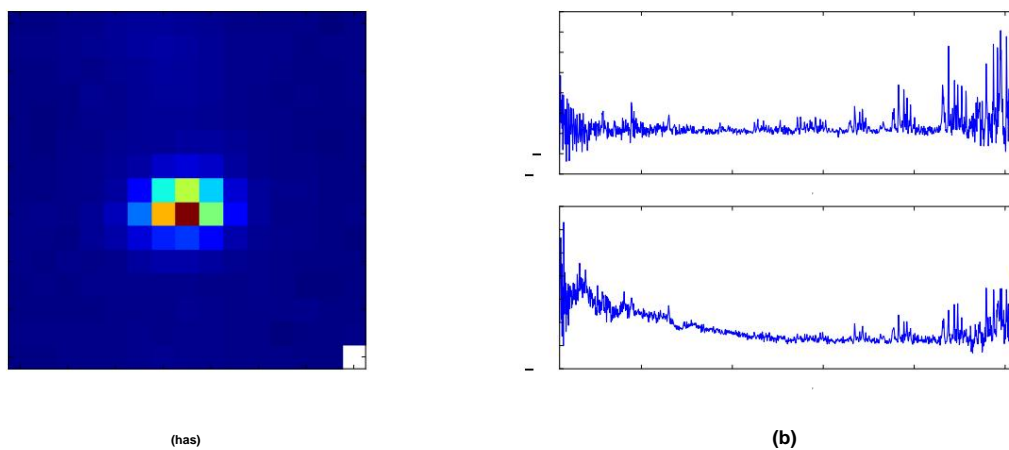


Fig. 2.9: The data cube after extraction and correction of the instrumental transmission. (a) Spatial appearance of the data in the cube, the supernova is visible in the center, the bottom right point suffers from vignetting and is therefore excluded from the data. (b) Example of spectra for two microlenses, the first in the sky area, and the second centered on the supernova.

---

## 2.5. DATA REDUCTION

---

in wavelength. The data obtained are then in the form of a cube with two spatial dimensions and one spectral dimension, and the flux is therefore of the form  $F(x,y,\ddot{y})$ .

The nighttime CONTINU exposures are extracted in the same way, and their flux is used to perform a spatial and spectral uniformity correction. A bandwidth correction for the dichroic plate is also applied in flight using the CONTINU exposure associated with the science exposure. Then, an anti-cosmic filter is applied: indeed, these being very localized on the CCD, they produce an aberrant point at  $(x,y,\ddot{y})$ . It would also be possible to remove the cosmics at the CCD level, but we defer the discussion to the next chapter. However, there remain fortuitous coincidences between cosmics in the data. Ultimately, the resulting data cube is flux-calibrated relative to a thermal lamp spectrum, thus without high-frequency components. Figure 2.9 shows the cube thus extracted from the data in our example.

### 2.5.3 Extracting the stream

The next step is to extract the spectra of astrophysical objects from the cube data, which most often consists of a point object, whether a supernova or a standard star, possibly superimposed on a diffuse background of a host galaxy in the case of SNIa. It is therefore necessary to have an algorithm to reconstruct the flux of a point source. For this, one of the major difficulties comes from the lack of knowledge of the spatial PSF, which is unknown a priori.

Another difficulty arises from effective atmospheric differential refraction (ADR), as integrated over the exposure time. A number of doctoral students have addressed this issue, particularly Nathalie Blanc, Sébastien Gilles, Guillaume Rigaudier, and Clément Buton.

Nathalie [Blanc's thesis \(2006\)](#) focused on extraction from data alone

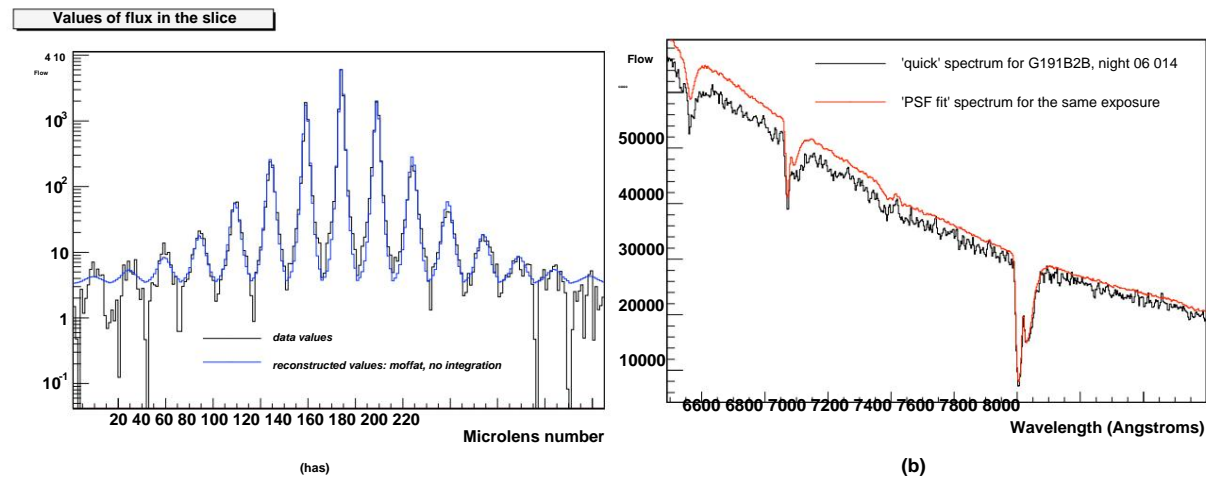


Fig. 2.10: Point source extraction: two figures summarizing Nathalie Blanc's thesis work . (a) Comparison of a Moffat functional form to data from a cube slice integrated in  $\ddot{y}$  : the spatial data of the cube are presented in the order  $x + 15 \ddot{y}$  so that they can be visualized in one dimension. (b) Comparison of the flux extracted by the PSF method with an aperture photometry method: the former not only gives a better signal-to-noise ratio, but also allows to reconstruct part of the flux lost out of field due to differential atmospheric refraction and the relatively narrow field of the spectrograph. (Figure N. Blanc thesis).

## CHAPTER 2. NEARBY SUPERNOVA FACTORY

---

of the spectrograph, and resulted in a flux reconstruction accuracy of 5 to 10%, using as the best functional form of the PSF an elliptic Moffat function with principal axes  $x$  and  $y$  (see Figure 2.10) : fortunately, these directions correspond to the cardinal axes to within a small angle, and the telescope being azimuthal mounted, this leads to a different guidance inaccuracy in the two axes, which justifies the approximation used. The ADR was reconstructed directly on the data using the air mass coefficient from the pointing information, and adjusting the projected direction in the plane of the spectrograph pose by pose. The flux extraction is done in two steps: in order to determine the PSF and ADR parameters, the cube is first integrated in wavelength in wide slices in order to improve the signal-to-noise ratio. Then, once the shape parameters are fixed, the flux extraction itself is done by a simple  $\hat{y}$  method<sup>2</sup>.

Point source extraction was subsequently improved (see Figure 2.11): Clément Buton empirically determined a better functional form, in the form of a Moffat function representing the atmospheric PSF (also called seeing) plus a Gaussian, representing additional errors, notably from guiding. An empirical relationship established between the parameters of the Moffat and the Gaussian, probably linked to a feedback between seeing and pointing accuracy, allows reducing the number of parameters to be adjusted. However, using the same data to adjust the PSF and extract the flux is a non-linear procedure, not free from bias. The ideal would be to be able to transpose the PSF measured in the photometric channel to spectral flux extraction. For this, two approaches have been developed, one empirical, which consists of using the functional form of the PSF of Clément Buton, adjusting its parameters on the photometric channel, and deducing a correlation law with the same parameters measured in the spectrographic channels. This method currently allows to give a good starting approximation for the adjustment, of the order of 3–4%. Because of the field curvature that induces spatial variations of the PSF related to optical aberrations, another approach would be to determine a complete optical model of the telescope, and to convolve the results with an atmospheric PSF as well as that coming from the guide to then transport

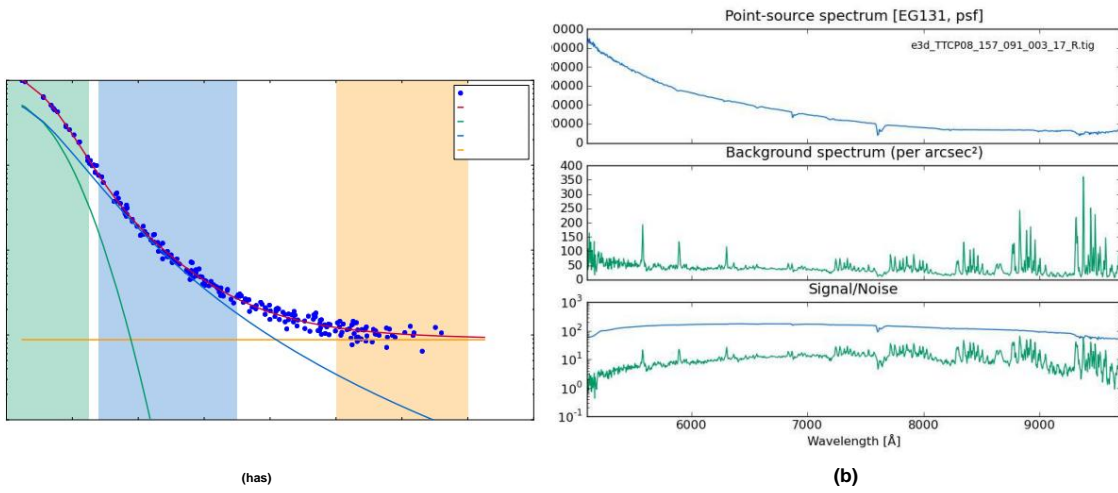


Fig. 2.11: (a) Functional form currently in use for spectro-spatial PSF fitting (Figure C. Buton thesis). (b) Spectrum extracted from EG131, a standard star taken on the same night as the example pose of SNF20080522-000: at the top is given the flux of the object in arbitrary units, in the middle the flux of the sky background, and at the bottom the signal-to-noise ratio.

## 2.5. DATA REDUCTION

---

the parameters in the spectroscopy field. A first study was carried out by Guillaume Rigaudier, but for the moment this complex process is not sufficiently developed to allow exploitation in production.

### 2.5.4 Calibration

Once the flux is obtained, it remains to determine its absolute calibration. The latter is based on the measured flux of standard long stars of the night, compared to their reference tables, in order to measure atmospheric absorption object by object. By exploiting the fact that standard stars are taken at different air masses ([Buton, 2009](#)), it is possible to determine the different components of atmospheric absorption: Rayleigh absorption, fixed according to atmospheric pressure, absorption by ozone, by aerosols, as well as absorptions linked to telluric lines, H<sub>2</sub>O and O<sub>2</sub>. Figure [2.12](#) shows the implementation of these adjustments for the night that we follow as an example.

Once the atmospheric correction has been carried out, it is still necessary to return to an absolute calibration in flux: in fact, the flux solution is done relatively to a gray absorption coefficient. Using the flux ratios of objects in the photometric channel between the poses taken in photometric night and those taken in non-photometric night allows this degeneration to be removed ([Pereira, 2008](#)). Figure [2.13](#) illustrates how this step works.

### 2.5.5 Galactic Subtraction

Now that the data are flux-calibrated, the underlying galaxy still needs to be subtracted. This step is still under development, and older productions used a linear diffuse background model, such as  $\hat{y}_{xx} + \hat{y}_{yy} + C$ , as subtraction, which was used instead of a constant background to model the sky in the point source extraction code. Galactic subtraction requires modeling the underlying galaxy. To do this, the poses must be spatially aligned, which is not very difficult as long as the supernova is present, but becomes tricky when working on the final reference pose: in fact, for the latter, the positioning must be deduced from the shift observed in the photometric channel between this pose and the poses with the visible supernova. However, the non-reproducibility of the positioning of the deflection prism, the POP, only allows spatial alignment with a resolution of 0.3 arc seconds, which is limiting for establishing the model. The latter (S. Bongard, submitted) is established in an area which exceeds the field of observation: in fact, it is on the one hand straightened by the ADR, and on the other hand, the wings of the PSF involve a part of the flow which is located outside the field. Of course, the reconstructed out-of-field part is done with low precision, but since only the part that will enter the field and pollute the supernova because of the PSF tails is important, in the end, it is not a problem. Figure [2.14](#) shows the model established for the host of the supernova SNF20080522-000 taken as an example. The application of this model does not result in spatially structured residues when extracting the flux of this supernova, which is done on the same model as the extraction of the flux of standard stars, but after subtracting the galactic model convolved by the current PSF.

### 2.5.6 Analysis of light curves

We now have for each observation epoch a spectrum calibrated in flux and subtracted from the contribution of its host galaxy: this gives the basic object of supernova analysis, the spectrotemporal series, presented for SNF20080522-000 in Figure [2.15](#). From this series, it is possible to analyze the data in a way representative of what is

## CHAPTER 2. NEARBY SUPERNOVA FACTORY

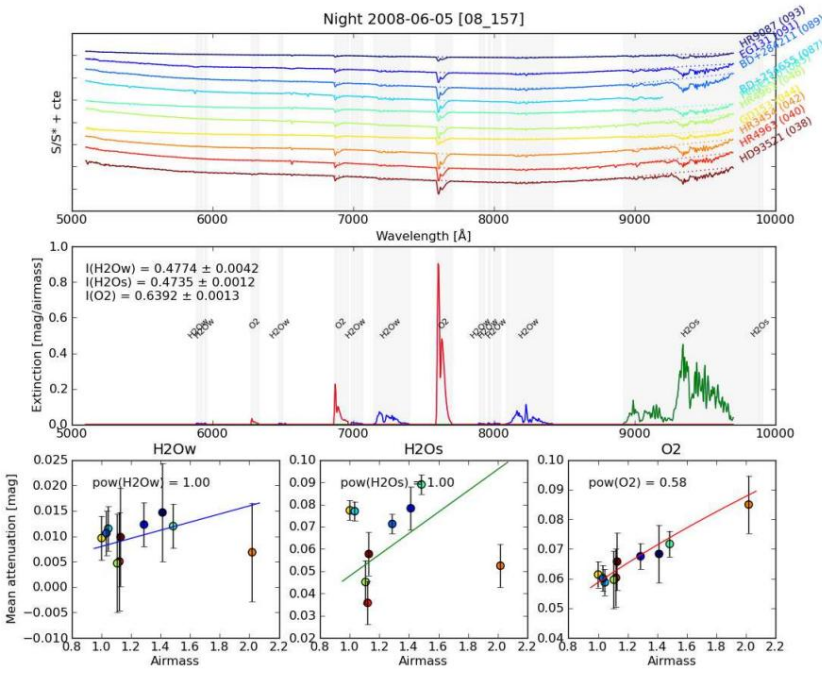
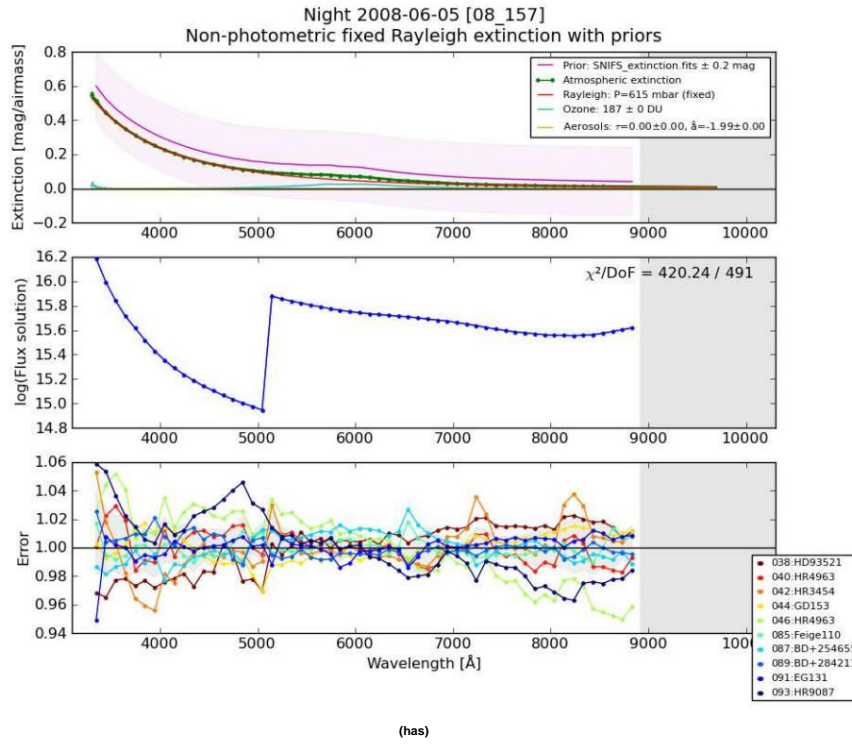


Fig. 2.12: (a) In the middle, the adjusted form of atmospheric extinction, in the middle, the flux solution, which represents the multiplicative coefficient to be applied to the extracted spectra to obtain an absolute calibration, and at the bottom, star by star, the error in the model. (b) : determination of the absorption by telluric lines: for each group of lines, the attenuation is calculated as a function of the air mass, before applying the adjusted model as a correction.

## 2.5. DATA REDUCTION

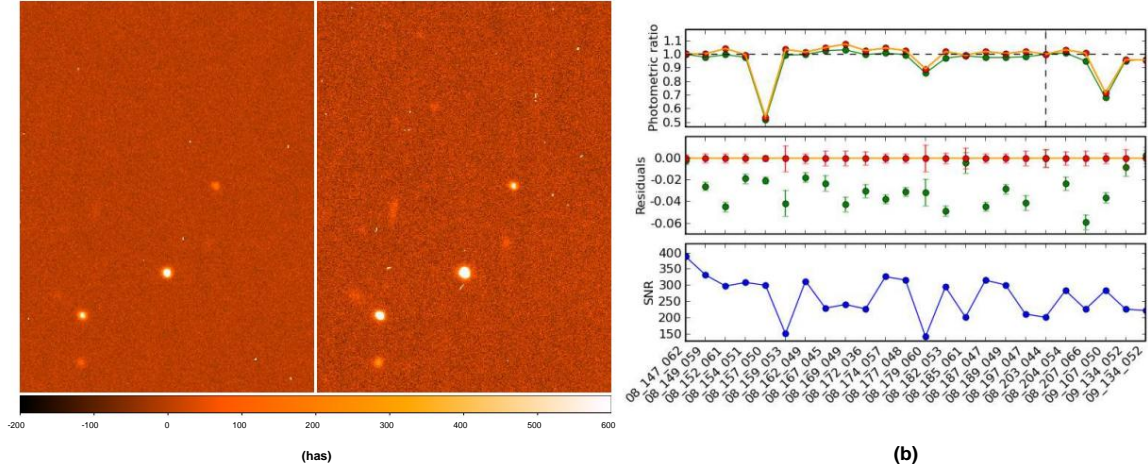


Fig. 2.13: Photometric ratios: (a) comparison of filter 3 of the photometric channel between nights 157 and 203 of 2008, the first being that of our example, and the second that taken as a photometric night reference. The color codes are aligned, and we can see visually that the flux is weaker in the pose shown on the left, which is confirmed (b) by the calculation of photometric ratios along the light curve of the object that shows a absorption of almost 50% for night 157. Night 203, taken as reference, and indicated by dotted lines.

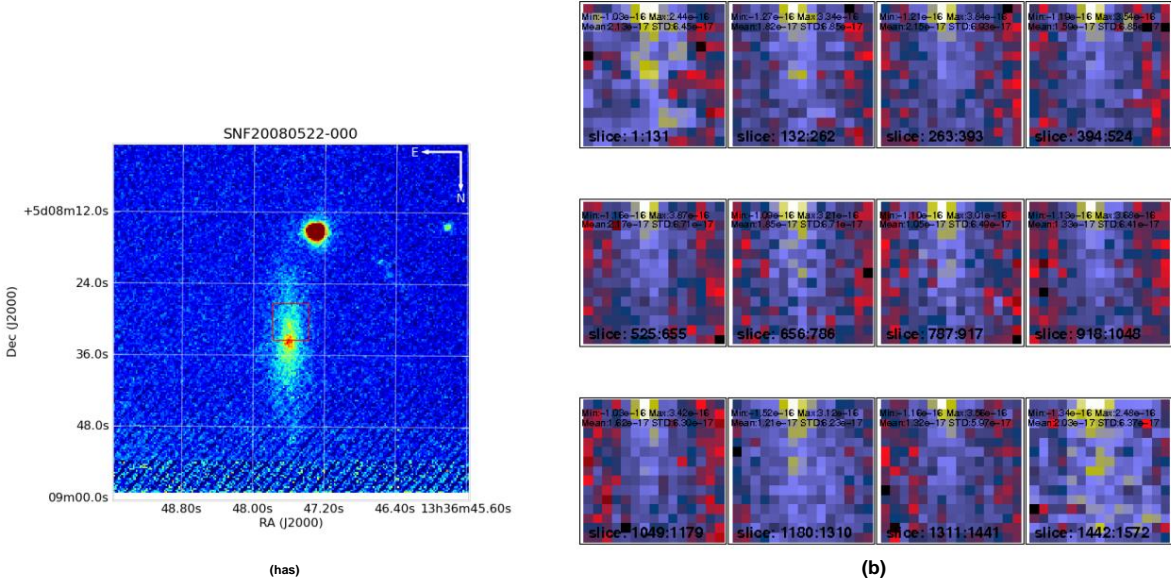


Fig. 2.14: (a) The acquisition images of SNF20080522-000, taken at the time of the point of the telescope, and added together. The position of the POP is shown by a red square, and we distinguish the integrated flux of the supernova. (b) The galactic model established for the subtraction, at various wavelengths: it is very similar to the flux observed in photometry because between the two images it is necessary to apply a transformation  $y \rightarrow \tilde{y}$

## CHAPTER 2. NEARBY SUPERNOVA FACTORY

---

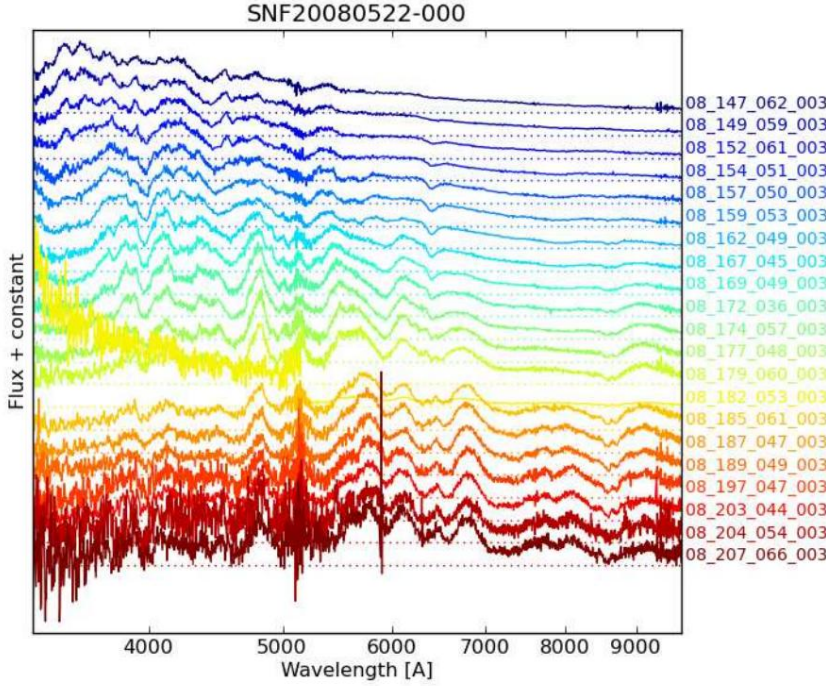


Fig. 2.15: Spectral time series of SNF20080522-000. An arbitrary flux shift between the spectra was applied. One of the spectra, in yellow, corresponds to a night when channel B flux extraction failed and will be discarded in the next step, light curve fitting .

made in the photometric surveys: it is sufficient to integrate the spectra in synthetic filters, of the slot type, chosen in order to cover the entire spectral domain, except the region polluted by the telluric lines of water beyond 9200  $\text{\AA}$  as well as the region centered on the cutoff of the dichroic plate, from 5100 to 5200  $\text{\AA}$ . The filters retained are presented in table 2.2 and the light curve of our supernova in figure 2.16. Once these data are obtained, a SALT2 type adjustment (Guy et al., 2007) makes it possible to determine the parameters of the light curve, and once all these are obtained, to minimize the residuals in the Hubble diagram presented in figure 2.17. These are ultimately 0.15 mag, or of the same order of magnitude as what is observed by other groups on their batch of supernovae.

### 2.5.7 Data quality

This number is not sufficient on its own to determine the quality of our data, however: in fact, it includes a dispersion on the magnitudes of the supernovae. To determine an order of magnitude of the flux uncertainty on the spectra of the spectro-temporal series, two means can be used, knowing that the statistical uncertainty linked to photo noise and reading noise is typically of the order of 0.3% and will in practice be negligible in the uncertainty balance. The first method consists of studying the standard stars as if they were

<sup>3</sup>Throughout this work, the 2007 version of SALT2 is used, even though the latest version of the code analysis now uses version 2010.

## 2.5. DATA REDUCTION

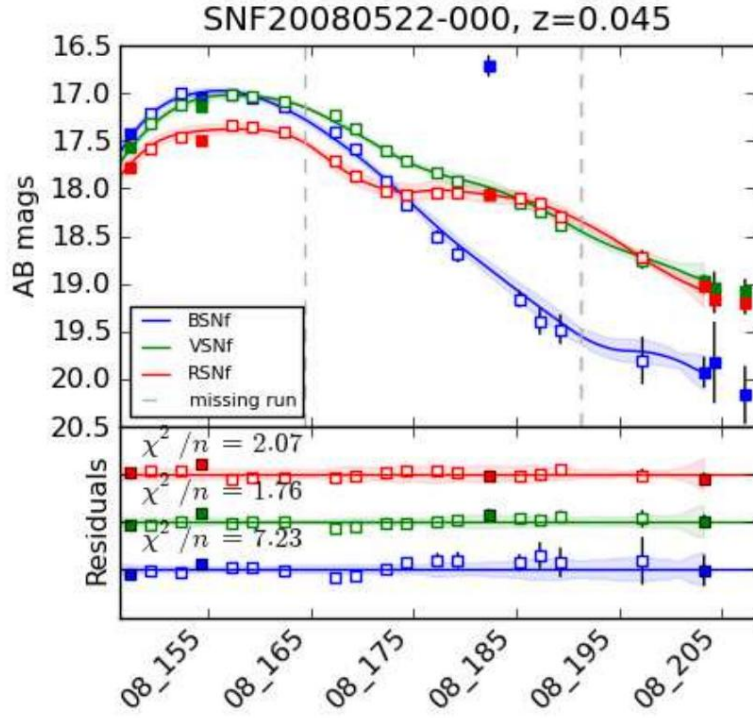


Fig. 2.16: SALT2 fitting of the light curves of SNF20080522-000. Only the bands BSNf, VSNf and RSNf are used in the adjustment

Tab. 2.2: Definition of SNfactory filters, and quality of data measured in these filters. first column contains the name of the filter, the second, its limits, the third, the standard deviation observed during repeated observation of standard stars, the fourth, the non-linearity observed on an underexposed star (see text), the fifth, the standard deviations at the SALT2 adjustment, and the last, the residues obtained by the method given in paragraph 4.3.2. The data are taken from the production called internally NEVADA/ACES. Below: the same data in color, showing that there is a strong correlation between the various bands.

Filtered	RMS terminals (std) (HAS)	Non-line. mag	RMS (SN) mag	RMS (SN) ' magazine	
USNf [3200,4102]		0.031 + 0.047	0.064		
BSNf [4102,5100]		0.029 + 0.046	0.042	0.066	
VBNf [5200,6289]		0.028 + 0.097	0.047	0.059	
RSNf [6289,7607]		0.028 + 0.072	0.044	0.061	
ISNf [7607,9200]		0.03 + 0.085	0.060		
color	RMS (std)	RMS (SN)	RMS (SN)'		
USNf-BSNf	0.014			0.053	
BSNf-VSNf	0.013		0.065	0.039	
VSNf-RSNf	0.006		0.051	0.030	
RSNf-ISNf	0.008			0.045	

## CHAPTER 2. NEARBY SUPERNOVA FACTORY

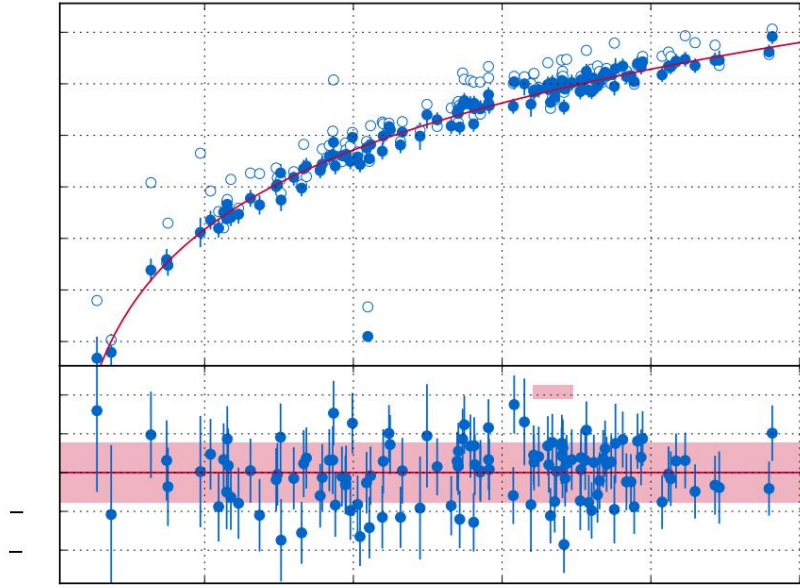


Fig. 2.17: Hubble diagram obtained using the classical standardization method. Open circles show data before  $x_1$  and color correction, and solid circles after correction. The bottom panel shows the residuals from the fit.

supernovae, and to determine the observed standard deviation in magnitude<sup>4</sup>. Table 2.2 gives the results of the dispersion observed after cutting off the 0.9% of aberrant measurements at more than 0.2 mag. It is of the order of 0.03 mag, with a weak chromatic component, the standard deviations in color being of the order of 0.01 mag: the flux calibration procedure therefore produces essentially gray fluctuations.

However, this measurement is a lower bound on the uncertainty in supernova spectra : in fact, these are at lower flux and therefore potentially affected by non-linearity problems. To determine the latter, we have exposures of WD1413+257, a star of magnitude  $g=16.7$ , which we have underexposed by a factor of 20, in order to simulate an observation of magnitude 20, the limit of our instrument. The study after data reduction reveals in the low intensity poses a systematic underestimation of the flux, up to 0.1 mag in V. The origin of this non-linearity is not yet understood, and is the subject of intensive developments by the collaboration: it comes from one of the stages of data processing described above.

It is also possible to determine the quality of the data by using the residuals of the measurements to the light curves fitted by the SALT2 model: this estimate is however imperfect, because on the one hand the measurement points were used in the adjustment of SALT2,

<sup>4</sup>Some consider normalized absolute deviations (or nMAD) as good indicators, which reflect the width of a central Gaussian part of a distribution, reducing the weight of atypical events.

While this measure provides information on what could be gained by improving the treatment of outliers, it does not allow us to deduce the statistical properties of an average taken from the data. We will therefore only give standard deviations here, even if it means defining cut-offs on events considered as outliers to improve the final resolutions.

---

## 2.5. DATA REDUCTION

and on the other hand, the SALT2 model itself has its own modeling uncertainties. However, it takes into account all uncertainties that may have affected the data reduction, which in addition to the flux calibration are the galactic subtraction as well as the nonlinearities. The results in B,V,R give an uncertainty of the order of 0.06 mag, once outliers at more than 0.2 mag are rejected. This time they contain a non-negligible colored component, of the same order of magnitude as the uncertainty on the magnitude. We repeated this study using only the points at  $\pm 10$  days from the maximum, and adjusting the bands independently, as described in section 4.3.2 : we then observe an improvement in the precision.

The synthetic supernova photometry data were also compared with available published data from some CfA supernovae, and show a dispersion of the order of 0.05 magnitudes: there remains room for improvement in the data calibration. The final dataset consists of supernovae for which the nMAD of the residuals to the SALT2 fit is less than 0.1 mag, with at least 5 points on the light curve.

They are calibrated with an accuracy better than 0.06 mag, with a strong correlation between bands, and at the last data production, 135 supernovae passed these cuts, out of an initial batch of 194 objects.

## Contributions

The description of the SNfactory experiment is made through the conference reports of Aldering et al. (2002), Lantz et al. (2004), Antilogus et al. (2008) and the articles of Wood-Vasey et al. (2004) and Copin et al. (2006), of which I am a signatory except for the first. I myself presented the experiment and its general results at international conferences in Ringberg (2003) and Blois (2007) — the conferences on the more specific results being mentioned in chapter 4 — at seminars in Grenoble (2005) and Clermont-Ferrand (2006), and at the scientific councils of IPNL (2002) and IN2P3 (2007).

I participated in the SNIFS instrument setup mission (5 weeks in my case) and I worked on the acquisition scripts mainly developed by Pierre Antilogus. I notably contributed the online quality analysis code. During the data collection of phase I of the experiment, I was one of the three shift coordinators. The spectroscopic typing of supernovae resulted in 153 telegrams, and our supernovae are available on the collaboration's public website at the URL <http://snfactory.lbl.gov/>

Data reduction is a highly collaborative endeavor, and most of the figures presented in this chapter are the result of the work of S.J. Bailey, S. Bongard, C. Buton, Y. Copin, E. P'ecotal, R. Pereira, and myself. While I focused on CCD data reduction, I also poked around in several areas of the reduction, particularly with regard to stray light, point source extraction, and light curve fitting using SALT2. Point source extraction was one of the projects in Nathalie Blanc's thesis, which I co-supervised. Finally, Léonie Berge's TIPE internship focused on the characterization in Zernike polynomials of the defects of a parabolic mirror using the Foucault method, a subject largely inspired by the work of E. P'ecotal on the measurement of optical aberrations in the photometric pathway.

Finally, outside of SNfactory, I participated in a supernova search campaign in the Canary Islands in November 2002, which was unsuccessful due to bad weather. I also participated in writing the FIREBALL proposal.

## **CHAPTER 2. NEARBY SUPERNOVA FACTORY**

---

## Chapter 3

# Use and implementation of CCD for spectrography

### Summary

---

3.1 General principle of a CCD sensor . . . . .	42
3.1.1 Signal formation . . . . .	42
3.1.2 Hardware implementation . . . . .	43
3.2 Reception and qualification of SNIFS CCDs . . . . .	45
3.3 Instrumental signatures and preprocessing algorithm . . . . .	45
3.3.1 Pedestal . . . . .	45
3.3.2 Noise and playback artifacts . . . . .	46
3.3.3 Gain . . . . .	47
3.3.4 Cosmetic defects . . . . .	50
3.3.5 Charge transfer efficiency . . . . .	52
3.3.6 Bias . . . . .	54
3.3.7 Dark current . . . . .	55
3.3.8 Uniformity . . . . .	58
3.3.9 Remanence . . . . .	61
3.3.10 Cosmics . . . . .	61
3.3.11 (Non)-Linearity . . . . .	63
Contributions . . . . .	65

---

CCD sensors are one of the key elements of SNfactory because they are at the interface between the physical signal and the raw data. They were received in 2003 and integrated to the instrument in 2004, and have been operational since. There are no specifications to strictly speaking on the level of bias admissible after data reduction, but if we sets a final precision target of 1% for the spectra, this amounts to determining the level of bias depending on the expected signal-to-noise ratio. In practice, it becomes difficult to make corrections ensuring a bias less than 0.1 electron for a read noise of 3 e<sup>-</sup>, i.e. a signal-to-noise ratio limit of 2, but achieving such precision is necessary or even insufficient when it comes to eliminating sources of non-linearity on late spectra. Thus, The reduction method started in 2003 is not yet completely finished: we We will outline the main steps here.

## CHAPTER 3. USE AND IMPLEMENTATION OF CCDs FOR SPECTROGRAPHY

---

### 3.1 General principle of a CCD sensor.

There are many books on the operating principle of CCDs. For our part, we recommend [Howell \(2000\)](#) as a first approach . However, the reference book we used is [McLean \(1997\)](#), supplemented by [Cavadore and Dorn \(1999\)](#) and [Sorensen \(2000\)](#) who analyzed the same CCDs as us.

#### 3.1.1 Signal formation

Without going into all the technical details that the reader will find in the works cited above , a CCD is schematically a doped silicon sensor on the face of which a periodic array of pixels is heavily doped, creating a depleted zone by polarization under about thirty volts. An optical photon converting in the detector will give an electron, which will be trapped in the pixel closest to the conversion zone. A system of logic gates is etched on the surface which allows the charges to be transferred from one pixel to another. In our case, this transfer is conventionally done along the vertical direction, from top to bottom, and is synchronous for all the pixels of the CCD (see figure 3.1) : this is what we call parallel registers. At the top, the first row of pixels is connected to ground, which makes an effective reset during the shift. At the bottom, the pixels are transferred into a register called

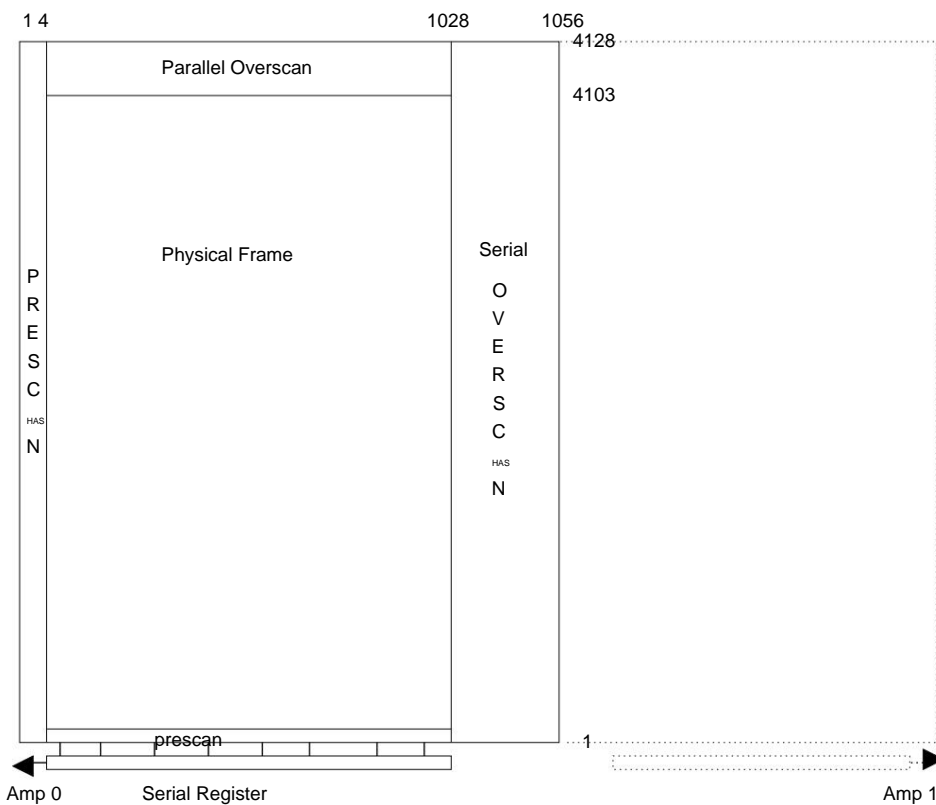


Fig. 3.1: Schematic layout of the various zones on a CCD sensor. The physical zone is enclosed in logical zones that correspond to additional clock pulses, compared to the physical zone, called pre- and overscan. The numbers correspond to the numbers of the rows of pixels where the transitions between the various zones take place, for channel B. The position of the zone read by the second preamplifier is indicated by a dotted line.

### 3.1. GENERAL PRINCIPLE OF A CCD SENSOR.

serial register, which will transfer the charges horizontally to one or more preamplifiers. Thus, between two clock pulses on the parallel register, the entire charge of the serial register is read, as well as a certain number of dummy pixels corresponding to a reading of the ground. The output signal is sent to a preamplifier on the CCD, which operates in correlated double sampling and adds a pedestal to the signal before sending it outside the CCD to an ADC which digitizes it.

#### 3.1.2 Hardware implementation

The four SNIFS CCD sensors are standard astronomy CCDs, EEV 44-82, 4056×2024 pixels, read by two amplifiers which therefore each read an image of size 4056×1024, pixel width  $15\mu$ , illuminated from the back, with a mid-height bandwidth between 3200  $\text{\AA}$  and 8500  $\text{\AA}$  for those which equip the B channel of the spectrograph as well as the two sensors of the photometric channel. The CCD of the red channel is of the deep depleted type, which allows a greater quantum efficiency in the red, and has a mid-height bandwidth of 4000  $\text{\AA}$  to 9400  $\text{\AA}$ . The price to pay, however, is a diffusion length greater than the pixel for electrons, which spreads the signal. The bandwidths come from the manufacturer's data: we only controlled them indirectly by calculating the overall transmission of SNIFS (see Figure 3.2). They were integrated into a cryostat by CCD for the blue (B) and red (R) channels, and the two CCDs for photometry and guidance (P channel) are attached to theirs. The guidance CCD, however, is only engineering grade, due to supply issues at the time of purchase. The integration was done by Lupino Inc. in Hawaii.

Cryogenics is provided by a Cryotiger-type system, which operates in a closed circuit—essential for continuous operations for several months—with a mixture of flammable gases based on Freons and covered by industrial secrecy. Cryogenics is also used to maintain the vacuum in the cryostats. However, after a typical period of one or two months, the vacuum begins to deteriorate, resulting in a temperature increase of approximately 10°C per month. Regular maintenance is therefore required.

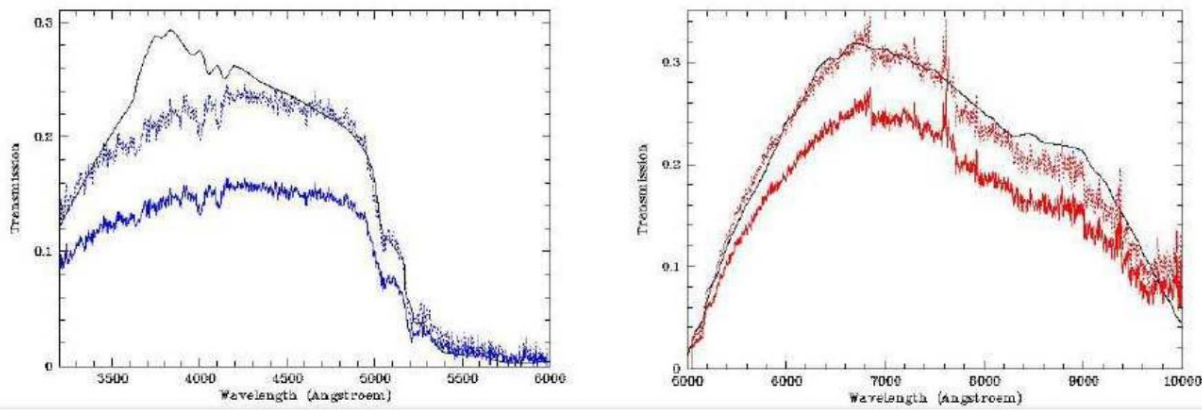
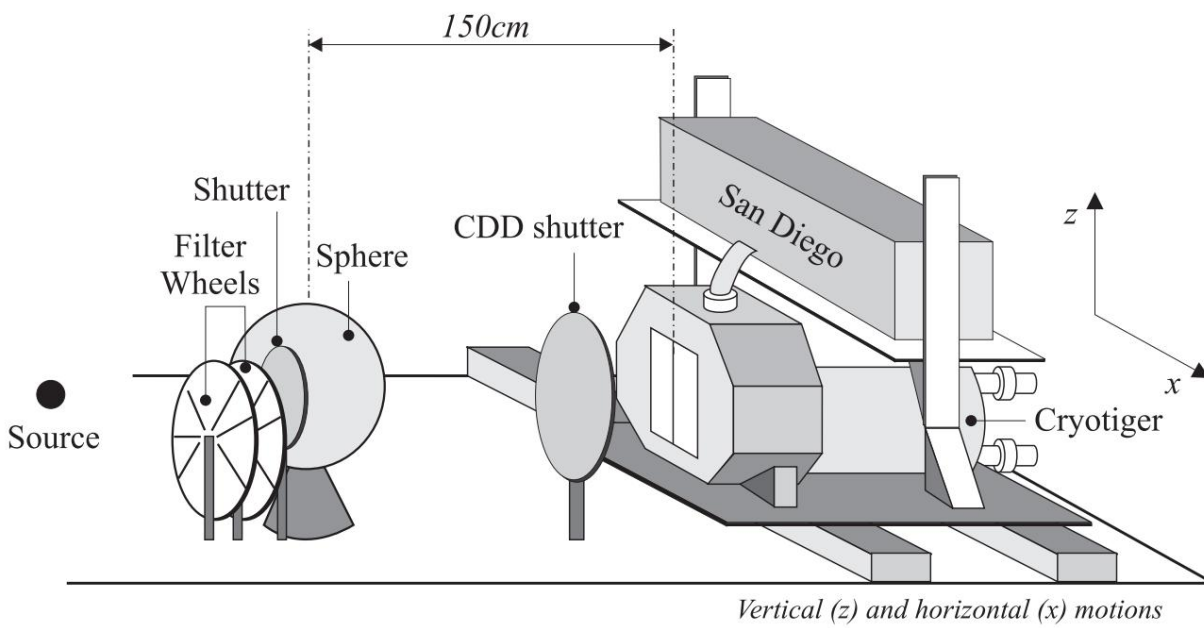


Fig. 3.2: Theoretical transmission of the instrument, in black, as well as the measured transmission, in solid blue or red lines corresponding to the two spectrograph channels. The dotted curves correspond to the measured curve scaled to the theoretical curve to within an adjusted multiplicative factor. The general shape of the curves coincides, apart from an unaccounted for deviation in channel B. The gray factor is partly attributable to the dust covering the telescope mirror. (Figure E. Pecontal)

## CHAPTER 3. USE AND IMPLEMENTATION OF CCDs FOR SPECTROGRAPHY

which consists of cycling the CCD, heating it so that impurities do not settle on it, pumping until the temperature returns to room temperature, then breaking the vacuum before pumping again and ensuring recooling. These operations are routinely carried out by a person from the University of Hawaii, when we notice a rise in temperature of the CCDs.

The output signal, along with the clock and high-voltage signals, is carried by a cable about 1 meter long to an SDSU electronic system (developed at the University of San Diego), including the clock cards and the video cards with a 16-bit ADC. It is powered by a switching power supply located in another box. The reading can be done at various gain and clock values; we use the highest gain, of the order of 1 ADU/e  $\circ$  and clock the reading at 50 kHz. SDSUs can also control a shutter, which is used in SNIFS to synchronize exposure times on the P channel, with exposures in the B and R channels being taken with 10 seconds of integration before the science exposure, and 10 seconds after. Communication with the LotusPCI cards of the acquisition PCs is done via optical fibers. The B channel is controlled by Detcom, an interface developed by Sidik Isani for the CFHT while the other two channels are controlled by otcom, developed by John Tonry of the University of Hawaii. These two interfaces are managed through the CFHT director system, which responds to shell commands sent by the scripts we have developed for this purpose (see paragraph 2.4.1).



**General layout of best bench**  
*(light-tight container not shown)*

Fig. 3.3: Schematic diagram of the test bench at IPNL. A black box, not shown, encompasses the integrating sphere and the entry window of the CCD cryostat (drawing by A. Castera).

### 3.2. RECEIPT AND QUALIFICATION OF SNIFS CCDs

## 3.2 Reception and qualification of SNIFS CCDs

The first CCD to be integrated was the one in the blue channel of the spectrograph. It was sent to France to be used to integrate the SNIFS optics into the CRAL, and was available for about 6 months at IPNL for preliminary tests. These were carried out on a dedicated bench from the IPNL instrumentation department, with the valuable assistance of Alain Castera, which included a light track with a servo-driven lamp, filter wheels, and a sphere integrator, which was placed inside a black box about 1.5 m long, sufficient to ensure uniformity of illumination at 0.1% and therefore to study inhomogeneities spatial CCD. The test bench was qualified with a commercial Hamamatsu CCD, and its schematic diagram is shown in Figure 3.3.

During the tests, a list of 13 sensor failures and weaknesses was established. Among the most important, a fluctuation of the random gain with an amplitude of a factor of 100 has was observed, as well as a cleaning of the inoperative CCD before an exposure. This led to resuming the integration of the CCD at the manufacturer, who had connected a voltage input to ground slightly negative! The CCD taken over, as well as the other CCDs once integrated, were quickly tested at the manufacturer, before being installed on the instrument, during integration in April 2004.

The data reduction algorithm was developed during these tests in Lyon, and refined to account for different reading software for other CCDs. We now move on review the processing performed on raw poses in order to eliminate instrumental artifacts.

## 3.3 Instrumental signatures and preprocessing algorithm

### 3.3.1 Pedestal

The first step in data subtraction involves the pedestal which is added before digitization in order to avoid negative conversions by the ADC. The level of this pedestal is fluctuating during the reading of the pose, and must be measured in situ, which is the role of the serial register overscan strip, which represents a measurement of zero. The signal reading is

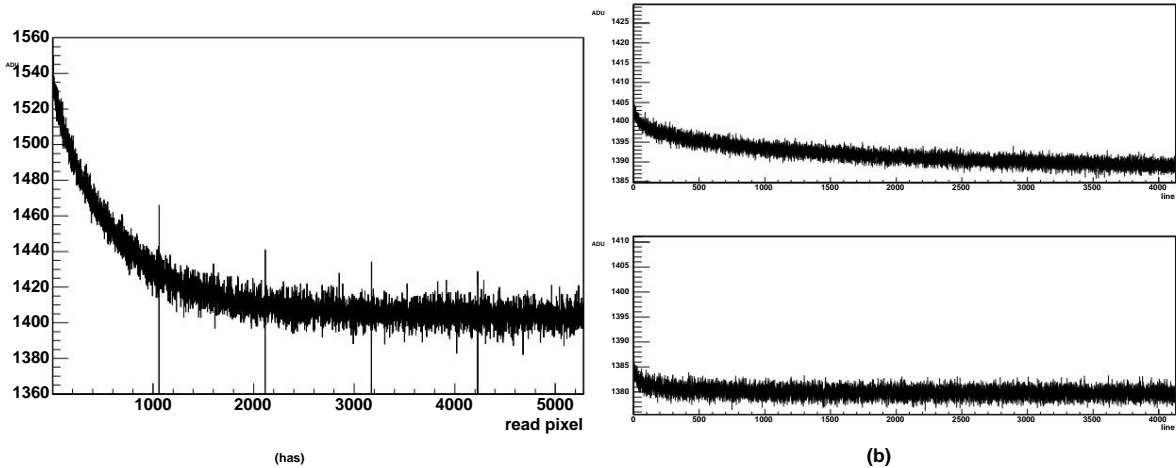


Fig. 3.4: (a) Value of individual pixels in ADU, as a function of the number of pixels read from the start of reading. (b) Average value of the pixels in the serial overscan area as a function of the number of the line read, showing the non-reproducibility from one pose to another.

## CHAPTER 3. USE AND IMPLEMENTATION OF CCDs FOR THE SPECTROGRAPHY

---

sequentially by each preamplifier, it is possible to reconstruct, from the spatial image, the time-ordered data, shown in figure 3.4 for a pose of type BIAS. Regular structures every 1024+32 pixels correspond to the register shift parallel, which induces a read signal at -600 ADU relative to the pedestal, followed by a few pixels of systematically higher value (see paragraph 3.3.6).

The use of the overscan band therefore makes it possible to determine the level of the pedestal after each line reading, and therefore to reconstruct level 0 by linear interpolation along the physical line. However, the first line does not have a measure of zero before its reading, and it is corrected by extrapolation of the slope calculated for line 2. The interpolation linear on the first lines of a concave signal results in a systematic bias. This will however be reduced by subtracting the mean bias, and moreover, the first line that we do not can correct with guaranteed accuracy does not contain any useful signal: the spectra are in effects projected in the middle of the CCD.

### 3.3.2 Noise and playback artifacts

In addition to the pedestal, the reading introduces noise that includes both a contribution random and a correlated contribution, as shown in Figure 3.5. The overscan area being a measurement of 0, it is also used to determine the average reading noise per measurement standard deviation statistics, however only considering the last 20 pixels of the overscan in order to avoid the effects of charge transfer inefficiency. The noise level is typically 3.0 e<sup>-</sup> for tracks B and R, 7th for the photometric CCD and 11th for the guiding CCD of the P channel.

A level differential is observed between the pixels of the even columns and the pixels of the odd columns, which we call the even-odd effect. The latter is constant along the reading of a pose, and is reconstructed once the pedestal is subtracted by calculating the difference of average level between adjacent columns. This effect, susceptible to secular drift, is far to be negligible and can reach 2 e<sup>-</sup> for channel B, and 0.7 e<sup>-</sup> for the R channel.

Crosstalk noise is observed at about 7 KHz, attributed to the switching power supply. Despite several shielding studies on the cable leading from the CCD to SDSU, we are not

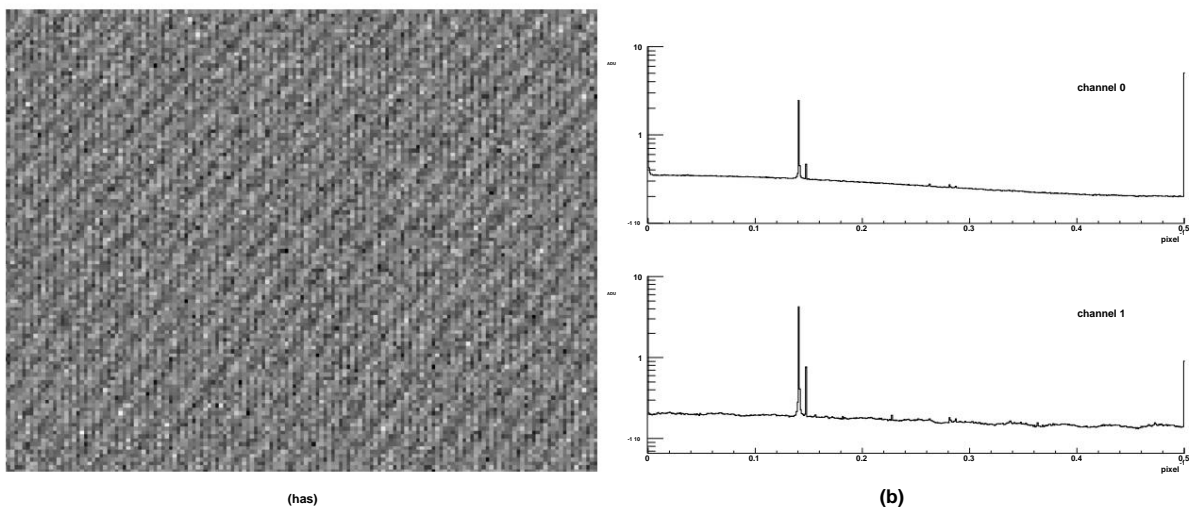


Fig. 3.5: (a) Subsection of a bias pose, showing typical read noise. (b) Spectrum of associated noise power for each of the preamplifiers.

### 3.3. INSTRUMENTAL SIGNATURES AND PREPROCESSING ALGORITHM

---

managed to eliminate it entirely. If the frequencies of this noise are relatively stable from one exposure to another, the phase shift observed from one line to another is not regular during reading.

This property leads us to attribute its origin as being exogenous to the clock system. A subtraction would therefore require line-by-line analysis of the phase, possibly with an adjustment by a spline-type function of this on all the lines. However, its spatial period being about 7 pixels, the overscan band only contains about 3 periods, and in the end the characteristics of this noise did not allow it to be subtracted satisfactorily, so it remains present on the processed poses. It is considered as read noise, and its amplitude is included in the numbers cited above.

The last read artifact studied is the bit skew on the ADCs: this is measured on a high-intensity uniform field pose, and is therefore only available on the data taken in Lyon on channel B1. If the ADCs were perfect, the least significant bits should be 0 or 1 with a probability of 50%. We measured a significant skew for 7 bits out of the 18 accessible by this method, but in all cases less than 0.2%, and we considered this phenomenon as negligible.

#### 3.3.3 Gain

The gain measurement was performed by replacing the optical window of the various cryostats with a light-opaque window containing a  $^{55}\text{Fe}$  source, whose X-rays deposit an average of  $1620 \text{ e}^{-}$  in the silicon. A reconstruction of energy deposit clusters therefore allows a precise determination of the gain for each amplifier, typically between 0.74 and 0.77  $\text{e}^{-} / \text{ADU}$  for the spectroscopy channels, and between 1.5 and 1.6  $\text{e}^{-} / \text{ADU}$  for the photometric channel.

However, this measurement cannot be performed once the CCD is mounted on the instrument, and the gain is likely to vary. Such variations can be suspected for the photometry and guiding CCD: indeed, flat-field exposures show a level difference between the preamplifiers after gain calibration. To verify the *in situ* gain values, three methods were used, all of which use a simple statistical property: the expected noise for an electron-calibrated pixel being Poisson noise plus readout noise, the inverse gain  $g$  (in  $\text{e}^{-} / \text{ADU}$ ) is given by

$$g = \frac{\text{NADU}}{\sqrt{2 \cdot \bar{y} \cdot \bar{y}}} \quad (3.1)$$

where NADU is the number of counts in logical units,  $\bar{y}$  the variance corresponding to the read ADU, the measured statistical variance and  $\bar{y}$  noise in ADU units. The difficulty in implementing 2 of these methods is the determination of  $\bar{y}$

ADU, which involves having a large number of statistical realizations of the same measurement, which is not difficult to put into practice. The methods used were as follows:

- The first method consists of studying the variance of the signal for each given pixel when they are illuminated under the same conditions by a constant flux light source. This can be done on **CONTINUOUS** or **DOME** type exposures, provided that the telescope is stationary while the sequence is being taken. The disadvantage of this method is ensuring the stability of the light sources used. The lamps typically take a few tens of minutes to stabilize in temperature, and furthermore they are not controlled by photodiodes, which affects the reproducibility of the measurements. An LED system

<sup>1</sup>Indeed, the presence of the spectrograph prevents the achievement of uniform illumination in the instrument

---

**CHAPTER 3. USE AND IMPLEMENTATION OF CCDs FOR SPECTROGRAPHY**


---

originally placed on the back of the secondary mirror to monitor this stability was struck by lightning, and was not replaced.

- The second method consists of using a single uniformly illuminated pose, and replacing temporal statistical studies on a pixel with spatial statistics. The sources of uncertainty in this case come from illumination inhomogeneities from one pixel to another, which amounts to adding an additional noise term. Moreover, in the spectroscopic channel, the illumination is far from uniform.
- A final method was then considered: in the spectrograph, the aim is to reconstruct the slow variations in illumination along a column, for example using a spline function adjustment, and to determine areas for which a linear interpolation is reasonable (defined as a difference between the spline function and an interpolated line less than 0.1  $\bar{y}$ ). The statistic retained is then the statistical difference observed at this linear interpolation. At the scale of a single exposure, this method is however limited by the available statistics.

These methods allowed us to validate the gain value to within 20%. Only a difference between the different P-channel amplifiers was observed. However, uncertainty in the gain value is negligible at first order in data analysis: indeed, one of the principles of calibration is to work on flux ratios: as long as the gain is stable, its value disappears in the end. On the other hand, an error in the gain will result in an error in the estimated variance. As with the final flux value, as long as the weights involved in the various averaging operations are all given within the same multiplicative factor, this will not change the calculated average values.

We estimated the variances of the extracted spectra at various stages of the data analysis chain by studying the bin-by-bin spectral fluctuations. To do this, we used the third of the methods mentioned above, but this time applied it to the extracted spectra at various stages of the reduction (see Figure 3.6). The value represented is

$$\frac{2\chi^2}{N} = \frac{1}{N} \sum_j \frac{(y_j - \bar{y})^2}{(\bar{y}_j^2)^{2+n}} \quad (3.2)$$

where  $y_j$  is the value of bin  $j$ ,  $\bar{y}_j$  its uncertainty, and  $y$  is  $\bar{y}$  represents a modeling obtained by the extrapolation from one bound to the other of an interval for which the function is reasonably linear. The increasing value for  $n > 5$  is interpreted as the increasing influence of the deviation from the model, while the sharp drop for  $n = 1$  is interpreted as a correlation between adjacent bins. The latter comes from the resampling operations during the extraction of the spectra to form the 3D cube, and since the variance stored in the files is the initial resampled variance (a choice that allows for a correct evaluation of the variance after broadband integration), the presence of a correlation between adjacent pixels induces a lower real variance than that stored.

By establishing a resampling model of the type

$$y_j = \bar{y}_j + (1 - \bar{y}_j)x_{j+1} \quad (3.3)$$

where the  $x_j$  are hypothetical independent measurements before resampling, with standard deviation ( $f\bar{y}_j$ ) we determine a correlation coefficient  $\bar{y}$  between nearest neighbors  $y_j$  and  $y_{j+1}$ , as well as a scale factor  $f$  by which the variances should be multiplied to account for the

### 3.3. INSTRUMENTAL SIGNATURES AND PREPROCESSING ALGORITHM

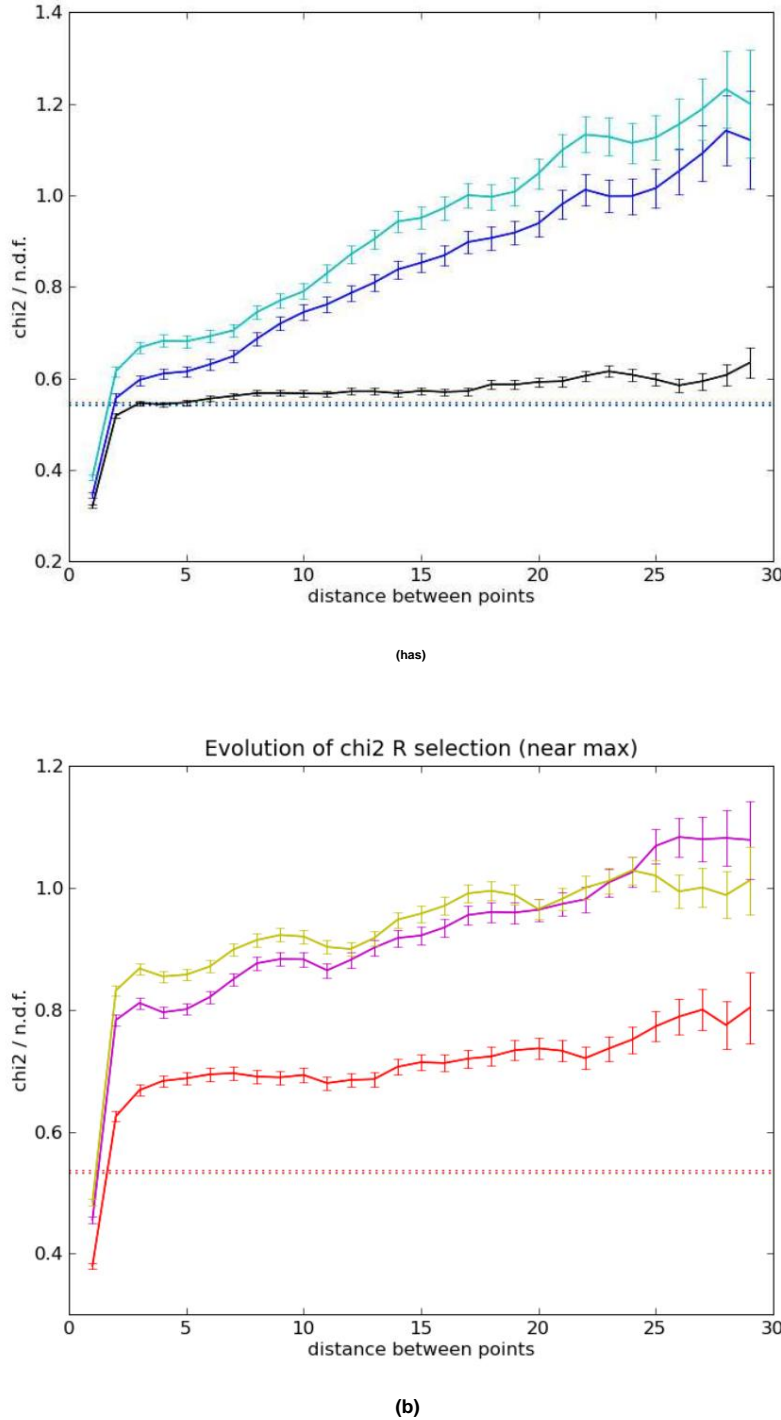


Fig. 3.6: Measure used to reconstruct the variance using the  $\hat{y}$  between two spectral bins as  $\chi^2$  depending on the distance defined by Equation 3.2, and thus expressed in units of  $\hat{y}$  degree of freedom, using the variance stored in the reconstructed pose for channel B (a). Black corresponds to the 3D cube spectra, blue to the extracted spectra, and cyan to the flux-calibrated spectra. The dotted horizontal lines correspond to the expected value for the measured autocorrelation coefficient. For channel R (b), red is for the 3D cube spectra, magenta is for the object spectra after extraction, and yellow is for the flux-calibrated spectra.

---

**CHAPTER 3. USE AND IMPLEMENTATION OF CCDs FOR SPECTROGRAPHY**


---

observations by:

$$\frac{2 \times 1}{N} = (1 + 3\bar{y} + 3\bar{y}^2)f^2 \quad (3.4)$$

$$\frac{\bar{y}^2}{N} = (1 + 2\bar{y} + 2\bar{y}^2)f^2 \quad (3.5)$$

which leads to

$$1\bar{y} = 1\bar{y} 2\bar{y} \frac{2\bar{y}}{N} \quad (3.6)$$

$$f^2 = \frac{\bar{y}^2}{N} (1 + 2\bar{y}) \quad (3.7)$$

The choice to take the 3rd nearest neighbor for the evaluation of  $f$  comes from a possible correlation between the  $y_i$  and the  $y_{i+2}$ , as suggested in the figure by the systematic inequality  $\bar{y}_2 < \bar{y}_3$ . The measurements give for the B channel  $\bar{y}_B = 0.48$  and  $f_B = 1.05$  and for the R channel  $\bar{y}_R = 0.48$  and  $f_R = 1.23$ : the correlation is almost the maximum correlation of 0.5 allowed by the model.

**As for the values of  $f = 1$ , it is difficult to say whether they come from a fluctuation of the gains after their measurement with the X, or whether it is an artifact related to the procedure of construction of the 3D cube. In any case, these numbers are consistent with the value of the gain validated at 20% by the other methods.**

These measurements were confirmed by studying the autocorrelation and pulls of the residuals to a spline fit on the measured spectra. This procedure is described in Nicolas Chotard's thesis (2011).

### 3.3.4 Cosmetic defects

Cosmetic defects are point defects that irrecoverably alter the signal, and the corresponding data must be masked from the preprocessed exposure.

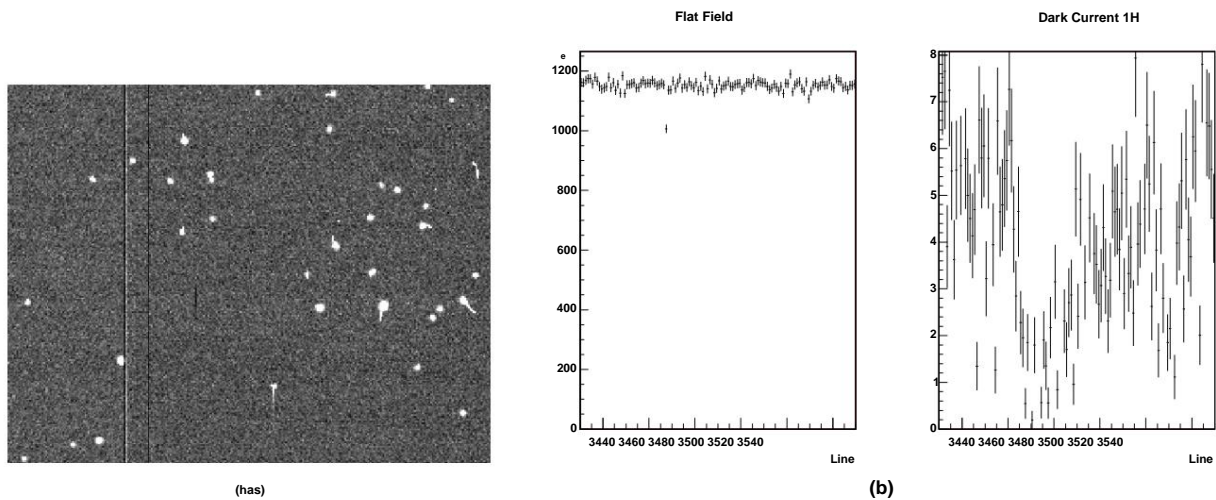


Fig. 3.7: (a) CCD defects of channel R, observed on a DARK exposure. The reading is done from the top of the exposure for this channel. (b) Pixel values along the same column of channel B (the reading is done from line 0), showing the effect of an electron trap on a uniformly illuminated exposure, on the left, and on a low-intensity exposure, on the right.

### 3.3. INSTRUMENTAL SIGNATURES AND PREPROCESSING ALGORITHM

---

Since the R-channel CCD is of a particular type, we had to accept it despite a relatively high defect rate. Figure 3.7 shows an overview of these. These defects are of several types. On the one hand, some junctions between pixels are faulty, which leads to a loss of signal. This data is immediately identified on the sensor by aberrant data.

This is the case of the double dark then light vertical line, as well as the simple dark vertical line observable in the above-mentioned figure.

More subtle are electron traps. These trap a certain number of electrons during the transfer, this number depending on the signal height, and then release them with a certain time constant. When the signal is high, such defects can go unnoticed, because the number of trapped electrons is lower than the Poisson noise. The usual methodology for detecting them is to correct a uniformly illuminated low-intensity pose with a uniformly illuminated high-intensity pose. We performed such exposures with the means at hand during the integration of the R CCDs and those of the P channel by using the quasi-Lambertian character of a sheet of paper illuminated by a desk lamp. These traps can also be detected on dark current exposures: Figure 3.7a contains two examples. The first is visible as a black line towards the middle of the exposure. The other is visible towards the middle of the bottom of the exposure: the electron trap is located out of field, but when a non-constant signal passes through it, as in the case of the cosmic, it will trap more electrons before releasing them following the readout.

Finally, a last case of defect is observed on the R channel: these are pixels for which the dark current is such that it saturates not only the pixel, but also those with which it is chained in the parallel register. In addition, when reading the serial register, the presence of a highly saturated pixel results in a fluctuation of the 0 level for about a hundred read pixels. The effect of this defect is shown in Figure 3.8. While it is easy to mask saturated pixels, and inevitable to mask the entire corresponding line, the presence of saturation results in a fluctuation of the level for the pixels read after a saturated pixel in the serial register. The number of affected pixels is dynamically evaluated based on the number of saturated pixels. Finally, as a curiosity, it is possible to model the decay along the saturated column after saturation, by a model of type

$$x_j = p_0 + j \cdot p_2 \quad \frac{p_1}{\text{where } x_j \text{ is}} \quad (3.8)$$

the height of the signal read on line  $j$  and  $p_{0,1,2}$  are the parameters to be adjusted. Such a modeling is not self-evident: one might expect an exponential decay if it were simple electrons trapped in wells of identical depths. The presence of a term in inverse time suggests, on the contrary, a continuum of well depths. Indeed, if an individual well releases the electrons according to a time law in

$$\ddot{\text{y}} \cdot t \cdot e^{-t} \quad (3.9)$$

Integration over all wells will give a law in

$$\int_0^y e^{-t} dt = 1 - e^{-y} \quad (3.10)$$

However, even if we were able to establish an empirical law on the pixels along this line, a correction would depend on the subtraction of a physical signal that we are also trying to determine. Since the absence of a column is harmful, but not crucial for the extraction, we preferred to mask these two so-called hot columns.

In total, no columns on track B, 7 columns on track R and 4 on track P are affected of defects.

## **CHAPTER 3. USE AND IMPLEMENTATION OF CCDs FOR THE SPECTROGRAPHY**

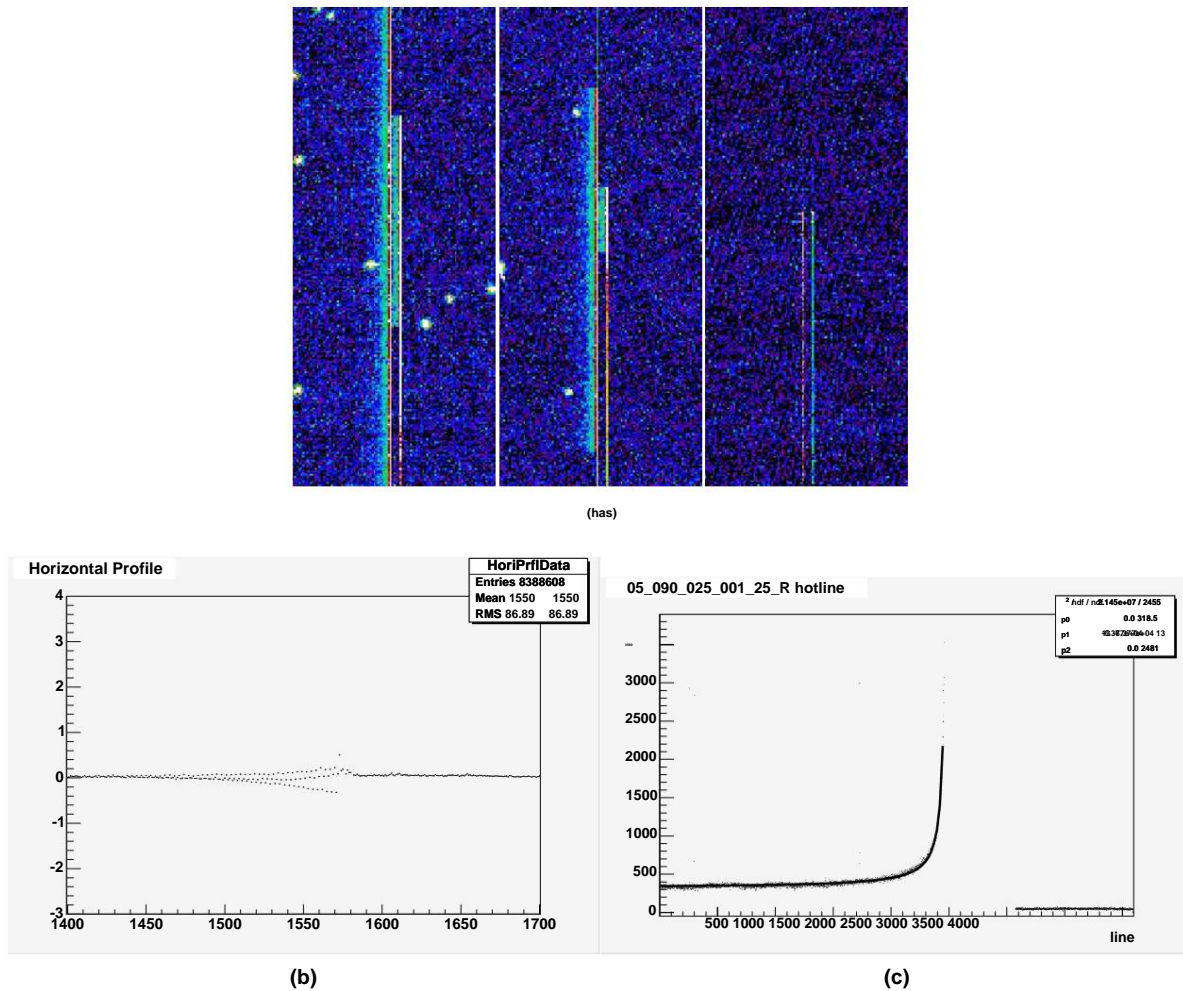


Fig. 3.8: (a) Effect of high dark current pixels, called hot pixels, on the R channel CCD, for 3600, 1000 and 0 seconds of nominal exposure time. This CCD is read from the top, the preamplifier being on the right. (b) Value of the pixels on the serial register, averaged over the rows on which a saturation is observed, which gives the variation of level 0 following saturation. (c) Value of the pixels along the hottest column, and its adjustment by a  $1/x$  model.

### 3.3.5 Charge transfer efficiency

When shifting registers, there is a non-zero probability that the charges remain in their original potential well. In order to quantify this phenomenon, we used poses uniformly illuminated during the tests in Lyon, and measured the signal in the serial overscan regions and parallel (see figure 3.9). Contrary to what is written in most books, the delayed signal observed in the serial overscan does not correspond to a delayed charge, as proven by the variance which does not depend on the signal height: it is a relaxation effect of the reading electronics after measuring an intense signal for 1024 pixels. We concluded that to obtain a clean area on the serial overscan, it was necessary to eliminate data analysis of the first 10 readings. On the other hand, the observed level, which is compatible with the specifications of CCDs in terms of charge transfer efficiency, corresponds to a negligible distortion of the transverse spectral PSF.

Regarding parallel registers, the observation of a Poisson-type variance on

### 3.3. INSTRUMENTAL SIGNATURES AND PREPROCESSING ALGORITHM

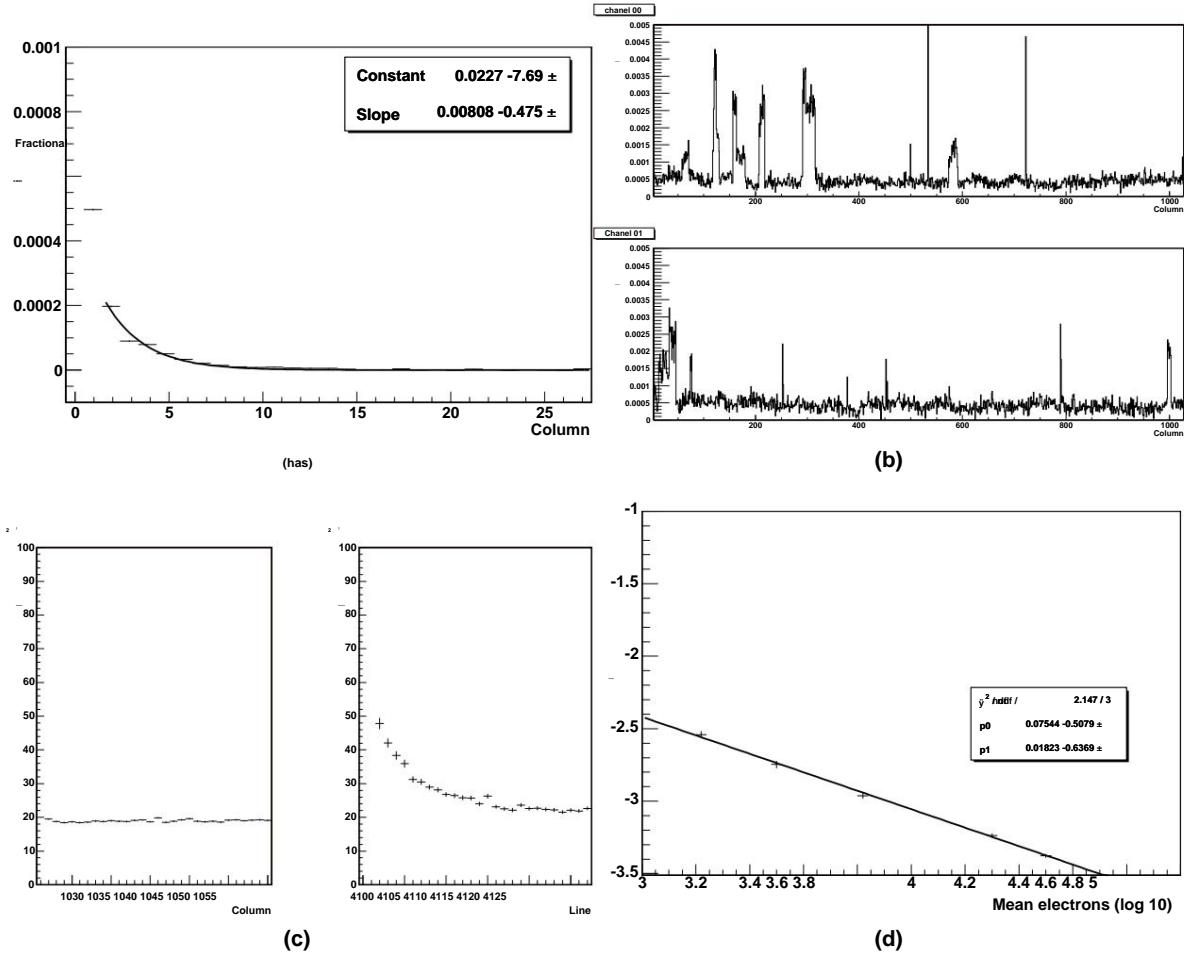


Fig. 3.9: **(a)** Delayed charge fraction for serial overscan, as a function of column number of the overscan, for a uniformly illuminated pose at  $33 \times 103$  e  $\ddot{\text{e}}/\text{pixel}$ . **(b)** Total fraction of delayed charges measured in the parallel overscan area, as a function of column number for both amplifiers, for the same illumination, showing a large heterogeneity according to the columns. **(c)** Variance measured on the pixels of the two overscan zones, series on the panel from left, parallel on the right panel. **(d)** Delayed charge fraction for registers parallels as a function of the illumination level, showing a power law dependence.

## CHAPTER 3. USE AND IMPLEMENTATION OF CCDs FOR SPECTROGRAPHY

---

repeated exposures shows that it is indeed delayed charges that are observed. On the other hand, the works do not mention the dependence with the amplitude of the illumination of the fraction of delayed charges according to a power law. In the end, the measurement that we carried out, at the end of a signal of 104 e<sup>-</sup>, is well within the specifications of and a worst of 10 e constitutes only a negligible deformation of the PSF compared to its natural spread (see the thesis of Nathalie [Blanc, 2006](#)).

### 3.3.6 Bias

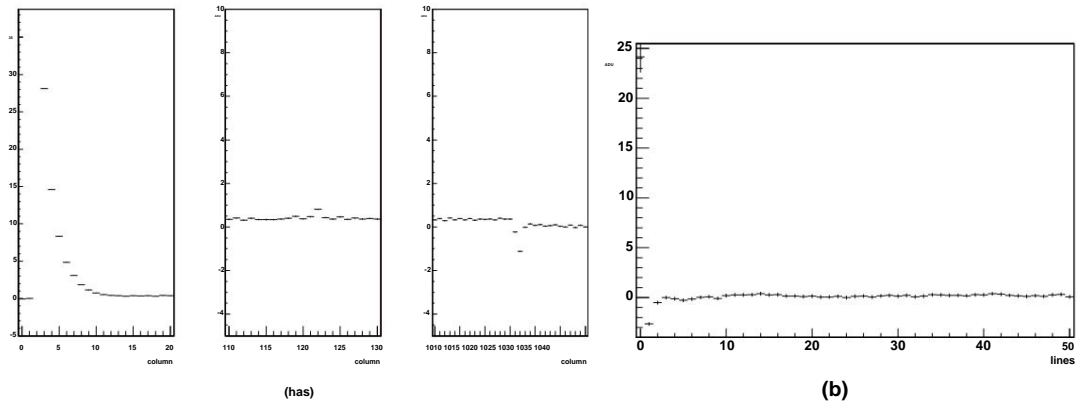


Fig. 3.10: (a) Average bias observed along the serial register for three given intervals, at the beginning, middle, and end of the reading. (b) Average bias observed along the parallel register, at the beginning of the reading.

**BIAS** exposures allow us to subtract systematic biases related to the readout electronics for an exposure nominally exposed for 0 seconds. However, even if the exposure time is negligible, the readout takes a finite time, approximately 80 seconds. The pixels will therefore integrate dark current during this time, which will lead to a higher signal at the end of the readout. The intensity of the bias exposures can therefore be described as

$$I(i,j) = B(i,j) + \sum_{i=0}^j D(i,j) \Delta t \quad (3.11)$$

where  $B$  is an electronic term corresponding to a theoretical map of 0 input electrons, and  $D$  is the dark current, integrated over the per-pixel transit time of  $\Delta t \approx 0.02\text{s}$ .

The analysis of the structures of a bias pose is therefore broken down into two phenomena, and we will discuss the influence of the dark current later.

Figure 3.10 shows the effects of the bias itself. In the serial register, at the beginning of the reading, the recorded level is systematically higher than the average and decreases rapidly.

We verified using the observed variance that this does not correspond to real charges, but to a relaxation phenomenon of the readout electronics subsequent to the offset of the parallel registers, and of a time constant comparable to what was observed in the serial overscan for uniformly illuminated exposures. The middle panel of the figure shows in column 122 the effect of a hot pixel of the CCD, which increases the observed level. Finally, the last physical pixel of the serial register, the first pixel of the overscan and the level of the rest of the overscan.

<sup>2</sup>Here we have neglected the integrated dark current during the 80 ms it takes for the sensor to reset before reading.

### 3.3. INSTRUMENTAL SIGNATURES AND PREPROCESSING ALGORITHM

---

are different: this difference comes on the one hand from electronic biases during the transition to overscan, and on the other hand from the dark current integrated into the physical zone, and of course absent from the overscan zone. Finally, the levels along the parallel register essentially show the gap between the linear interpolation, carried out on the pedestal value at the start of reading, and reality.

#### 3.3.7 Dark Current

The dark current of CCDs depends on the one hand on the temperature, according to the laws of quantum mechanics and thermodynamics, and on the other hand on the time after switching on the detector: charges are then trapped, and we observe a transient detrapping phenomenon whose characteristic quantity after several modeling tests is the time after switching on. The observation of this phenomenon led to a review of the data collection methodology in 2006, leaving the CCDs switched on as long as possible and reading them regularly, whereas previously we switched off the instrument between two nights of data collection.

The modeling of the average dark current observed on the pose is thus the following:

$$D(t, T) = I_0 + I_1 t^{-\gamma} + I_2 T^{3/2} \exp(-\frac{E}{2kT}) \quad (3.12)$$

where  $D(t)$  is the instantaneous dark current, which should be integrated over the exposure time, a constant term coming from a non-zero current observed at very low temperature, a second term representing the detrapping where  $t$  is the time since power-up, and a thermodynamic term where  $T$  is the temperature (in K),  $k_B$  the Boltzmann constant and  $E$  the gap energy in silicon,

$$E = 1.11557 \times 7.021 \times 10^{-4} \frac{T^2}{1108 + T} \text{ eV} \quad (3.13)$$

The adjustment of the free parameters  $I_0, I_1, I_2$  and  $\gamma$  must be done on bias-corrected poses, and the integrated dark current on the latter must be taken into account when reading it. We then use the same modeling for the dark current in the bias pose, but taking another set of adjusted values  $I_1$ . This choice is justified by the integration during an average effective exposure time of 40 seconds, but whose characteristics differ from a DARK exposure : the first pixel is in fact exposed for 0 seconds and the last for 80. The adjustment was carried out on the average observed values of the signal per read amplifier for 13,000 BIAS exposures and 3,000 DARK exposures of 3,600 seconds acquired between 2005 and 2008, thus covering all the operational parameters  $(t, T)$  of SNIFS.

Figure 3.11 shows the comparison between the measured level on dark exposures for various integration times, compared to the modeling. The adjusted parameters are similar to within 5% on the two amplifiers of the same CCD. The time decay coefficient,  $\gamma$ , is approximately  $\gamma \approx 1.3$  for channel B and  $\gamma \approx 1.1$  for channel R, and is therefore close to  $\gamma \approx 1$ , which is similar to the detrapping modeling proposed during the considerations on CCD defects. The level of dark current observed at the nominal operating temperature, i.e.  $-120^\circ\text{C}$ , and after stabilization is approximately  $1.5 \text{ e}^{-}/\text{H}$ . It takes more than ten hours to consider that the transient phenomena become negligible.

The model predicts only an average dark current for CCD exposures. To account for pixel-to-pixel differences, we map the residual biases to the model

## CHAPTER 3. USE AND IMPLEMENTATION OF CCDs FOR SPECTROGRAPHY

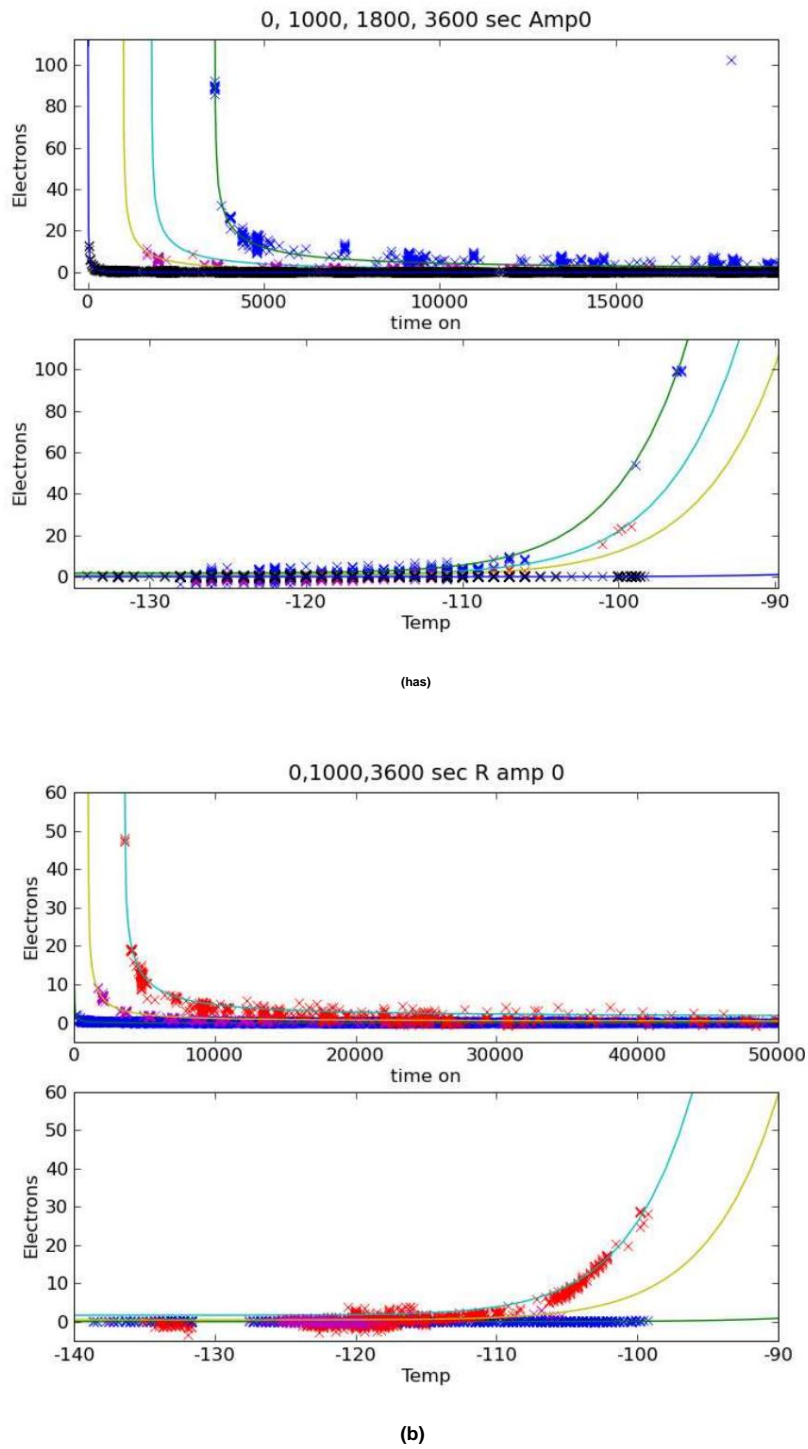


**Fig. 3.11: Comparison of the levels measured at BIAS and DARK exposures with the established model for the dark current. From top to bottom, the data from the left amplifier of channel B (a), for exposures from 0 to 3600 seconds, as a function of the ignition time, then as a function of the temperature (in  $^{\circ}\text{C}$ ) with the same color code; at the bottom, the data from the left amplifier of channel R (b), as a function of the ignition time and then of the temperature.**

---

 3.3. INSTRUMENTAL SIGNATURES AND PREPROCESSING ALGORITHM
 

---

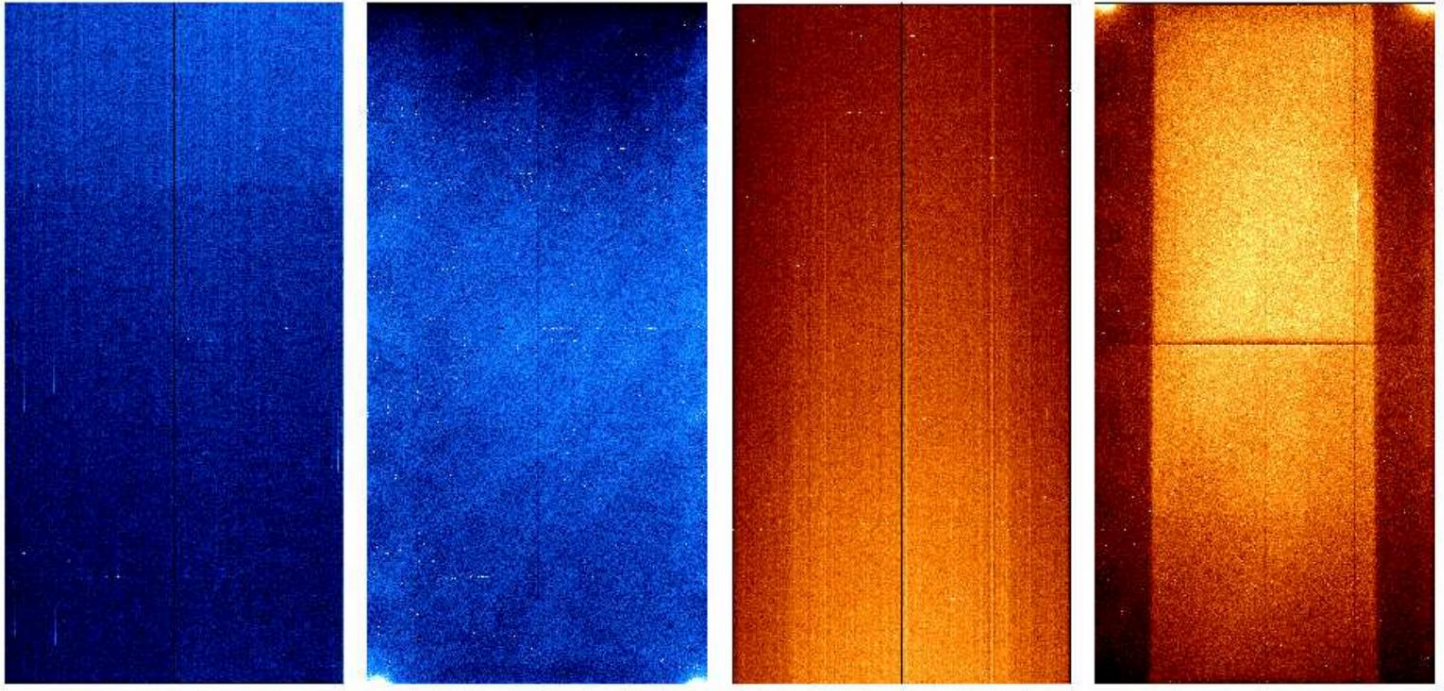


Fig. 3.12: Map of pixel-by-pixel variations, from left to right, of the bias then the dark current of channel B, of the bias then the dark current of channel R. Dark colors correspond to a weaker flux than lighter colors.

average, which we subtract. For the DARK exposures, we also calculated the residuals, but normalized to the exposure time. Thus, the final subtraction performed is of the type

$$S(T,t,i,j) = B(T,t) + b(i,j) + D(T,t,texp) + d(i,j) \times texp \quad (3.14)$$

where  $B$  is the bias-related model,  $D$  the dark current model integrated over the exposure time  $texp$ , and  $b(i,j), d(i,j)$  are residual maps. These are shown in Figure 3.12. The BIAS residuals exhibit vertical structures, characteristic of the integration of the current from the hot pixels. On the R channel, two darker bands can be seen on the sides, corresponding to the integration of a weaker dark current in these areas. The level is higher at the end of the readout, i.e. at the top for B exposures, and at the bottom for R exposures, due to the longer integration of the dark current. In the center, we can see the bias effect on the last physical pixel of the serial register read by the preamplifiers as described above.

The DARK residues show, in addition to hot pixels or dead columns, an underlying structure that comes from the CCD manufacturing process: on the blue CCD we see large oblique structures from the thinning process, while on the red CCD we see, in addition to two dark bands of unexplained origin, a central dark area from a masking effect during etching. Finally, at the bottom of the B card, and at the top of the R card, we can see hotter spots corresponding to the physical position of the preamplifiers that heat the CCD, a phenomenon called glow in English.

The subtraction of the dark current, however, leaves two artifacts. On the one hand, at high temperature or short time after ignition, the residues of the vertical bands observed in the R channel are visible on the extracted spectra. The model will therefore have to be improved, probably by

## CHAPTER 3. USE AND IMPLEMENTATION OF CCDs FOR SPECTROGRAPHY

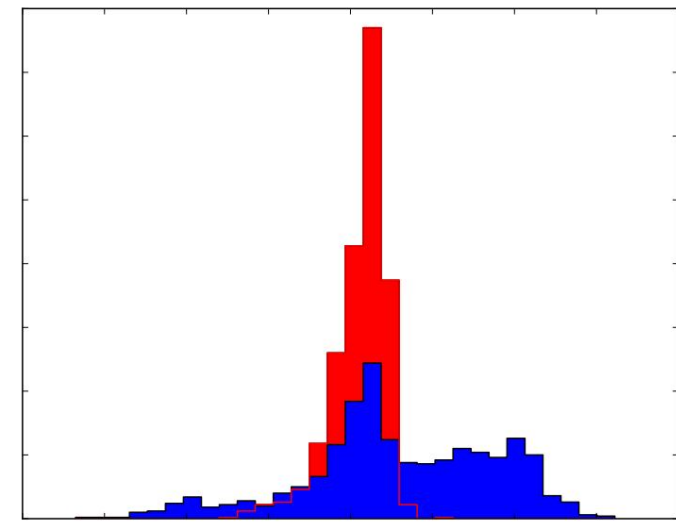


Fig. 3.13: Histogram of the dark current differences in  $e^-/\text{H}$  between the two CCD amplifiers, in blue for channel B, in red for channel R.

replacing the term in  $d(i,j) \times t_{\text{exp}}$  by a term of type  $d(i,j) \times D(T,t,t_{\text{exp}})$  in a first step, or even an expansion in the form of several spatial maps in  $(i,j)$  whose amplitude will be determined by the elements of the model.

The other residual is a random fluctuation of the dark current on the right amplifier of the blue CCD, as seen in Figure 3.13. We have determined that its amplitude is linear with exposure time, and that it is not a random fluctuation of the zero level. This effect, which can reach 0.4  $e^-/\text{H}$ , will be difficult to correct: if it is possible to measure in situ a level differential on the two amplifiers to within 0.03  $e^-/\text{H}$  electron in low light conditions, this does not indicate which amplifier is at fault, and furthermore it will be difficult to determine an unlit area as soon as the signal is too large, making the correction hazardous. However, we will see later that we have reason to suspect that the problem comes from the right amplifier,

### 3.3.8 Uniformity

An important step in data processing, once the zero level corresponding to an absence of incident photons has been determined, is to take into account the relative spatial and spectral efficiency of converting incident photons into electrons. The procedure for the photometric channel should have been the canonical use of a uniformly illuminated exposure (or flat field). However, spurious reflections on the multi-filter posts as well as light leaks between filters made this technique ineffective, and Rui Pereira (2008) had to use a PCA-based technique to eliminate high-frequency structures from the flat field that varied from one exposure to another. We reproduce in Figure 3.14 the appearance of the flat poses taken under various conditions. The three red parts of the multi-filter (shown in Figure 2.5) are affected by interference fringes, linked to a photon absorption length that is not negligible compared to the thickness of the CCD, and by characteristics dependent on the wavelength, the part corresponding to the

### 3.3. INSTRUMENTAL SIGNATURES AND PREPROCESSING ALGORITHM

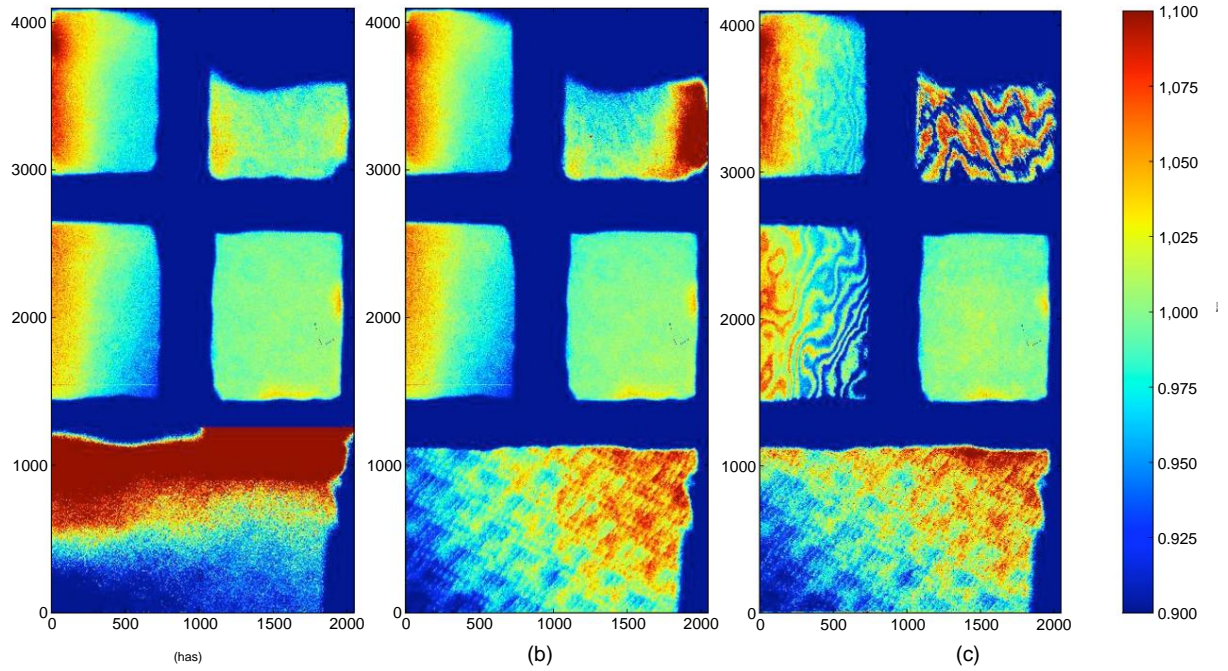


Fig. 3.14: Flat field exposures of the photometric CCD, taken with Dome (a) Sky (b) or Super-flat (c). (Thesis R. Pereira)

filter V (middle right) shows no coherent spatial structure, while filter U shows structures related to the CCD manufacturing process, the mean free path of the photons being sufficiently weak so that the efficiency is sensitive to the thickness crossed before to reach the active area of the CCD.

Since the flat-field structure is very wavelength dependent, it is not possible to use the poses obtained in uniform illumination to carry out a correction in the channels of spectroscopy. Indeed, the intensity received on the pixel  $(i,j)$  is modeled by

$$NCCD(i,j) = \frac{I(I,\bar{\lambda})PSFI,\bar{\lambda}(i - i_0, j - j_0)\bar{\gamma}(i,j,\bar{\lambda})}{I,\bar{\lambda}} \quad (3.15)$$

where  $\bar{\gamma}(x,y,\bar{\lambda})$  is the efficiency factor we would like to correct,  $I$  the intensity received by the microlens  $I$  at wavelength  $\bar{\lambda}$ , giving on the CCD a response function image PSF whose centroid  $i_0, j_0$  also depends on  $I$  and  $\bar{\lambda}$ . To perform this type of correction not only have a set of monochromatic efficiency maps, but also have perfect confidence in the PSF model. However, since the centroids  $x_0, y_0$  are almost always centered at the same location on the CCD which ensures that the length wave striking a given pixel varies only within a restricted range, our modeling can approach by

$$NCCD(i,j) = \frac{I(I,\bar{\lambda})PSFI,\bar{\lambda}(x - x_0, y - y_0)\bar{\gamma}(I,\bar{\lambda})\bar{\gamma}(i,j)}{I,\bar{\lambda}} \quad (3.16)$$

the correction thus uses a factorization in two terms, one depending on optical absorption and the average absorption on the CCD,  $\bar{\gamma}(I,\bar{\lambda})$ , which is determined using poses of type CONTINUOUS up to a spectral multiplicative factor or spectral flat, the other,  $\bar{\gamma}(i,j)$ , which represents

## CHAPTER 3. USE AND IMPLEMENTATION OF CCDs FOR SPECTROGRAPHY

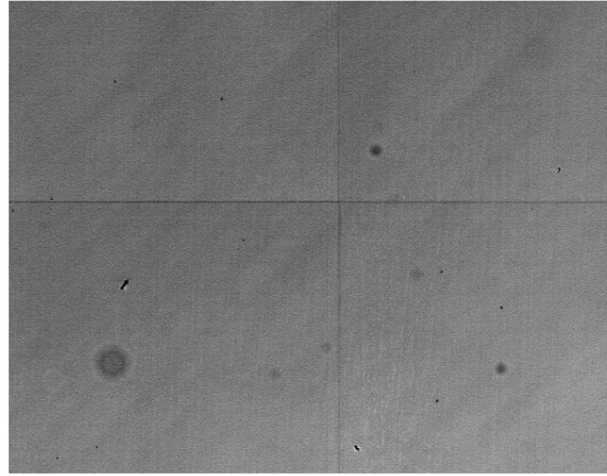


**Fig. 3.15:** Extract from a flat field of CCD B, taken with a V filter in the laboratory, showing the junction effects between the etching masks of the CCD as dark lines. The dark spots correspond to dust, and the large slanted structures come from the sensor thinning process.

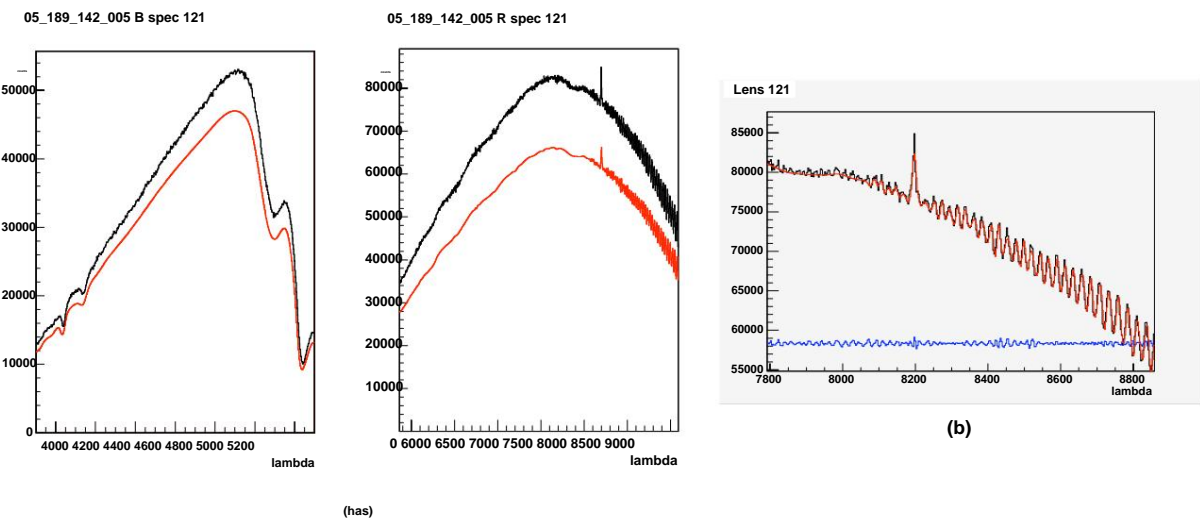


**Fig. 3.16:** (a) Extracted spectrum from a CONTINUOUS exposure (in black), on the left for channel B, on the right for channel R. The black curve corresponds to the extracted data, the red curve to the spline smoothing used for correction. The intermediate frequency structures on channel B are related to the bandwidth of the dichroic plate; while the red channel shows on the one hand a singular peak related to a CCD effect, and on the other hand interference fringes in the red. (b) Zoom on the reddest part of the spectrum. In blue, the residue observed after correction

### 3.3. INSTRUMENTAL SIGNATURES AND PREPROCESSING ALGORITHM

---

a corrective factor to the first to take into account high spatial frequency variations, mainly linked to point geometric defects in pixel size.

This factor was measured in the laboratory in Lyon on channel B. The amplitude of the pixel-to-pixel efficiency variations is 0.7%, and it can be neglected: this effect will be averaged during spectral extraction, and then negligible compared to the fluctuations of  $\hat{y}(i,j)$ . However, as shown in Figure 3.15, engraving inaccuracies related to the finite size of the masks lead to edge effects for certain rows of pixels. These effects being physically linked to the CCD, they will not move according to the flexions, and must therefore be corrected: their amplitude can reach up to 13% as visible on the spectrum extracted from the red channel, in the form of a singular peak.

Observation of the extracted spectra (see Figure 3.16) shows that the red part of the spectra is affected by interference fringes, whose amplitude can reach 5% of the signal level at 9000  $\text{\AA}$ . These fringes are however at relatively low frequency, the inter-fringe distance being 25  $\text{\AA}$ , and are linked to the wavelength arriving at the CCD: their correction will be done naturally by the spectral flattening procedure, and the residuals are less than 1%. In addition, at the time of spectra extraction, the fringe residuals will be averaged, and the effect is not observable on our final spectra. The effect of telescope flexions on the flat-field after spectral extraction shows that residual intensity variations of up to 3% can however be observed at a traversed air mass of 2, the effect being more marked in the R channel due to a higher displacement of the centroids on the CCD.

#### 3.3.9 Remanence

Re manence is the phenomenon by which part of the signal from one exposure can be observed in the next exposure, particularly in the case of saturation when the electrons have sufficiently filled their potential well to find themselves trapped in wells that will only release them after a characteristic time, which increases as the temperature decreases. We limited this phenomenon by working at -120°C, which is a good compromise between the level of dark current and the risk of remanence. While this afterglow effect is sometimes visible on some exposures, we sought to quantify it by overexposing the spectrograph CCDs: a repeated CONTINUOUS exposure sequence producing a 300 ke  $\text{\AA}$  signal does not cause any observable afterglow on a 30-minute DARK exposure taken immediately afterward, which corresponds to ten times the nominal exposure expected for the brightest signal we use. At  $3 \times 10^6 \text{ e } \text{\AA}$ , we obtain an afterglow signal whose decay time is similar to that of the dark current after ignition, i.e. several hours before reaching a stable level. This level is however never reached during normal operation, and the phenomenon can be ignored in the spectrograph.

#### 3.3.10 Cosmic

Integrating the signal over long periods of time results in the presence of localized energy deposits, generally considered cosmic rays passing through the detector, but which may also be the result of radioactive decay in the cryostat. These localized deposits, which can reach saturation amplitude, must be eliminated. Several methods are used to do this.

- When you have poses taken under identical conditions, as is the case for BIAS or DARK poses , it is possible to stack the poses by applying either a median filter or sigma-clipping to the original poses. This method is the most robust.

### CHAPTER 3. USE AND IMPLEMENTATION OF CCDs FOR SPECTROGRAPHY

---

- On a single given exposure, it is possible to determine the position of cosmics using a Laplacian filter that will detect isolated peaks. However, it is necessary to distinguish between cosmics and fine spectral lines. While putting a cutoff to make the separation is trivial in channel B, the presence of scattering linked to the thickness of the CCD in the red channel leads — in order to keep the entire signal — to a low detection efficiency.
- The detection of cosmics used in production for science poses is done after extraction of the 3D cube. Indeed, a cosmic will be seen as an artifact localized spatially and in wavelength.
- However, it happens that fortuitous coincidences on the CCD result in pairs of cosmics not being eliminated on the cubes, which results in artifacts in the extracted spectra. A new algorithm is being developed, which consists of detecting at the time of spectra extraction a deformation of the transverse profile G (defined in paragraph 2.5.2) linked to the presence of cosmics, and eliminating it on a criterion of type  $\hat{y}$ <sup>2</sup>.

We used cosmics to determine the impulse response of CCD amplifiers. Indeed, apart from the hot zones of the CCD which correspond to localized defects, the number of which is not sufficient to perform statistical averages, cosmics are present in abundance in our data. The average profile observed (see Figure 3.17) for channel B shows a level systematically lower than the average level about 3 pixels after the signal maximum. This effect, with an amplitude at worst of 1% of the incident signal, will have no observable consequences, especially since the extraction only takes into account the 5 most illuminated pixels. On the R channel, we see that the average profile of cosmics is broadened due to diffusion. Compared to the maximum intensity, the profile shows an asymmetry as if we had delayed charges up to 2% of the peak height, whether it is an effect of charge transfer inefficiency, or of electronic response, hypotheses that we could only resolve by having controlled poses in the laboratory. This effect will however disappear from the analysis chain as long as it is independent of the signal height: in fact, as long as the distortion affects in the same way the science poses and the poses on which the transverse spectral PSF is determined, it will be correctly included in the modeling of the latter.

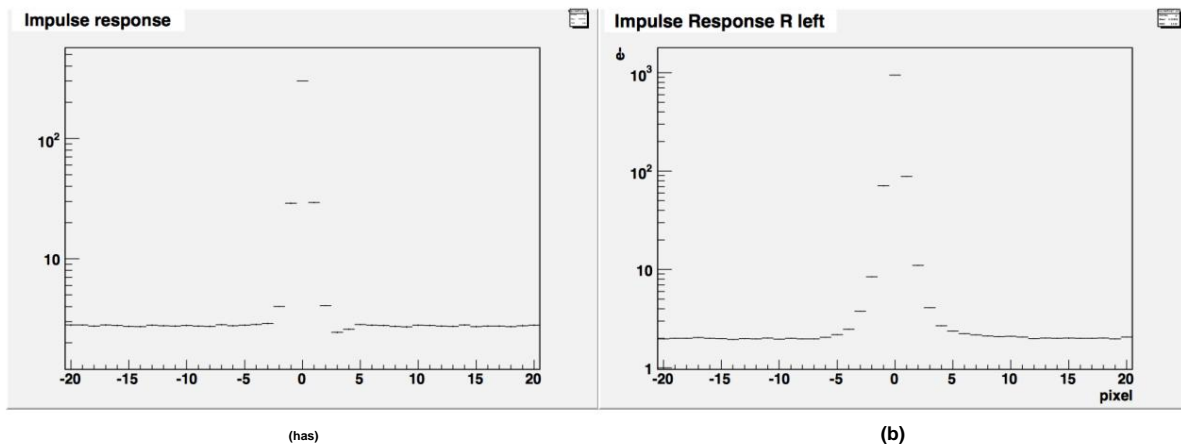


Fig. 3.17: Average profile on the serial register of the recorded cosmics as visible in channels B (a) and R (b), each time for the left amplifier of the CCDs: the pixels are numbered in reading order, centering on the cosmic.

### 3.3. INSTRUMENTAL SIGNATURES AND PREPROCESSING ALGORITHM

#### 3.3.11 (Non)-Linearity

We discussed in Chapter 2 the non-linearity measured at the end of the analysis chain on WD1413+257. However, CCD sensors are known to be very linear, which we confirmed by comparing DOME exposures between 1 second and 400 seconds: indeed, at the CCD level, an exposure of 400 seconds gives a level that goes from 0 to 70% of the logical saturation for channel B, and which saturates channel R, which makes it possible to scan the entire dynamic range and to check the linearity by making exposure reports.

If we have not detected any nonlinearity on channel R by this procedure, Figure 3.18 shows the result for channel B. At the CCD, the left amplifier behaves linearly, but the right amplifier produces a negative signal at low intensity in the inter-spectrum, whose amplitude seems at first sight to be of the order of 4% of the peak value. Figure 3.18b allows us to observe the effect of this negative signal on the extracted signal, visible in the form of a jump in intensity between the lower half and the upper half of the spatial image of the reconstructed cube, corresponding respectively to the spectra projected on the left and right parts of the CCD.

We have mentioned above the impulse response of the amplifiers reconstructed using cosmics. This response is identical whether it is the amplifier on the right, and moreover,

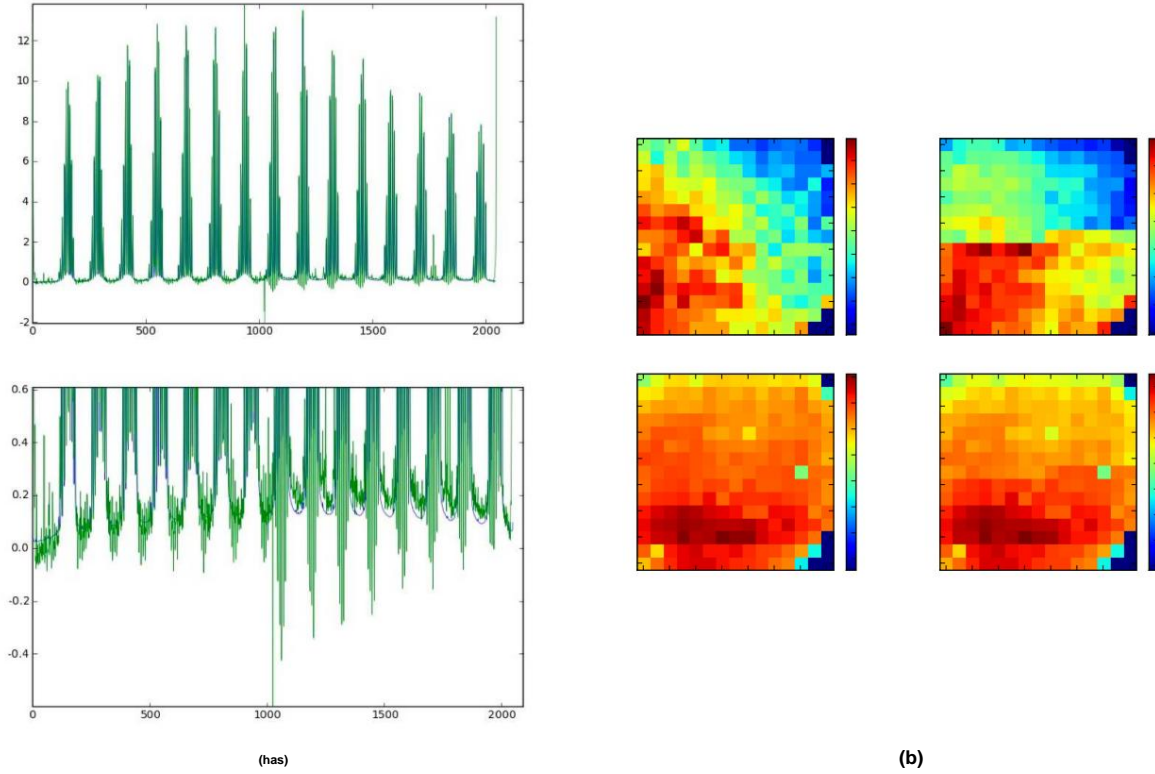


Fig. 3.18: (a) Averaged value over 1000 lines of the signal from the observed DOME exposures , normalized by the exposure time, on the blue CCD, in blue for long exposures, in green for short exposures. (b) Effect on the reconstructed cube, below before, above after flat-fielding operation. The signal has been normalized to the exposure time and integrated in wavelength. In the absence of non-linearities, the figures on the left exposed to 300 s and those on the right exposed to 1

---

**CHAPTER 3. USE AND IMPLEMENTATION OF CCDs FOR THE SPECTROGRAPHY**


---

the amplitude of the observed negative level is quite insufficient to account for a phenomenon height of 4%. The modeling cannot therefore be done in the form of a simple convolution of the incident signal with a response function. In addition, the analysis of negative delayed signals on the CCD shows that the envelope of their amplitude in a group of spectra is delayed by report to the envelope of the incident signal: a modeling of this phenomenon should therefore hold account of the history on several spectra of the incident signal. To date, no modeling satisfactory could not be carried out at the CCD level.

We studied the empirical behavior at the level of the extracted cubes on the poses of DOME, using the ratio of the observed fluxes between exposures of 1 and 300 seconds (see Figure 3.19. The data obtained can be modeled by

$$I = A I_{T_h}^2 + B I_{T_h} + C \quad (3.17)$$

where  $I$  is the observed intensity (normalized to the exposure time),  $I_{T_h}$  the expected intensity deduced from the long exposure,  $C$  represents a possible zero level shift,  $B$  a proportionality coefficient and  $A I_{T_h}^2$  a nonlinearity term chosen to reproduce the observed nonlinearity. The values observed are given in Table 3.1. It can be seen that short exposures suffer from a systematic shift from their level 0. This was at the time of this study approximately 0.9 e<sup>-</sup> at the level of the extracted spectra and still visible on the parameter  $C$  despite an ad hoc correction.

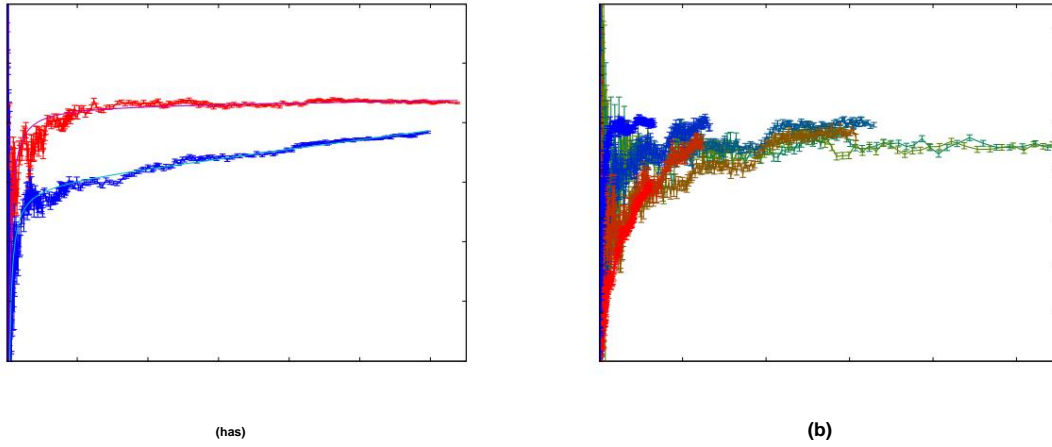


Fig. 3.19: (a) Ratio of observed to expected fluxes as a function of expected flux using the entirety of the spectra of the extracted cubes, for a reference of 300 seconds of exposure time, and a signal at 1 second. In red, the data for the left amplifier, in blue, for the one on the right. The solid lines correspond to a fitted model. (b) The raw data for various exposure time ratios.

Tab. 3.1: Expected and observed values for the nonlinearity parameters.

Expected Parameter	Amp. G	Amp. D	
A (1/e <sup>-</sup> )	0	0	$3.8 \times 10^{-4}$
B 0.9487	1	1.015	
C (e <sup>-</sup> ) -0.11	0	-0.12	

### 3.3. INSTRUMENTAL SIGNATURES AND PREPROCESSING ALGORITHM

---

Since then, the revision of the diffuse background subtraction algorithm has reduced the offset to between 0.1 and 0.6 e  $\ddot{\text{e}}$ . The proportionality coefficient, even for the so-called linear amplifier, is also not 1: this illustrates the difficulty of establishing perfectly controlled conditions. Indeed, either the exposure time is underestimated by 17 ms on short exposures, or the light intensity has varied by 1.5% on average between long and short exposures, which cannot be excluded. On the other hand, the non-linearity term is only significantly non-zero for the right-hand amplifier: under these well-controlled conditions, we therefore manage to properly model the non-linearity effect.

However, one should be careful not to claim victory: on the one hand, the chosen model cannot be extrapolated beyond an expected signal of 170 e  $\ddot{\text{e}}$ , and on the other hand, the panel in Figure 3.19b shows that the data cannot be immediately transposed to other time ratios between long and short exposures. However, these data at other exposure time ratios are statistically less abundant, and moreover, their quality is affected by variations in the bandwidth of the dichroic plate, without the **CONTINUOUS** data necessary for this correction having been acquired.

Ultimately, we have a model that allows us to determine by Monte Carlo whether the magnitude of the observed effect induces significant biases at the end of the analysis. In order to then proceed with a correction, we must prove that the chosen modeling allows us to improve the **scientific poses**, even if it is imperfect. This study remains to be done, and possibly the acquisition of **additional data will be necessary**.

## Contributions

I participated in the acceptance tests of the CCD of channel B in Lyon, in 2003, with A. Castera from the instrumentation department. The expertise acquired by this department was then concretized by tests on infrared sensors within the framework of SNAP, under the responsibility of G. S. As an expert on CCDs, I participated in the monitoring of these detectors upon return to the manufacturer, in the acceptance tests after correction in Honolulu, with G. Aldering, then in their installation on the instrument during integration in Hilo and then at the summit of Mauna Kea. I was also responsible for and developed the preprocessing code that corrects most of the phenomena described in this chapter, which largely reflects my research work from 2002 to about 2008, the year in which I turned more towards data analysis. The IPNL group, with preprocessing, spectral data reduction written by Y. Copin, calibration by C. Buton and responsibility for production since the arrival of R. Pereira, was thus able to play a central role in the reduction of the instrument data within the collaboration.

This work was also an opportunity to train students, first Olivier Perrusol, a third-year intern, then Nathalie Blanc during her second-year internship and then her thesis, which included a section on the analysis of CCD data during the Lyon tests.

### **CHAPTER 3. USE AND IMPLEMENTATION OF CCDs FOR SPECTROGRAPHY**

---

## Chapter 4

# Analysis of spectral variability

### Summary

---

4.1 Automatic calculation of indicators . . . . .	68
4.2 Spectral indicators . . . . .	71
4.2.1 Silicon lines.	71
4.2.2 Calcium Lines.	74
4.2.3 Principal component analysis.	76
4.3 The maximum color law.	79
4.3.1 Color law or extinction law.	79
4.3.2 Calculation of magnitudes.	81
4.3.3 Corrections by intrinsic parameters.	82
4.3.4 color law . . . . .	82
4.3.5 Results.	85
Contributions . . . . .	86

---

The study of correlations between the spectral structures of supernovae and their variability was initiated by the pioneering work of [Nugent et al. \(1995\)](#), who detected correlations between the magnitude at maximum luminosity in band B with, on the one hand the ratio of Si II  $\lambda$ 5972 and Si II  $\lambda$ 6355 lines , and on the other hand the ratio of the fluxes on either side of the Ca II H&K absorption structure between 3925 and 3650  $\text{\AA}$ . The IPNL group was involved in the theoretical explanation of these correlations with the thesis of Sébastien [Bongard \(2005\)](#). In 2008, when Nicolas Chotard started his thesis, SNFactory data was starting to be sufficiently reduced to consider studying the correlations of these indicators with the supernova variabilities in our own data. These studies are currently still in progress, and described for the most part in Nicolas's thesis ([Chotard et al., 2011](#)), currently being writing under my direction. We will therefore limit ourselves here to summarizing the main stages and questions, and invite the reader keen on details to consult Nicolas's thesis for more further information.

We initially focused on visible spectral data at maximum brightness, which are the most studied in the literature, with a tolerance range of  $\pm 2.5$  days, during which the temporal variations are of low amplitude. The spectra considered in this chapter have all been corrected for Galactic extinction, as well as for the shift towards the red in order to be placed in the frame of reference at rest of the supernova. According to the studies performed, the normalization between the spectra will be done either absolutely, using the redshift data, either relatively by normalizing by the integral of the flux over

CHAPTER 4. ANALYSIS OF SPECTRAL VARIABILITY

---

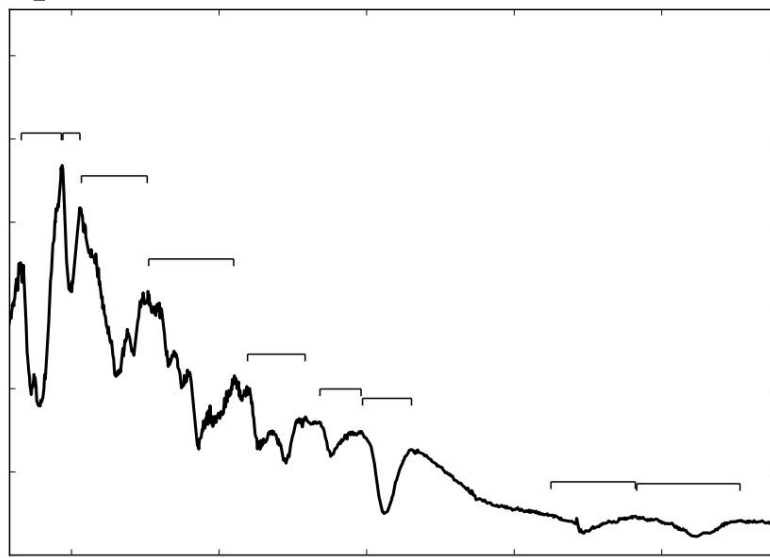


Fig. 4.1: Typical spectral structures observed at maximum brightness.

a given wavelength range. Finally, for some comparative studies, the spectra were sampled on the same wavelength grid.

The different lines visible at the maximum in the SNIFS spectra are shown in Figure 4.1. The variability of these spectra can certainly be studied directly on the raw spectral data, which comprise about 2000 spectral bins. However, we can take advantage of the existence of physical laws underlying spectral formation in order to reduce the dimensionality of the space to be studied: this is what led us to focus on the notion of spectral indicators.

## 4.1 Automatic calculation of indicators

The indicators considered in the literature are of several types, as shown in Figure 4.2.

They are based on the analysis of either the peak height ratios between two spectral structures, which are ultimately flux ratios, or on the analysis of absorption structures. For the latter, the effective velocity of the corresponding P-cygni profile, as measured from the flux minimum, is defined:

$$\frac{v}{c} = \frac{\bar{\lambda}_0 - \bar{\lambda}_{\min}}{\bar{\lambda}_0} \quad (4.1)$$

where  $\bar{\lambda}_0$  is the wavelength of the resting line, or effective wavelength in the case of a multiplet, and  $\bar{\lambda}_{\min}$  the wavelength of the observed flux minimum. The other global quantity that allows us to characterize these lines is a measure of the absorption level defined with respect to a pseudo-continuum, either by calculating a line depth at the minimum wavelength, or an equivalent width, both being largely redundant. We have only used the second, which also has the advantage of taking into account the details of the profile of the

#### 4.1. AUTOMATIC CALCULATION OF INDICATORS

---

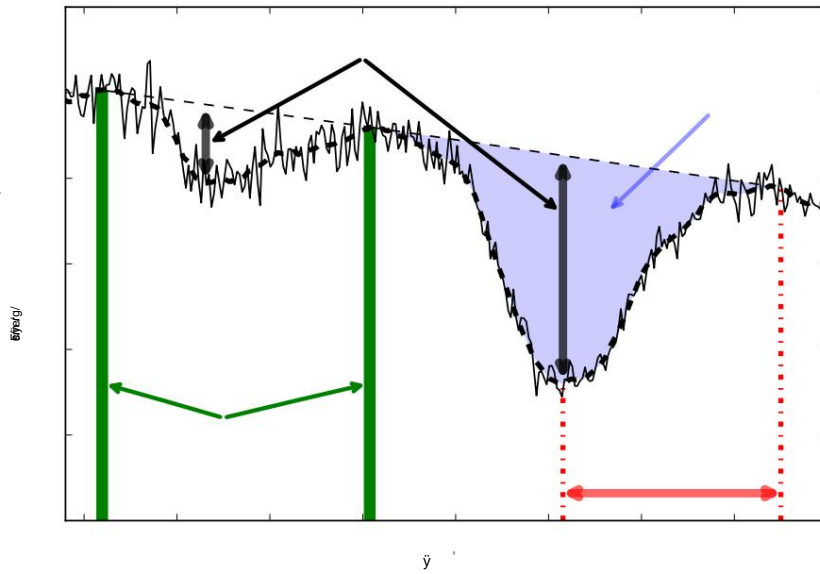


Fig. 4.2: Definition of various types of spectral indicators.

structure. We therefore define the equivalent width by

$$EW = \frac{\int_{\tilde{y}_1}^{\tilde{y}_2} f(\tilde{y}) d\tilde{y}}{\int_{\tilde{y}_1}^{\tilde{y}_2} f_c(\tilde{y}) d\tilde{y}} \quad (4.2)$$

where  $\tilde{y}_1, 2$  are the limits of the absorption line,  $f$  the observed flux, and  $f_c$  the flux of the pseudo-continuum obtained by linear interpolation between the fluxes observed at wavelengths  $\tilde{y}_1, 2$ .

To put these definitions into practice, it is necessary to determine the characteristic wavelengths of the structure boundaries, defined by the wavelengths of the two intensity peaks surrounding them, as well as the minimum wavelength that defines the velocity. To improve the accuracy on these wavelengths, smoothing of the data must be performed, with automatically determined parameters. Our criterion is based on minimizing the error on the smoothed function in order to achieve an optimal approximation. Indeed, by modeling the smoothing by the linear transformation

$$Y^{\tilde{y}} = BY \quad (4.3)$$

where  $Y$  is the data vector, and  $B$  is a matrix, it can be shown that the expected error between the approximated data  $Y^{\tilde{y}}$  and the unknown true values  $Y$  is given by

$$EY^{\tilde{y}} - Y^{\tilde{y}} = EY^{\tilde{y}} - Y + 2 \operatorname{Tr} B \tilde{y} n \quad (4.4)$$

where the norm is here understood to be normalized by the weight matrix of the measure:  $\tilde{y}Y = \tilde{y}Y + W\tilde{y}$  and  $n$  is the rank of the vector  $Y$ . Optimizing the procedure therefore consists of finding the transformation  $B$  that minimizes the above quantity. However, we only have one realization of the noise, this makes the matrix  $B$  dependent on  $Y$  which makes the process non-linear. In order to reduce the number of degrees of freedom of the system and reduce the risks of overtraining, the matrix  $B$  has been parameterized by a single degree of freedom,  $B(s)$ , corresponding to a family of approximations depending on a parameter,  $s$ . Likewise in order to model at

---

**CHAPTER 4. ANALYSIS OF SPECTRAL VARIABILITY**


---

better the approximation on the areas of interest — we only test an average deviation from the unknown function, and therefore local deviations can be significant — we cut the initial spectrum into small areas and the parameter  $s$  was optimized on each of them. Finally, knowledge of the matrix  $W$  plays a large role in the choice of  $s$ , hence the studies carried out to specify the structure of the spectral covariance, mentioned in chapter 2.

Two families of approximations were considered: splines, parametrized by a regularity parameter, and a Savitzky-Golay approximation, corresponding to a local parabolic adjustment on a window of width  $s$ . The latter were ultimately retained because on a small domain, adjustments by splines involve a small number of knots, which causes a significant jump in the quality of approximation when going from  $n$  to  $n + 1$  knots.

The procedure was validated by a Monte Carlo simulation, which takes as a starting point to which one the approximate spectrum adds from one to a thousand realizations of the noise of variance  $W\bar{y}^2$ .

This simulation allowed:

- To calculate the dispersion of the values obtained for the various realizations, as well as the average bias compared to the values calculated on the smoothed original spectrum, and to deduce the measurement uncertainties;
- To verify that the determination of the parameter  $s$  on a given spectrum corresponds within a certain range of uncertainty to the determination that we would have carried out on a large statistical set;
- To study various measurement biases: those linked to the signal-to-noise ratio, or those linked to the reddening linked to the host galaxy of the supernovae, which for the latter have proven to be negligible on EW measurements to within 1%.

Figure 4.3 shows as an example the approximation obtained for two lines that we will study extensively later, Ca ii H&K and Si ii  $\lambda 4131$ . Our fitting procedure is satisfactory, with two exceptions: the first concerns the fact that Savitzky-Golay only allows an extremum to be determined at the location of a measurement point. Given the width of the lines, and therefore the uncertainty about the locii of the extrema, this concern is not a problem.

The other source of potential improvement comes from the use of the  $W$  matrix : in some cases, the presence of noise not represented by this matrix, whether linked to a cosmic mismatch, can be a problem.

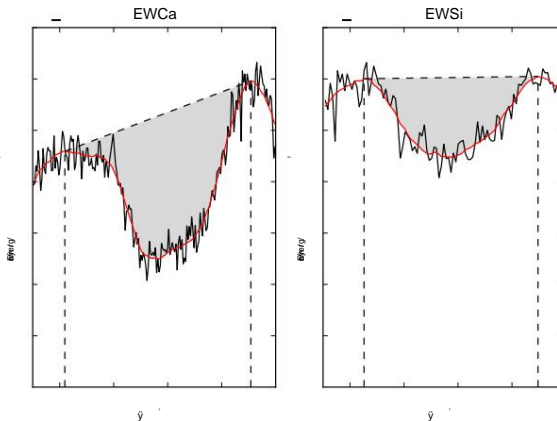


Fig. 4.3: Example of the optimal Savitzky-Golay approximation for two spectral regions, on the left Ca ii H&K, on the right Si ii  $\lambda 4131$ . The original spectrum is in black, and the smoothed spectrum in red.

---

## 4.2. SPECTRAL INDICATORS

subtracted or, in the red, to sky line residues, leads to obtaining an approximate spectrum that is too noisy, or even to determining the position of the maxima on artifacts. To improve the procedure, it would be advisable to tabulate the expected values of  $s$  as a function of the region considered and the expected average signal-to-noise ratio, in order to give more robust results. As it stands, after automatic production of the data, the verification carried out on control graphs shows that for approximately 10% of the spectra, one of the 9 equivalent depths was incorrectly measured, which leads to excluding the spectrum in question according to the analyses considered.

for which one of the 9 lines was poorly determined.

## 4.2 Spectral indicators

Among the various spectral indicators, we will not consider here the flux ratios between two wavelengths. Indeed, these are affected by the reddening due to absorption by the dust of the host galaxy of the supernova, and therefore contain a source of variability extrinsic to it. Certainly, in [Bailey et al. \(2009\)](#) we showed that using the ratio of fluxes at 6420 and 4430  $\text{\AA}$  allows us to obtain Hubble diagram residuals of 0.12 mag, instead of the 0.16 obtained by the classical method, a result confirmed since [\(Blondin et al., 2011\)](#), but the possible presence of extrinsic variability does not allow us to easily answer our problem, namely, how many parameters are necessary to describe the variations of supernova spectra.

In contrast, the equivalent line widths and velocities are largely independent of reddening. We will focus here on lines related to two elements, calcium and silicon.

### 4.2.1 Silicon lines

Figure 4.4 shows the relationships between the equivalent widths of the three Si lines (which we will denote EWSi4131 , EWSi5972 and EWSi6355 ) with the results of the SALT2 fit: the residuals to the Hubble diagram of uncorrected adjusted absolute magnitude,<sup>1</sup> Thus  $\bar{y}_{MB}$  , and the shape parameters  $x_1$  and color,  $c$ . We find the conclusions of [Arsenijevic et al. \(2008\)](#) who had noticed a strong anticorrelation between EWSi4131 and  $x_1$  (in our sample  $\bar{y} = \bar{y}0.77$ , as well as with  $\bar{y}_{MB}$ , as shown by [Brander et al. \(2008\)](#)). Moreover, if EWSi6355 shows an anticorrelation with  $x_1$ , this is of lower amplitude than for EWSi4131 .

The study of the relationships between the equivalent widths of Silicon, shown in Figure 4.5, leads to modeling their variations in the form of a 1-dimensional manifold in a three-dimensional space. Moreover, the observed relationships are non-linear, at least as far as  $EW(Si II \bar{y}6355)$  is concerned as a function of the others: this is the expected consequence of the saturation of this line. This implies that a modeling of the intrinsic spectral variability should take this non-linearity into account. Finally, [Branch et al. \(2006\)](#), confirmed by [Branch et al. \(2009\)](#) , use the graph EWSi6355 ,EWSi5972 to classify supernovae. Compared to their data, our figure covers a continuum from the region they call subluminous to the so-called narrow silicon region, which corresponds among others to the bright objects of the 1991T class, passing through the normal class. This seems to indicate the arbitrary nature of this classification, as we do not observe any continuity solution in our sample. Finally, we have only one object that marginally corresponds to the class they call wide silicon. This

<sup>1</sup> defined by  $\bar{y}_{MB} = m\bar{y}_b \mu(z) + C$ , where  $m\bar{y}_b$  comes from the light curve fitting,  $\mu(z)$  is the distance modulus ,  $C$  a constant

## CHAPTER 4. ANALYSIS OF SPECTRAL VARIABILITY

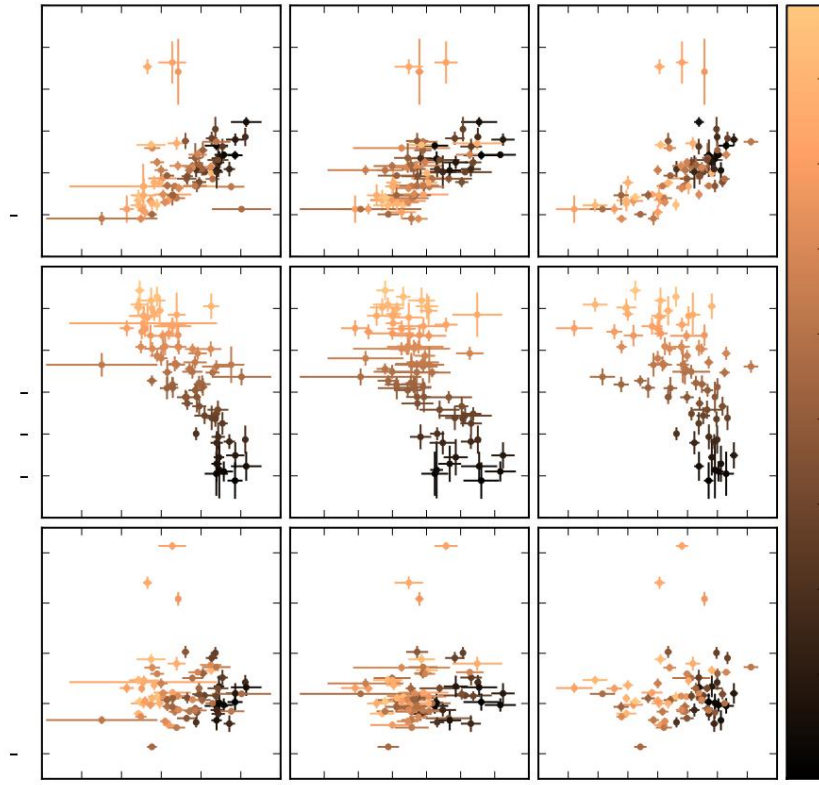


Fig. 4.4: Equivalent widths of silicon lines as a function of uncorrected residues in the Hubble diagram, and the parameters of the SALT2 model,  $x_1$  and the color  $c$ . The color code allows the values of  $x_1$  to be identified.

may be a selection effect related to the fit of the light curves to the SALT2 model, and further studies will be necessary to clarify this point. Compared to the historical indicator  $\text{RSi} \ddot{\gamma} \text{EWSi5972} / \text{EWSi6355}$ , we have also concluded from our studies that its correlation to the magnitude comes essentially from the correlation between  $\text{EWSi5972}$  and  $x_1$ .

The velocity of the  $\text{Si ii} \ddot{\gamma} 6355$  line is an indicator of the kinetic energy of the expanding envelope, and its gradient was used by [Hachinger et al. \(2006\)](#) to recover the supernova classes defined by [Branch et al. \(2006\)](#). [Wang et al. \(2009\)](#) showed that a gradient-based classification is equivalent to a velocity-based classification, and suggested that the reddening law would be different depending on the class of supernovae studied. If we lack data for the high-velocity class, corresponding to the broad silicon class of [Branch et al. \(2006\)](#), we can however study the variability of this speed as a function of equivalent widths (see Figure 4.6). If, for the supernovae in our sample we observe a correlation with  $\text{EWSi}$ , we do not observe any correlation with  $x_1$ , which implies that the variations of  $v_{\text{Si}}$ , and therefore of the kinetic energy of the external layers, are not correlated with the total energy released by the explosion: we have here the indication that there is a source of intrinsic variability in addition to  $x_1$ .

## 4.2. SPECTRAL INDICATORS

---

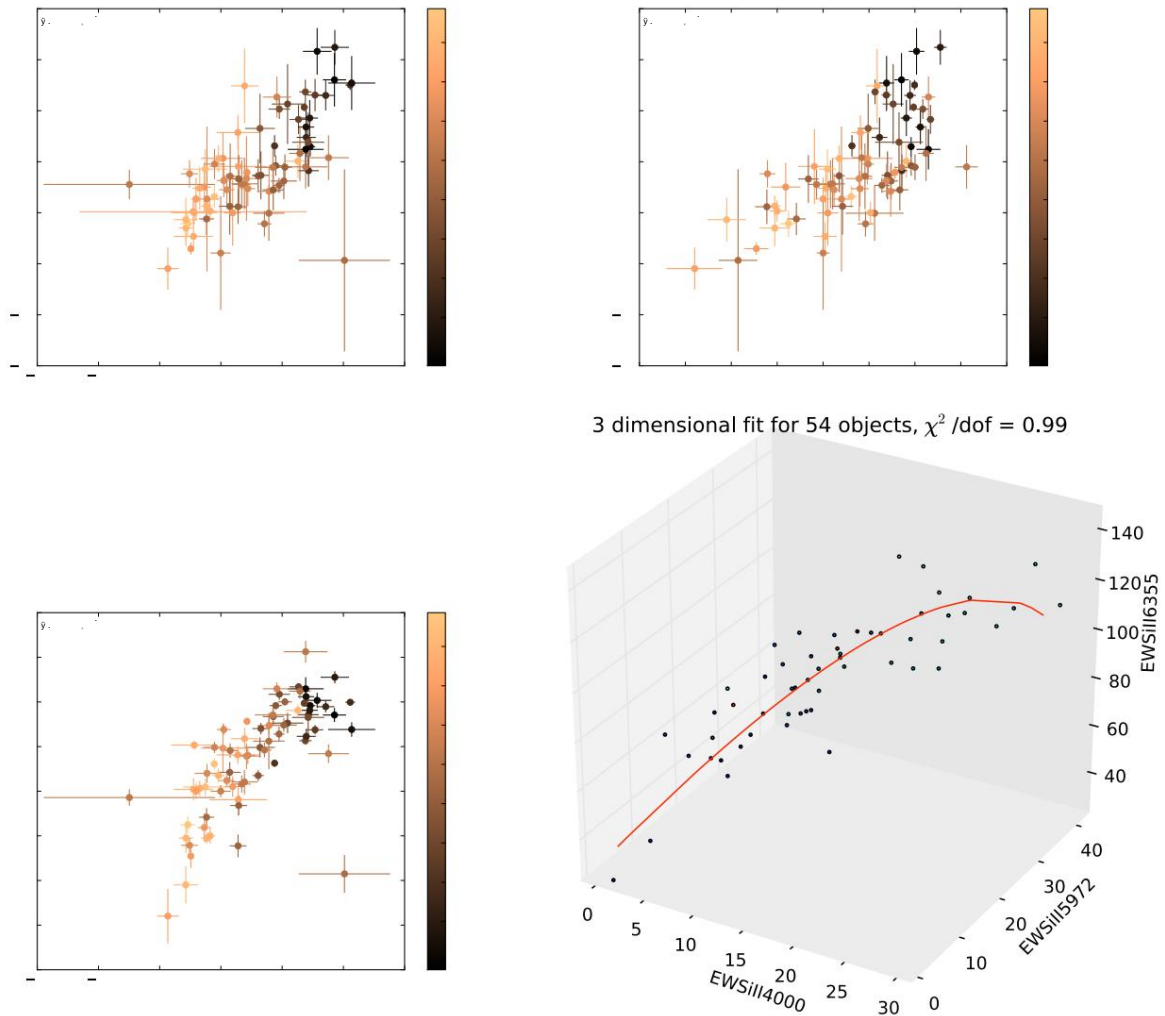


**Fig. 4.5: Relationships between the various equivalent widths of Silicon.**

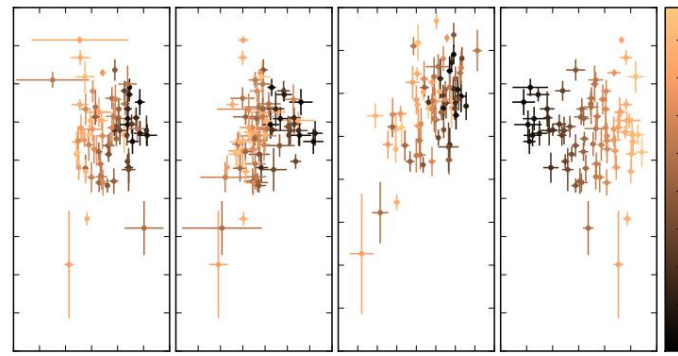


**Fig. 4.6: Relations between the speed of the Si II 6355 line and on the one hand the equivalent widths of other silicon lines, and on the other hand x1.**

## CHAPTER 4. ANALYSIS OF SPECTRAL VARIABILITY

---

### 4.2.2 Calcium Lines

The UV part of the supernova spectrum is the region in which metallicity effects are expected (see for example [Hoeflich et al., 1998](#) or [Lentz et al., 2000](#)). The variability in this region was studied by [Ellis et al. \(2008\)](#) who excluded that it was mainly related to color, without being able to relate it to other parameters, except for a phase dependence of two peaks with wavelengths below  $3200\text{\AA}$ , inaccessible to SNIFS.

Furthermore, [Kessler et al. \(2009\)](#) showed that the greatest difference between the MLCS2k2 and SALT2 empirical models appeared in the UV. The study of this region is therefore particularly interesting for our problem.

The R<sub>Ca</sub> ratio defined by [Nugent et al. \(1995\)](#) and corrected by [Bongard et al. \(2006\)](#) did not prove relevant for the study of this region: we found that the bounds defined by these authors do not correspond to peaks on the spectra, in a region where the spectral shape is very variable (see Figure 4.7), in particular with regard to the bluest peak, the choice of which will give rise to a selection of different underlying structures, and thus will blur a correlation with precise physical parameters. Moreover, a large part of the correlation detected by [Nugent et al. \(1995\)](#) can be related to color. In order to ensure that we are measuring intrinsic properties, it is therefore appropriate to take an indicator that is insensitive to the presence of dust—whether or not it is the cause of the observed color law—which is what EWCaH&K does .

Figure 4.8 shows the correlations of EWCaH&K and EWCaIR with the SALT2 parameters: while the UV line does not show significant correlations with  $x_1$ , this is not the case for the IR line (see Table 4.1), whose behavior is similar to that of the silicon lines, namely, a less marked line for more luminous supernovae. However, it has a marginal correlation to EWCaH&K with a Pearson correlation coefficient of  $\gamma = 0.33 \pm 0.10$ , which is much lower than when comparing the silicon lines with each other. It is therefore difficult to conclude regarding the origin of the variations in the UV line, which could therefore be linked to the influence of Ca ii, but also to other sources such as the variations affecting the blue terminal

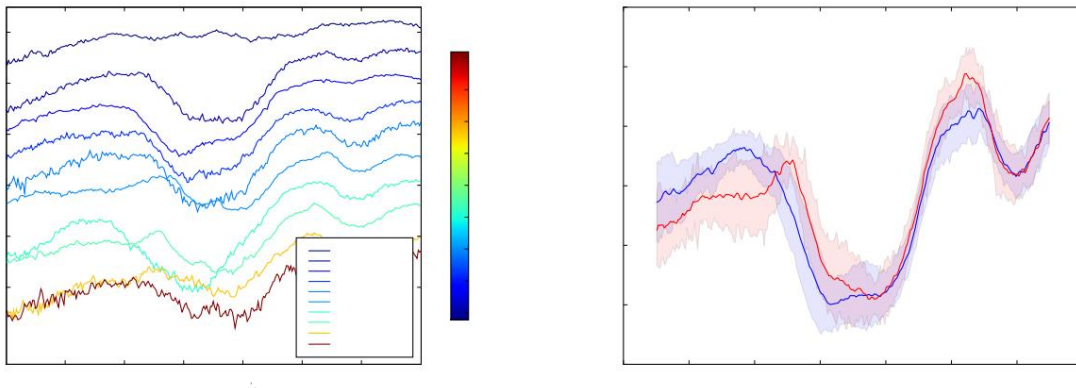


Fig. 4.7: Illustration of the variability of the calcium zone. Left: some spectra classified according to their Hubble diagram residue. Right: average spectra obtained after correction of their SALT2 color, in blue for the half with the largest  $y_2 - y_1$ , in red, the half with the smallest  $y_2 - y_1$ , for the same average value of  $x_1$ , the normalization between the two curves being arbitrary here.

---

4.2. SPECTRAL INDICATORS

---

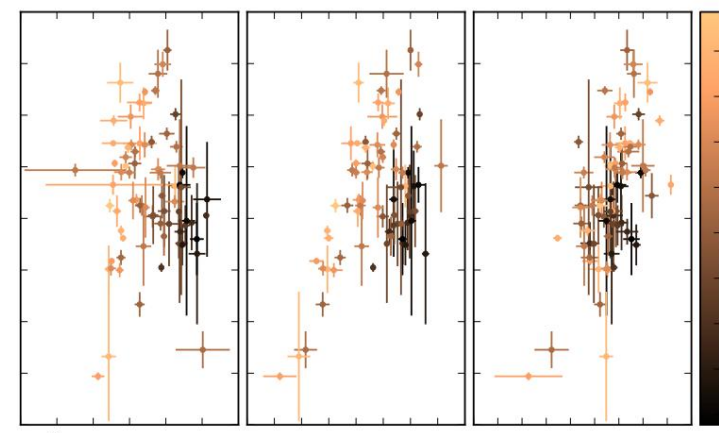
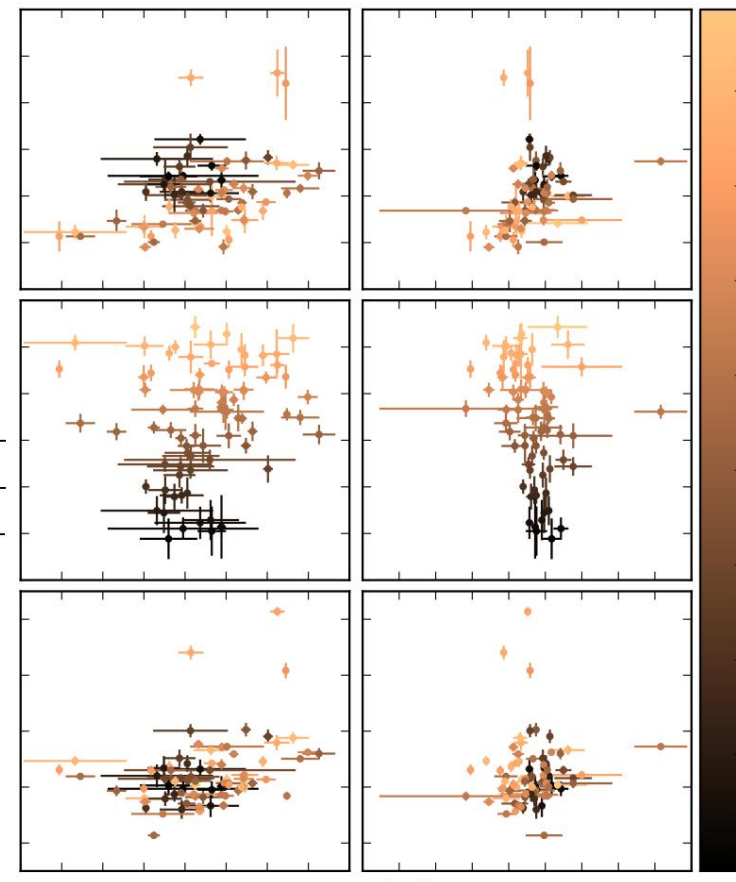


Fig. 4.8: Correlations between the depths of the two calcium lines with the supernova parameters determined by SALT2, and on the other hand with certain indicators corresponding to silicon.

## CHAPTER 4. ANALYSIS OF SPECTRAL VARIABILITY

---

of the UV structure, or the mixture with lines of other elements.

The fact that EWCaH&K is not correlated with  $x_1$  is also reflected in its absence correlation with EWSi4131, while it is significantly correlated with EWSi6355 and vSi6355 : Here again we have an indication that a new parameter must be introduced in order to model the intrinsic variabilities of supernovae. Finally, the correlation of EWCaH&K with the color is also significant, and even more so if we redo the SALT2 adjustment by incorporating the U band (see Chotard, 2011 for more details). This is an important indication that shows that the SALT2 color contains an intrinsic contribution to the supernova.

### 4.2.3 Principal component analysis

Given the large number of indicators to be processed, we carried out a preliminary analysis in principal components on the equivalent widths, in order to determine the power of the various eigenvalues as well as the nature of the associated eigenvectors. This analysis uses all 9 equivalent widths available on the spectrum, in the order Ca ii H&K,

Si ii  $\lambda$ 4131, Mg ii Fe ii Ca,ii IR, as described in Si ii  $\lambda$ 5972, Si ii  $\lambda$ 6355, O i

**Figure 4.1.**

First, we considered the evolution of these equivalent widths as a function supernova parameters from SALT2 adjustments, such as  $(x_1, c)$ , but also parameters specific to the spectrum such as the phase  $p$ , or the red shift  $z$  which can trace an evolution linked to the signal-to-noise ratio, or selection effects. The only correlation significant observed between these four parameters is an anticorrelation between color and spectral shift ( $\hat{y} = \hat{y}(0.4)$ ) : it is the result of a Malmquist bias on supernovae more reddened, which are only observed at low redshift, being less luminous than the others.

Table 4.1 shows the correlations between external parameters and equivalent widths. The evolution with  $x_1$ , predictable, indicates a general tendency towards less marked lines for brighter supernovae, which is generally explained by higher degrees of ionization raised in the supernova envelope. On the other hand, the possible correlation of EWCaH&K with color is of a new nature: the equivalent widths being insensitive by construction to dust reddening, this could be indicative of an intrinsic contribution from the supernova to the color parameter. Finally, a correlation with the phase is observed, essentially for the O i line, little studied elsewhere in the literature: although restricted around the maximum, the width of the window in time is sufficient to make appear phase effects.

The decomposition into principal components, made by normalizing the values to their dispersion and by discarding two particular supernovae from the lot, gives three principal vectors which make

**Tab. 4.1: Correlations between the equivalent widths of the mentioned lines and the parameters external parameters to characterize the data. Numbers in bold are significant at more than  $3\sigma$ , the typical uncertainty being of the order of 0.12 for  $\hat{y} = 0$ .**

Param.	Ca ii H&K	Si ii $\lambda$ 4131	Mg ii Fe ii	S ii W	Si ii $\lambda$ 5972	Si ii $\lambda$ 6355	O i Ca ii IR		
$x_1$	0.22	-0.83	-0.63	<b>-0.062500</b>	<b>0.520.012</b>	<b>-0.0610.09</b>	-0.66		-0.58
$c$	0.35			<b>0.11</b>	<b>0.31</b>	<b>0.15</b>	<b>0.04</b>	0.12	<b>-0.27</b>
Phase	-0.14			<b>-0.18</b>	<b>0.19</b>		<b>0.17</b>	<b>0.16</b>	0.51
$z$	-0.06					<b>0.13</b>	<b>-0.06</b>		<b>0.19</b>

## 4.2. SPECTRAL INDICATORS

---

**Table 4.2: Decomposition into principal components.** The first table gives the relative value eigenvalues normalized to 1; the second table indicates the decompositions of the three first eigenvectors, highlighting the most important ones in bold, and the last line gives the correlations with the parameters determined elsewhere for the first three components, the correlations being non-significant for the following ones.

Vector	1	2	3	4	5	6	7	8	9
PV	0.51	0.22	0.11	0.05	0.03	0.03	0.02	0.02	0.01

Param. Ca ii H&K Si ii $\dot{y}$ 4131 Mg ii Fe ii S ii W Si ii $\dot{y}$ 5972 Si ii $\dot{y}$ 6355 O i Ca ii IR	Vec. 1	Vec. 2	Vec. 3					
-0.49 -0.01 <b>0.29</b> <b>0.09</b> <b>0.04</b> -0.46	-0.35 -0.20 <b>0.30</b>	-0.10	-0.38				<b>-0.22</b>	-0.37
0.70	<b>0.20</b> <b>0.33</b> 0.19	0.12	-0.26				-0.44	<b>0.08</b>
-0.12		-0.09	-0.43				<b>0.38</b>	0.53

Param.	Vec. 1	Vec. 2	Vec. 3
x1	0.67	0.48 <b>0.12</b>	
c	<b>-0.08</b>	0.35 <b>-0.15</b>	
Phase	-0.24 -0.03	<b>-0.20</b> <b>0.28</b>	
z		-0.08	<b>0.24</b>

accounts for 84% of the observed variance (see table 4.2). The first vector is essentially correlated with  $x_1$ , and corresponds in part to the intrinsic variability already known for the supernovae. The second eigenvector accounts for a significant fraction of the variance, and as expected is strongly correlated with EWCaH&K . It also shows correlations with  $x_1$  and color, which confirms our idea that this is a significant variability of our sample, and that a complete model should take this variability into account. Finally, The interpretation of the third eigenvector does not lead to any firm conclusion, except that the presence of a third eigenvector at about 10% of the total variance is robust when changes the details of how to do the PCA This transformation, based on the indicators spectral, in fact involves a part of arbitrariness in the number of indicators chosen where the relative normalization of the input components. Moreover, the orthogonalization operation does not guarantee that the observed vectors correspond to underlying physical variables, even if it is indicative of the number of parameters to take into account.

Once the vectors are identified, it is possible to determine a spectral model that describes the spectrum of a supernova given  $i$  by

$$I_f = S_0 + \sum_i \hat{y}_{ij} S_j \quad (4.5)$$

where  $\hat{y}_{ij}$  are the coordinates of the supernova in the eigenvector space, truncating the series to the first three vectors. In order to reduce the share of variance corresponding to the reddening, we corrected each spectrum for its SALT2 color, by multiplying it by  $\exp(cCL(\hat{y}))$  as defined in Guy et al. (2007). This transformation in fact leaves the invariant depths, which allows the use of  $\hat{y}_{ij}$  from the PCA and will allow to study local variations even if the overall shape of the spectra will only be defined at a low frequency component nearby.

The result is shown in Figure 4.9. The first eigenvector actually corresponds to a global correlation between the depth of the structures, the second vector accounts for a increased variability mainly in the UV part, with the notable characteristic that

## CHAPTER 4. ANALYSIS OF SPECTRAL VARIABILITY

---

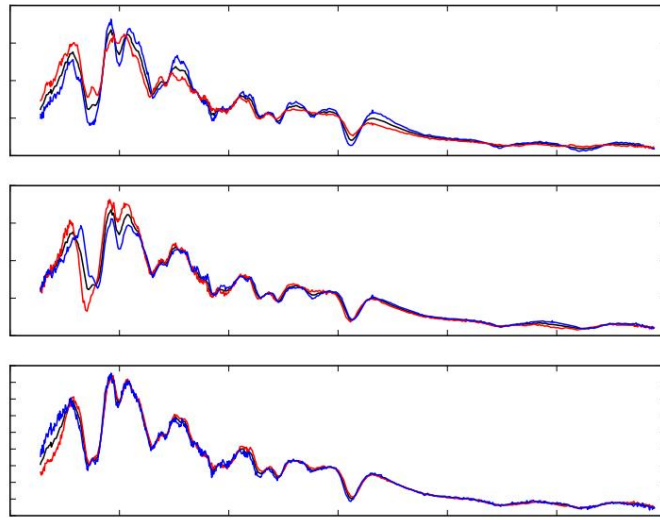


**Fig. 4.9:** Variability of the supernova decomposed on the first three eigenvectors determined by PCA on the spectral indicators. The average spectrum is shown in black, the spectra in red and blue correspond to a variation of  $\pm 1\sigma$  along the considered eigenvector. The flux normalization is arbitrary.

EWSi4131 is relatively unaffected while the average spectrum undergoes both a shift in relative amplitude and wavelength. Finally, the third eigenvector shows low line velocity variability as well as high variability in the UV, all the more remarkable since it corresponds to a region that is not traced by the spectral indicators used, which reinforces the plausibility of a third source of variability. However, this region, bluer than the Ca ii H&K, is also very sensitive to the phase at which the spectrum is acquired, even if the observed correlations are marginal, and a  $2\sigma$  correlation with the redshift is observed for this third vector. Some caution is therefore required and the addition of line velocities in the PCA would be the natural next step to continue this work.

This preliminary study has therefore highlighted the presence of additional components that can account for the variability of supernovae. However, a modeling of the spectra must fully take into account the color dependence that we have treated here as if it were entirely extrinsic despite an observed  $3\sigma$  correlation between the color parameter  $c$  and certain spectral characteristics. Furthermore, when we corrected the SALT2 color spectra, we found that the underlying model did not seem to account well for our observations, as shown in Figure 4.10 : the SALT2-modeled spectrum appears to deviate from our average spectrum in the UV, and furthermore, the most reddened supernovae are over-corrected as indicated by the overall color distortion of their spectrum relative to the corrected average spectrum.

### 4.3. THE LAW OF COLOUR AT MAXIMUM

---

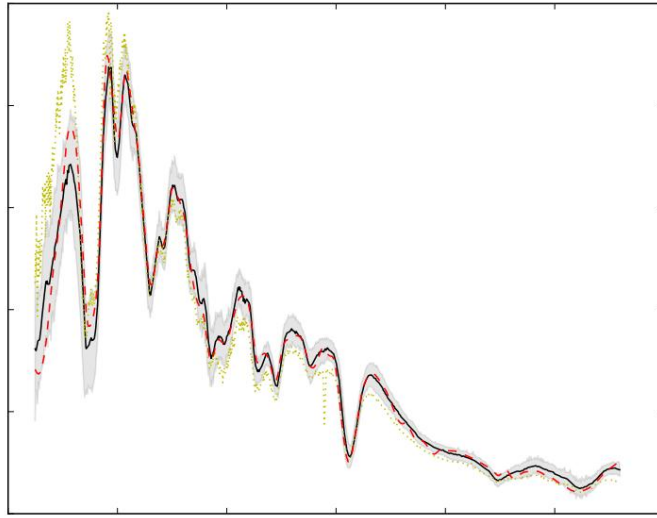


**Fig. 4.10:** Average spectrum obtained after correction by color  $c$ , in black, with a gray band indicating the variation at  $\pm 1 \sigma$ . In red, the average spectrum modeled by SALT2 for this sample. In yellow dotted lines, the average spectrum corrected for our three most red.

## 4.3 The maximum color law

Armed with the assumption of the existence of a second intrinsic parameter on the one hand, and of a deviation from the SALT2 color law on the other hand, in Chotard et al. (2011), we sought to establish a complete model by establishing an empirical extinction law. Although we invite the reader to refer either to the aforementioned article or to Nicolas Chotard's thesis (2011) for more details, given the importance of the result we will develop our method here.

### 4.3.1 Color law or extinction law

The SALT2 approach models the temporal evolution of the supernova spectrum as follows:

$$S(p, \dot{y}) = x_0(p, \dot{y}) [S_0(p, \dot{y}) + x_1 S_1(p, \dot{y})] \exp(\dot{y}c CL(\dot{y})) \quad (4.6)$$

where  $S_0$  and  $S_1$  are phase-dependent spectral (flow) patterns  $p$ ,  $CL(\dot{y})$  a color pattern chosen as a polynomial of order 3 or 4 depending on the versions considered.  $x_0$ ,  $x_1$  and  $c$  are fitted to the data, and the relationship between  $x_0$ ,  $x_1$  and  $c$  is implicitly determined at the time of distance estimation:

$$m_B = \mu(z) + M_0 - B - \dot{y}x_1 + \dot{y}c \quad (4.7)$$

where  $\mu(z)$  is the distance modulus,  $B$  is the magnitude in B calculated by integration over  $m_B$  fitted model  $S$ , and  $M_0$ ,  $\dot{y}$ ,  $\dot{y}$  are adjusted in order to minimize the residual dispersion in the diagram of Hubble. By applying this approach to our data, as indicated in Chapter 2, we

## CHAPTER 4. ANALYSIS OF SPECTRAL VARIABILITY

---

We obtain a dispersion of the residuals in the Hubble diagram of 0.16 mag. Using EWSi4131 instead of  $x_1$ , we obtain the same dispersion, which shows that in our data EWSi4131 has the same standardization power as  $x_1$ : this allows us to free ourselves from an underlying model of spectral patterns, and we will therefore use EWSi4131 in the following as an indicator of intrinsic variability linked to stretch.

SNfactory data in principle allow us to study the spectral color law up to the resolution of the instrument, avoiding polynomial modeling as is the case in SALT2. Moreover, since our data come from nearby supernovae,  $\mu(z)$  will be independent (to within 1%) of the cosmological parameters. We can therefore directly model the observed spectrum of a supernova  $i$ , in magnitude AB, by

$$M_{\text{obs},i} = \mu(z) + M_0 + \sum_j x_{j,i} s_j + A_{j,i} \quad (4.8)$$

where  $M_0$  would be the average spectrum observed in the absence of absorption  $A_{j,i}$ ,  $x_{j,i}$  is the  $j$ th external  $j$  measured on supernova  $i$ , such as an equivalent width, and corresponding spectral  $s$ . The absorptions  $A_{j,i}$  is the boss are related to each other by the empirical extinction law

$$A_{j,i} = \frac{A_{j,V}}{V} \quad (4.9)$$

where  $A_{j,V}$  is the absorption in V band V special case of an  $\text{eme}$  parameter, and  $\text{eme}$  the unknown law that we seek to establish. In the extinction of Cardelli et al. (1989),

$$A_{j,i} = a_{j,i} + \frac{b_{j,i}}{RV} \quad (4.10)$$

where  $a_{j,i}$  and  $b_{j,i}$  are given by O'Donnell (1994), and RV is an adjustable parameter.

This approach, although it seems similar to that of SALT2, has however an important difference: SALT2 in fact leaves free the absolute normalization of the supernova, through the parameter  $x_0$ , where our approach fixes the amplitude of the average spectrum at a given distance,  $M_0$ . The consequence is that SALT2 gives a measurement of the color  $c = E(B - V) = AB - AV$  where we seek directly to determine  $AV$ . We therefore directly measure an extinction law  $\text{eme}$ , where SALT2 will only measure a color law,  $CL(\text{eme}) = \text{eme} - \text{eme}_B$ , which it will be possible to interpret in a second step as an extinction law by adjusting  $\text{eme}$ . One of the objections often raised against attempting to directly determine extinctions is the lack of a statistically significant and unbiased reference group with zero extinction.

In our approach, we bypassed this problem by only considering the residuals in the Hubble diagram:

$$\text{residual} = M_{\text{obs},i} - M_{\text{pred},i} = M_{\text{obs},i} - (\mu(z) + M_0 + \sum_j x_{j,i} s_j) \quad (4.11)$$

$$= A_{j,i} + \text{eme} \quad (4.12)$$

with  $\text{eme} = A_{j,i} - A_{j,V}$ : we therefore free ourselves from the definition of the zero point of the analysis by choosing an average extinction, and must then adjust the empirical extinction law by

$$\text{eme} = \text{eme}_V + \text{const} \quad (4.13)$$

where  $\text{const}$  is a constant: the analysis is thus invariant under a translation in magnitude.

### 4.3. THE LAW OF COLOUR AT MAXIMUM

#### 4.3.2 Calculation of magnitudes

We operated on two datasets in parallel, coming from the same initial spectra. First, the spectra were binned at 1500 km/s, then we calculated the Hubble residuals before correcting them for phase by

$$\hat{y}M_{\hat{y},i} = \hat{y}M_i + ps^{\frac{p}{\hat{y}}} \quad (4.14)$$

where the phase p is given by the SALT2 fit, and s is determined by least squares on the sample, taking into account uncertainties in p and  $\hat{y}M_{\hat{y},i}$ . These were determined from the measurement uncertainty, evaluated by the deviation from SALT2 of the light curves, as described in Chapter 2. Added to this is the propagation of uncertainties related to the redshift, which strongly correlate the covariance matrix between the various wavelengths.

The other dataset consists of magnitudes reconstructed in 5 synthetic filters of constant resolution between 3276 and 8635 Å. Since a linear interpolation between phases is not suitable when we are close to the maximum of the light curve, we used the shapes of the adjusted light curves to calculate in each band taken independently the magnitude at the date of the maximum using all the data between -10 and +10 days around the maximum: in fact, the SALT2 model does not go down to our spectral resolution, it would have been risky to rely on it to establish an interpolation on the spectral data, while it was adjusted to reproduce the light curves in broad band. A future improvement of phase interpolation in the case of spectral data could be the use of higher-order derivatives, provided that we can determine that these are measurable with significant accuracy, pending the development of a complete phase model.

Figure 4.11 shows as an example this procedure applied to SNF20080522-000. Another

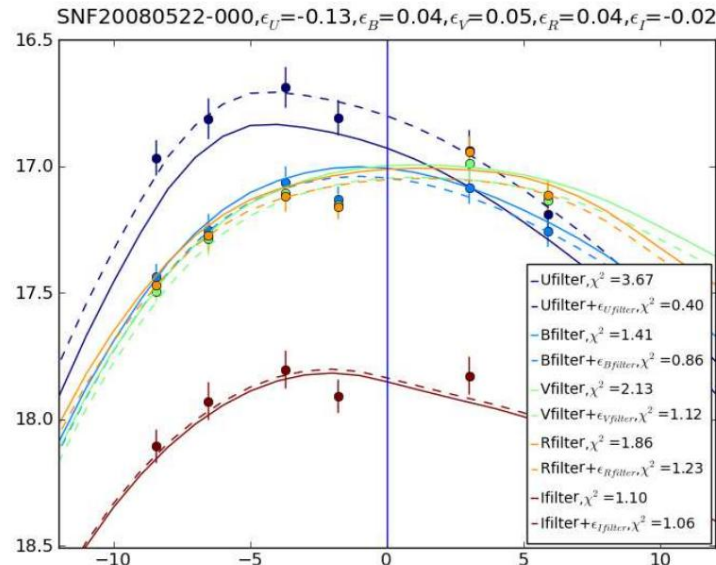


Fig. 4.11: Magnitude interpolation in synthetic filters using SALT2 light curves. The solid curves are the magnitudes determined by SALT2, the dotted curves are the curves fitted to the data, indicated by colored points with their uncertainties.

## CHAPTER 4. ANALYSIS OF SPECTRAL VARIABILITY

---

One of the advantages of this procedure is to reduce the uncertainty in the calibration to about 0.02 mag by the averaging effect on the measurements.

### 4.3.3 Corrections by intrinsic parameters

Figure 4.12 shows as an example the relationships between the residuals in the Hubble diagram in B with EWSi4131 : we observe a linear relationship, to which is added a dispersion of magnitude which originates a priori from an intrinsic variability as well as from a dispersion extinction. Also, in our modeling,  $\bar{A}_y$  will only represent extinction at a residue of intrinsic fluctuation.

We were led to consider three hypotheses to model the intrinsic contribution:

$$\bar{y} \bar{y} A_0 \quad (4.15a)$$

$$\bar{y} M \bar{y}, i = \begin{cases} \text{EWSi4131 } s_{,i} & \text{if } \\ & \bar{y} + \bar{y} A_S \bar{y}, i \end{cases} \quad (4.15b)$$

$$= \text{EWSi4131 } s_{,i}^{Si} + \text{EWCaH\&K } s_{,i}^{Ca} + \bar{y} A_S \bar{y}, i \quad (4.15c)$$

The first, (Eq. 4.15a) corresponds to what the extinction would be if supernovae were purely standard candles. The second corresponds to the consideration of EWSi4131 for plot an intrinsic variability, and the latter taking into account both EWSi4131 and EWCaH&K to study the variability associated with this second potential parameter.

### 4.3.4 Color law

The adjustment of a color law hides a conceptual difficulty: taking into account intrinsic residual fluctuations of magnitudes. Indeed, the adjustment is done by the minimization of

$$2x = \sum_i \bar{y} A_i \bar{y} \bar{y} A \bar{y} \quad v, i \quad \bar{y} \bar{y}^T W_i \bar{y} A_i \bar{y} \bar{y} A \bar{y} \quad v, i \quad \bar{y} \bar{y} \quad (4.16)$$

where the notations  $A, \bar{y}, \bar{y}$  represent respectively the wavelength vectors  $A_i, \bar{y}_i, \bar{y}$  and  $\bar{y}$  and  $W_i$  is the inverse of the measurement covariance matrix for supernova  $i$  which takes into account account of correlations between wavelengths.

The values of the  $\chi^2$  per degree of freedom obtained after adjustment are however far from the unit, worth  $\chi^2/\text{ndf} = 11$  and  $\chi^2_{\text{If} + \text{Ca}} = 3$  in the respective hypotheses 4.15b and 4.15c, which shows that residual intrinsic dispersion must be taken into account. Figure 4.13 shows the

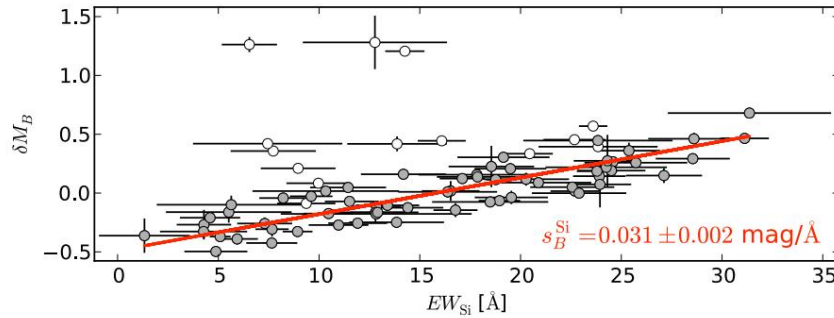


Fig. 4.12: Evolution of the magnitude measured in B with EWSi4131 . The red line represents a linear fit, open points were excluded from the fit.

---

### 4.3. THE LAW OF COLOUR AT MAXIMUM

---

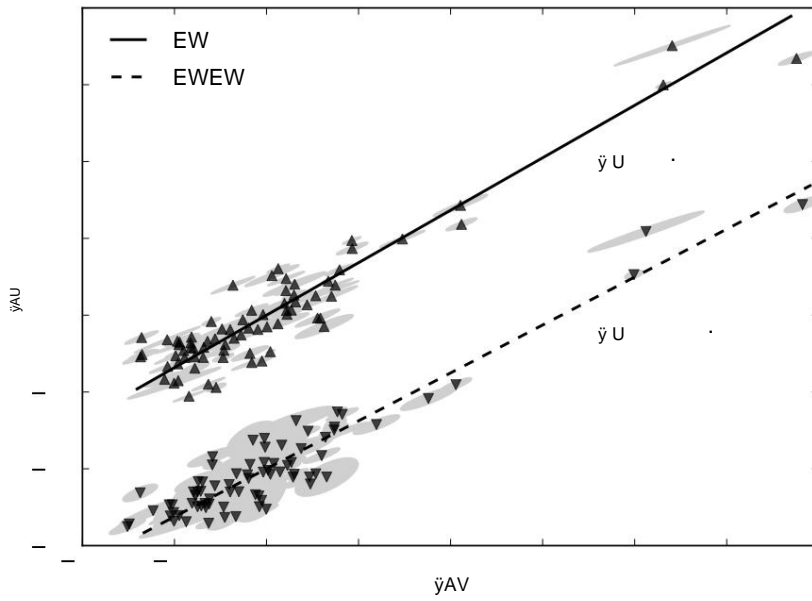


Fig. 4.13: Relationship between  $\bar{y}_{AU}$  and  $\bar{y}_{AV}$  after correction by EWSi4131 (triangles pointing up) or by EWSi4131 and EWCaH&K (triangles pointing down). The ordinate is given to within an arbitrary constant.

relationship between U and V absorptions : besides a linear relationship being appropriate, the points are naturally more dispersed than their uncertainty contours. These are larger after the correction linked to EWCaH&K because of the propagation of uncertainty on this last parameter.

We chose to take the additional dispersion into account by modeling it with an additional variance term to add to the measurement uncertainties. In principle, this matrix can be obtained by maximizing the expression of the logarithm of the Restricted Maximum Likelihood, an introduction to which can be found in [Guy et al. \(2010\)](#) as well as references for further study. Indeed, the expression of the likelihood corresponding to a least squares minimization is generally written

$$\bar{y}^2 \ln L = Y \bar{y} H X t^\dagger \quad W(Y \bar{y} H X t) \bar{y} \ln |W| + \text{Coast} \quad (4.17)$$

where  $X_t$  is the vector of true values of the parameters to be adjusted,  $Y$  the vector of measurements, with mean value  $H X_t$  and  $W$  the weight matrix. Since  $X_t$  is unknown, it is possible to replace it with its adjusted value  $X = H T W H \bar{y}^1 H T W Y$  which gives all calculations made

$$\bar{y}^2 \ln L = (Y \bar{y} H X)^\dagger W(Y \bar{y} H X) \bar{y} \ln |W| + \ln |H T W H| + \text{Coast} \quad (4.18)$$

However, the matrix  $W$  has  $n(n + 1)/2$  degrees of freedom for vectors of rank  $n$ , which is far too many for it to be reasonable to numerically perform the minimization of  $\bar{y}^2 \ln L$  in our case. We therefore used  $X = X_t$  as an approximation , which leads to neglecting the  $\ln$  term  $|H T W H|$  , whose influence becomes negligible in the statistical limit. In this case, we can obtain the elements of the variance matrix by

$$\bar{y}^2 \frac{\bar{y} \ln \bar{y}}{\bar{y} w_{ij}} = (Y \bar{y} H X) i (Y \bar{y} H X) j \bar{y} V_{ij} = 0 \quad (4.19)$$

## CHAPTER 4. ANALYSIS OF SPECTRAL VARIABILITY

---

where  $V = W\hat{y}V$ , which amounts to writing that  $V$  is the covariance matrix of the residues ( $\hat{Y}-HX$ ).

Adapted to our problem, this leads to writing that the dispersion matrix is worth

$$D = \frac{1}{N} \sum_i (a_{i,i} - \hat{y}_i^T \hat{y}_i) V_i \quad (4.20)$$

where  $r_i = \hat{y}_i A_i \hat{y}_i^T V_i$  if  $\hat{y}$  is the residual of the adjustment and  $V_i = W\hat{y}V$  the covariance matrix

measure of the supervova  $i$ . Because of the subtraction of the  $V_i$  the matrix  $D$  risks having negative eigenvalues, which we therefore set to 0 in order to have a positive dispersion matrix.  $D$  then intervenes in the minimization of the  $\hat{y}$  using as weight matrix  $W\hat{y} = (D + V_i)^{-1}$ , and we iterate the successive estimation of  $A\hat{y} V_i \hat{y}, \hat{y}$  and  $D$  until convergence.

We have analytically verified that the exact value of  $\hat{y}^T \ln L$ , i.e. without neglecting the  $\ln$  term  $|HTWH|$ , is by this procedure lower than any other value that we had obtained by modeling  $D$  with one or two free parameters. Furthermore, we have verified that the value after adjustment does not depend on the initial hypotheses on the matrix  $D$ , as long as these remain within a reasonable range. Finally, we validated this matrix by a Monte Carlo simulation, which takes as input the converged parameters  $\hat{y}$  and  $A\hat{y} V_i \hat{y}$  and simulates the  $A_i$  by adding a noise of variance  $V_i + D$ . The obtained convergence matrix is faithful to the original to within about 5% of its coefficients, as shown in Figure 4.14. It should be noted that our method is general in scope, and could very well be adapted to the minimization of the Hubble parameters by introducing an empirical dispersion between  $\hat{y} B, \hat{y}$  and  $\hat{y}$ : indeed, the classical choice of adding the dispersion magnitude is purely arbitrary.

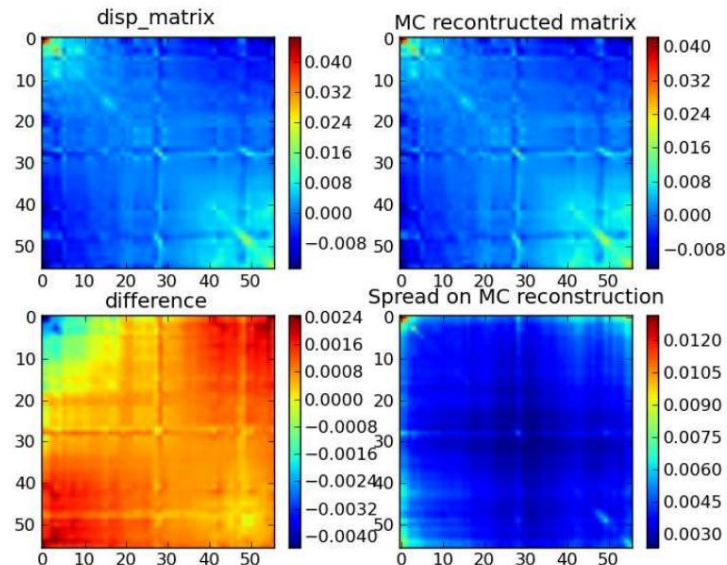


Fig. 4.14: Dispersion matrix obtained using spectral data as input. Top left, the initial dispersion matrix, top right, the average matrix reconstructed over 100 Monte Carlo simulations, bottom left, the average deviation between the initial matrix and the reconstructed matrix, and bottom right the standard deviation of the simulated matrices.

### 4.3. THE LAW OF COLOUR AT MAXIMUM

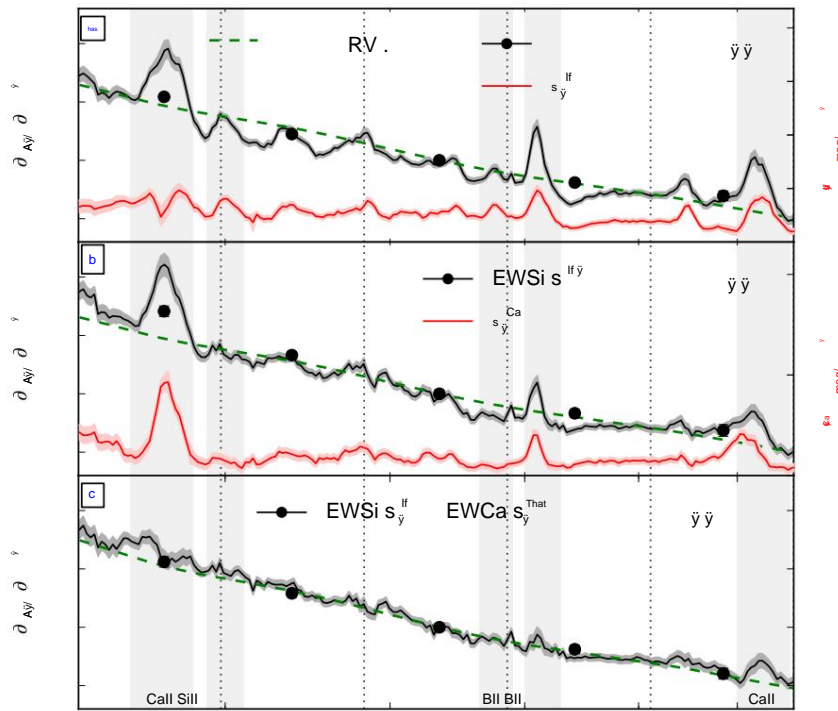


Fig. 4.15: Empirical extinction laws and correction vectors  $s\bar{y}$  under different assumptions. a) In black, the extinction law without correction of intrinsic parameters. The line corresponds to the spectral data, the points to the UBVRI synthetic filters. In red, the correction vector  $s$

$\ddot{y}$ . b) In black, the extinction law after correction by silicon (hypothesis 4.15b).

In red, correction vector  $s$ .

$\ddot{y}$ . c) The empirical extinction law once all the corrections have been made.

#### 4.3.5 Results

Figure 4.15 shows the results obtained. In a) the empirical extinction curve, which if supernovae were standard candles should reflect extinction by dust.

The presence of structures shows the effect on the law deduced from the ignored intrinsic variabilities.

Indeed, they are linked to the structures of the supernova, as shown by the comparison with  $s$  the correction vector

$\ddot{y}$ , which reproduces its appearance remarkably, with the exception of the Ca ii H&K region. As a side note, if we had used  $x_1$  instead of EWSi4131, we would have obtained a very similar vector.

In b), we observe that the extinction law deduced after correction of EWSi4131 is smoother, with the exception of 3 notable structures, two related to the UV and IR calcium regions, and one related to Si ii  $\ddot{y}6355$ . In particular, it is remarkable that in the UV region the curve deviates from a Cardelli law, as seen elsewhere in the color law of SALT2: we show that the origin of this deviation is related to variations in the underlying Ca ii H&K. Thus, the color parameter  $c$  in SALT2 will contain a part that measures the intrinsic dispersions, and a part that comes from the underlying color, which we present in panel c): the latter is remarkably smooth and close to a Cardelli law, despite the fact that we only used the bluest regions to determine our correction.

## CHAPTER 4. ANALYSIS OF SPECTRAL VARIABILITY

---

The coefficient of Cardelli's law measured using synthetic filters gives  $RV = 2.8 \pm 0.3$ , and is compatible with the Galactic value. This measurement opens avenues to understand the discrepancy between the RV value deduced from classical Hubble adjustments, of the order of 2, and the Galactic value: using the dispersion matrix defined in Guy et al. (2010) with a diagonal value of 0.09 mag and a quasi-unitary correlation between bands, we indeed obtain a value of  $RV = 1.9$ . However, this matrix is not representative of ours, with a diagonal value less than or equal to 0.05 magnitudes in B,V,R, and presenting anti-correlations.

This result therefore leads to important conclusions for supernova modeling: on the one hand, we have established the existence of a second intrinsic correction vector, and on the other hand, we have shown that the classically used color law is polluted by the UV variability linked to the Ca ii H&K line. Finally, we explain the origin of the RV outliers obtained using supernovae to determine it as coming from a poor consideration of natural color variations, outside of those taken into account by the model.

## Contributions

The work developed in this chapter is essentially that of Nicolas Chotard's thesis (2011). It has been the subject of a first publication (Chotard et al., 2011), and there is still enough material for a second publication that will systematize the relationships between spectral indicators as much as possible. A comparison between the second correction vector and the predictions of explosion models will also be worthy of publication: we provide a tool that allows for the discrimination of models. Nicolas's postdoctoral position will be ideal for finalizing these publications. Beyond that, there is enough material for a new thesis exploring the relationships between spectra and their spectral indicators outside the luminosity maximum.

I presented the preliminary results of this analysis at an international conference in Moriond (2010) and the published results in Sydney (2011). Nicolas presented them at two international conferences. They were also the subject of a CNRS press release, which was picked up by various press outlets in ways that left me speechless.

# In conclusion

After about ten years since the launch of the SNfactory project, we are able to draw the first conclusions from the statistical analysis of the accumulated data.

While the establishment of a second intrinsic variability factor to be taken into account to standardize objects, as well as the empirical observation at maximum light of a reddening law compatible with extinction by dust of a Galactic nature are important results, there remain a certain number of studies to be carried out.

First, data reduction leaves an unexplained nonlinearity, and its causes need to be investigated. While various nonlinear steps in data reduction are involved, there is one that we need to explore further: the subtraction of the dark current in the R channel of the spectrograph. Indeed, the subtraction residuals, visible for certain exposures in the subtracted cubes, must be reduced. Furthermore, even though we do not have a reliable model for the observed nonlinearity in channel B, responsible for a step on the extracted cubes, it is possible to carry out studies to evaluate its final impact, or to determine whether an imperfect correction would be preferable to no correction. Even at the current state of data reduction, the light curve fitting by SALT2 will have to be improved to take into account the uncertainties related to data calibration.

The observation of relationships between spectral indicators at the maximum is only in its infancy: indeed, even if the observed relationships are generally compatible with those in the literature, it remains to be determined whether the absence of subluminous supernovae in our sample comes from a selection bias, or whether these, as well as other potentially peculiar supernovae, are rejected at the light curve fitting stage by the SALT2 model. The study at higher order dimensions of the relative behavior of indicators must be further investigated. This will be done by taking into account other indicators such as velocities, and by improving the modeling: indeed, we have observed non-linear relationships, which implies that a PCA can only be a first step. It will also be necessary to correct phase effects, which are potentially present in the third eigenvector determined, and to be able to evaluate how many eigenvectors are to be taken into account to best model the object.

Furthermore, a systematic search for criteria to determine which supernovae should be considered special should be undertaken. Indeed, if these supernovae appear normal when considered in their light curves, but they present distinctive spectral characteristics, they are potentially biased if included in cosmological adjustments. Finally, the study of the correlation of spectral properties with host galaxies will likely provide answers concerning the variations already observed in photometry.

The studies shown so far have focused on spectra close to the maximum. It will be necessary to extend them to other phases, which implies redefining some of the indicators to take into account the temporal spectral evolution. The study at other phases will also enrich the reflection on the number of parameters to take into account for modeling

## IN CONCLUSION

---

the variability of objects. It will be especially important to validate or not the color law as a dust law, depending on whether the latter will be invariant or not when changing phase.

One of the questions raised by our work is whether observing a spectrum close to the maximum is sufficient to standardize supernovae. Our preliminary study shows that knowledge of the phase and color determined by SALT2 and EWSi4131 performs as well as a light curve fit. It would be interesting, as an exercise, to determine color and phase directly from the spectra, in order to arrive at an autonomous determination.

Above all, it would be interesting to see if observing a spectrum close to the maximum allows us to determine the spectral shape at other phases, and if not, what would be the minimal set of spectral determinations to take into account to improve the standardization.

Finally, the presence of variability linked to Ca ii H&K raises the question of the standardization of photometrically measured supernovae: indeed, is it possible using only the light curves thus determined to reconstruct what could be a parameter controlling the evolution effects? This is a matter of the observational paradigm: indeed, the future foresees numerous photometric surveys amassing a large quantity of data. In light of our work, will it be possible to standardize them or not without making additional spectroscopic or even spectrophotometric measurements ? It is important to determine this now.

### And what's next?

SNfactory still needs to accumulate supernova data until 2013 using the supernovae found by PTF. Beyond this timescale, what project could we hope for? The presence of evolution effects is one of the systematic sources of uncertainty in the use of supernovae in cosmology that we would like to reduce. We have already determined that the EWCaH&K measurement is a quantity that we would like to compare between low- and medium-redshift data, as an 8m telescope allows a decent signal-to-noise ratio up to  $z = 0.5$ . More generally, it is the spectrophotometric time series that we would like to compare across distances, at least for a modest sample size, to constrain the effects of evolution: indeed, how can we compare the information from 3 to 5 photometric filters with the few dozen pieces of information that can be derived from a spectrum? These data will, however, be difficult to acquire given the competition for access to large telescopes, the complexity of the instruments and data analysis for spectrophotometry, compared to the numerical weakness of the teams involved. I nevertheless believe that in the absence of photometric determinations of the variabilities detected separately at low spectral shifts, such a project would provide a decisive answer regarding the effects of evolution: let us not forget that the measurement of supernovae is dominated by systematic effects.

Finally, it is not possible to imagine the future of the discipline without considering the LSST, a very wide field camera project on a dedicated telescope, which should see its first light after 2018. Such a project will allow us to cover many cosmological probes, and paves a solid path for the future. I hope to be able to involve the LPC, which would pave my way for the years to come, and which will allow me, I hope, to supervise many more students on a fascinating subject.

## **Annexes**



## Appendix A

# Other works

### Summary

---

A.1 NOMAD . . . . .	91
A.1.1 Reconstruction. . . . .	91
A.1.2 Analysis. . . . .	92
A.2 Heavy Ions . . . . .	92
A.2.1 ALICE . . . . .	92
A.2.2 NA60 . . . . .	93
A.3 ToMuVol . . . . .	94

---

### A.1 NOMAD

The NOMAD experiment aimed to search for massive neutrinos by the appearance of  $\bar{\nu}\nu$  in a beam dominated by  $\bar{\nu}\mu$  and for values of square mass difference of interest cosmological: the hypothesis tested was hot dark matter covering 100% of the “mass missing,” as it was called at the time. The experimental apparatus was placed in the Wide Band Beam neutrino beam from the SPS, on the same beamline as the CHORUS experiment, and produces the best world limits in this area of the diagram ( $\Delta m^2$ , mixing angle). The discovery of Super-Kamiokande in 1998 invalidated the hypothesis of searching for oscillations Initially, however, NOMAD remains a benchmark experience in terms of productions inclusive hadronic and knowledge of the neutrino beam.

My contributions to this experience during the 3 years of thesis and the following year of post-doc focused on two aspects, on the one hand the reconstruction of the traces charged in the chambers at derives from experience, and on the other hand the search for oscillations in the decay channel  $\bar{\nu}\nu\rightarrow 3\nu$ .

#### A.1.1 Reconstruction

The signature of neutrino oscillations uses transverse energy as an important variable missing. The reconstruction of this is based on a good reconstruction of the traces in the ‘adrift’ chambers, 0.8 interaction lengths long, which caused numerous secondary interactions. Moreover, these had a very low stereoscopic angle according to the tradition of Saclay, at 5 $\mu$ , which induced a low resolution in the axis parallel to the field magnetic, x. So I developed two algorithms during my thesis, one which used a transition radiation detector that followed the chambers and provided rough drafts

## APPENDIX A. OTHER WORKS

---

of  $x$ -traces to initiate the reconstruction in the chambers. The other algorithm used secondary vertices or traces that had undergone wide-angle scattering as a seed to find traces and fit them between the primary and secondary using a Kalman filter.

### A.1.2 Analysis

The search for the appearance of  $\bar{\nu}$  neutrinos in the experiment was divided into as many channels as there are decay pathways of  $\bar{\nu}$ . I focused on the decay channel  $\bar{\nu} \bar{\nu} 3$  charged, which provides a strong internal constraint related to the internal structure of the 3 charged. Compared to the simplistic analysis of the experimental proposal, which was based solely on the analysis of the pulses in the plane transverse to the beam, Pierre Astier and I introduced a discriminant variable analysis, which took into account the structure of the decay into three charged waves, as well as an isolation variable between the decay residues of the  $\bar{\nu}$  and the hadrons coming from the charged current. This discriminant variable, or isolation pT, was taken up by the other analyses of the collaboration in all the usable decay channels of the  $\bar{\nu}$ . Finally, as we were looking for rejection rates of the order of 106, I conducted one of the first blind analyses of the collaboration on the preliminary data from 1995 and 1996, and demonstrated the importance of this approach. The work on the rejection of unwanted events also highlighted a number of flaws in the simulation, whether the transverse dispersion in pT of the hadronic jets, the fragmentation parameters which simulated jets that were too hard, and the Fermi momentum phenomena in the neutrino target nucleus which induced a simulated transverse momentum too weak for the  $\bar{\nu}$ . This led to the development of a simulator from the data itself, for example by replacing the  $\mu$  produced by a  $\bar{\nu}$  and simulating only the decay of the latter, or by removing it to simulate neutral currents.

## Contributions

The NOMAD experiment has produced 27 scientific articles of which I am a signatory, among which 4 either allow to deepen the few lines above, or reflect to varying degrees my involvement. [Altegoer et al. \(1998a\)](#) and [Anfreville et al. \(2002\)](#) describe respectively the detector and the drift chambers, while [Altegoer et al. \(1998b\)](#) and [Astier et al. \(1999\)](#) describe the first results of the search for the appearance of  $\bar{\nu}\bar{\nu}$ . I presented the preliminary results of the experiment at an international conference in Moriond (1999), and at the occasion of 4 laboratory seminars.

## A.2 Heavy Ions

### A.2.1 ALICE

The ALICE experiment, placed on the LHC beam at CERN, aims to probe the appearance of a quark-gluon plasma in nucleus-nucleus interactions at 5.5 TeV per pair of nuclei, and the sub-detectors that compose it are optimized to detect its signatures.

The Lyon group, having had the expertise of the NA38 and NA50 experiments, naturally engaged in the R&D of the di-muon arm, in order to observe the high-energy and forward signatures.

The design the group was involved in concerned prototype chambers intended to fit inside the dipole magnet, and read by segmented cathodes. They were modeled on the design of the chambers made at IPNO, but with a different segmentation and, above all, a

---

A.2. HEAVY IONS

parallel reading of cathode segments in order to reduce the number of high-radius electronic channels, where the occupancy rate was lower. I participated in the test beam campaigns of these chambers, and improved the position reconstruction by taking into account the capacitive effects between tracks. I also highlighted a phenomenon described by [Charpak et al. \(1979\)](#) allowing to improve by a factor of 2.5 the resolution in the coordinate transverse to the reading wires compared to the traditional interwire/ $\bar{y}$  12.

In parallel with the chamber R&D activities, I focused on the simulation and reconstruction software for the di-muon arm. Among other tasks, I modeled the third chamber, and wrote the algorithm for reconstructing the clusters left by the stacks of charged traces, which allowed in this chamber to resolve multi-charged ambiguities with 97% efficiency.

### A.2.2 NA60

The opportunity to participate in a relay experiment before the start of the LHC arose in Lyon, with two alternatives: one to participate in the PHENIX experiment, which did not see the light of day, and the other to propose a follow-up to the NA50 program, in the form of a new experiment, NA60.

NA50 consisted mainly of a muon spectrometer to record dimuon events caused by the interaction of an ion beam on a fixed target, and provided a signal of abnormal  $J/\psi$  disappearance. The interest in studying this phenomenon with other pairs of nuclei to probe the relevant variable and if possible discriminate the models quickly became apparent, as did the need for a modification of the equipment: it was a question of adding a pixel telescope immersed in a dipolar magnetic field upstream of the hadron absorber, which should make it possible to significantly improve the resolution of the spectrometer for small masses, to increase the acceptance at low transverse momentum, and to label the charm by measuring the displaced vertex. With these improvements, the goals were to test the excess events seen by CERES at low masses, to measure the contribution of open charm to the excess events observed by NA50, and to separate the  $J/\psi$  resonances from the  $\psi$  of the pixels. As for the software architecture, this project presented many synergies with the ALICE project. Three French laboratories participated: IPNL, LPC and LLR. Both by the choice of technology

I participated in the experiment proposal, my expertise being the evaluation of the required software efforts, and the development of a simulation and analysis software prototype. To do this, I used the architecture developed in aliroot, the ALICE framework, to recycle most of the software and test it in real conditions well before the start of the LHC. More specifically, on the NA60 part, I wrote the reconstruction of the traces in the silicon pixels.

## Contributions

I am a signatory to 10 of the ALICE TDRs (Technical Design Reports), my work being reflected in the work on the di-muon arm ([Dellacasa et al., 1999](#)), and I contributed to the proposal of NA60 ([Baldit et al., 2000b,a](#)). I also contributed significantly to IPNL's involvement in this project, which allowed two theses on ALICE to have science data to analyze, including that of Philippe Pillot, provided the material for Laurent Ducroux's HDR, and ultimately led to numerous publications.

The work on heavy ions allowed me to supervise two students, Stéphane Ranchon in L3 and Nathalie Pargenthalian in M2, and was popularized during a public conference.

---

**APPENDIX A. OTHER WORKS****A.3 ToMuVol**

I joined a valorization project since the end of 2009 for about 20% of my time: the ToMuVol project, which allows me to be part of the LPC dynamics, while maintaining control of my main activity. This project aims to transfer technology to volcanology of particle physics detectors, as well as knowledge of cosmic muon fluxes developed within the framework of ANTARES. The detectors selected for the prototype are RPCs developed within the framework of the CALICE collaboration, and available at relatively low cost for testing.

The principle consists of measuring the absorption of cosmic muons through a volcanic edifice in order to determine the average density along the trajectory. A first Japanese study showed that it was possible to be sensitive to density contrasts lower than one percent. However, the resolution of their equipment is not sufficient to obtain precise structures, and their choice of using emulsions does not allow real-time data processing.

In collaboration with volcanologists from the Magma and Volcanoes Laboratory, specialists in in situ deployment and final recipients of the transfer, we deployed RPCs developed in Lyon at a site near Puy de Dôme, and we have been collecting data since January 2010. Once the method has been validated, it can then be transferred to other structures in order to either monitor active volcanoes or reconstruct structures using tomography using different viewing angles.

## Other contributions

**In my opinion, research work cannot be conceived without participating in the life of institutions. While I have attempted throughout this document to contextualize most of my work, some activities are by nature unclassifiable in this or that category linked to a scientific development per se.**

This is also the case with teaching: we owe it to the institution that trained us to become trainers in our turn, which also offers the researcher the advantage of getting involved in the life of the university to which their UMR belongs, and incidentally of knowing the students, a significant advantage when it comes to taking on interns. I taught from 1995 to 2004, for about 30 hours on average per year, from L1 to M1, first as a tutor, then as part of a teaching exchange program set up by the UCBL Physics Department.

The other contribution I would like to mention is more directly linked to the CNRS: from 2004 to 2008, I was secretary of section 03 of the CoNRS and a member of CID 47. By devoting a significant part of my time to serving the community, I hope to have done useful work. At least for me, it was a source of certain enrichment.

**APPENDIX A. OTHER WORKS**

---

# Table of figures

<b>2.1 Position of supernovae in the sky.</b>	<b>20</b>
<b>2.2 Comparison of the sample with other sources.</b>	<b>21</b>
<b>2.3 Distribution of supernovae in phase and in z.</b>	<b>22</b>
<b>2.4 Optical diagram of the SNIFS instrument.</b>	<b>23</b>
<b>2.5 Diagram of the photometric channel.</b>	<b>24</b>
<b>2.6 Projection of spectra onto CCDs.</b>	<b>26</b>
<b>2.7 Histogram of pixel values.</b>	<b>28</b>
<b>2.8 Stray light.</b>	<b>29</b>
<b>2.9 Data Cube.</b>	<b>30</b>
<b>2.10 First attempts at PSF extraction.</b>	<b>31</b>
<b>2.11 Extracting PSF.</b>	<b>32</b>
<b>2.12 Atmosphere correction.</b>	<b>34</b>
<b>2.13 Photometric ratios.</b>	<b>35</b>
<b>2.14 Modeling the underlying galaxy.</b>	<b>35</b>
<b>2.15 Spectral time series of SNF20080522-000.</b>	<b>36</b>
<b>2.16 Light curve of SNF20080522-000.</b>	<b>37</b>
<b>2.17 Hubble diagram of SNfactory.</b>	<b>38</b>
<b>3.1 Diagram of the various zones of a CCD.</b>	<b>42</b>
<b>3.2 Transmission of the two instrument channels.</b>	<b>43</b>
<b>3.3 Schematic diagram of the test bench at IPNL.</b>	<b>44</b>
<b>3.4 Pixel values depending on the start of playback.</b>	<b>45</b>
<b>3.5 Reading noise</b>	<b>46</b>
<b>3.6 Measure used to reconstruct the structure of the spectral variance</b>	<b>49</b>
<b>3.7 CCD faults for R and B channels.</b>	<b>50</b>
<b>3.8 Effect of hot pixels on the R channel.</b>	<b>52</b>
<b>3.9 Delayed Charge Fractions for Serial and Parallel Registers.</b>	<b>53</b>
<b>3.10 Bias structure.</b>	<b>54</b>
<b>3.11 The dark current model.</b>	<b>56</b>
<b>3.12 Map of pixel-to-pixel variations of bias and dark.</b>	<b>57</b>
<b>3.13 Differences in dark currents between the two amplifiers of the same channel.</b>	<b>58</b>
<b>3.14 Photometric flat field exposures.</b>	<b>59</b>
<b>3.15 Extract from a flat field of CCD B.</b>	<b>60</b>
<b>3.16 Spectra of CONTINUOUS poses.</b>	<b>60</b>
<b>3.17 Average profile of cosmic rays on channels B and R.</b>	<b>62</b>
<b>3.18 Comparison of DOME data at long and short exposure times.</b>	<b>63</b>
<b>3.19 Measurement of nonlinearity under controlled conditions.</b>	<b>64</b>

**TABLE OF FIGURES**

---

4.1 Spectral structures observed at the maximum. . . . .	68
4.2 Definition of various types of spectral indicators. . . . .	69
4.3 Savitzky-Golay approximation for Ca ii H&K and Si ii $\lambda$ 4131. . . . .	70
4.4 Comparison of silicon lines and SALT2 parameters. . . . .	72
4.5 Relationships between the various equivalent widths of Silicon. . . . .	73
4.6 Evolution of the speed of Si ii $\lambda$ 6355. . . . .	73
4.7 Variability of the calcium zone. . . . .	74
4.8 Correlations between calcium, silicon and SALT2 parameters. . . . .	75
4.9 The first three eigenvectors. . . . .	78
4.10 Spectrum after color correction. . . . .	79
4.11 Interpolation of magnitudes in synthetic filters. . . . .	81
4.12 Evolution of the magnitude measured in B with EWSi4131. . . . .	82
4.13 Relationship between $\lambda$ AU and $\lambda$ AV after correction by EWSi4131 . . . . .	83
4.14 Monte Carlo study of the dispersion matrix. . . . .	84
4.15 Empirical extinction laws and correction vectors $s\lambda$ under different assumptions. . . . .	85

## List of tables

<b>2.1 Sample of supernovae...</b>	<b>21</b>
<b>2.2 Data quality.....</b>	<b>37</b>
<b>3.1 Expected and observed values for the nonlinearity parameters.....</b>	<b>64</b>
<b>4.1 Correlations between line widths and supernova parameters.....</b>	<b>76</b>
<b>4.2 Principal component study of equivalent depths.....</b>	<b>77</b>

**LIST OF TABLES**

---

# Bibliography

- Aldering, G. et al. 2002, "Overview of the Nearby Supernova Factory," in Society of Photo-Optical Instrumentation Engineers (SPIE) Conference Series, Society of Photo-Optical Instrumentation Engineers (SPIE) Conference Series, vol. 4836, edited by JA Tyson & S. Wolff, p. 61–72, doi:10.1117/12.458107. [18](#), [39](#)
- Aldering, G. et al. 2006, "Nearby Supernova Factory Observations of SN 2005gj: Another Type Ia Supernova in a Massive Circumstellar Envelope", ApJ, vol. 650, doi:10.1086/507020, p. 510–527. [10](#), [15](#)
- Altegoer, J. et al. 1998a, "The NOMAD experiment at the CERN SPS", Nuclear Instruments and Methods in Physics Research A, vol. 404, doi:10.1016/S0168-9002(97)01079-6, p. 96–128. [92](#)
- Altegoer, J. et al. 1998b, "A search for  $\bar{\mu}$   $\bar{\nu}$   $\bar{\mu}$   $\bar{\nu}$  oscillations using the NOMAD detector", Physics Letters B, vol. 431, doi:10.1016/S0370-2693(98)00521-8, p. 219–236. [92](#)
- Anfreville, M. et al. 2002, "The drift chambers of the NOMAD experiment", Nuclear Instruments and Methods in Physics Research A, vol. 481, doi:10.1016/S0168-9002(01)01371-7, p. 339–343. [92](#)
- Antilogus, P. et al. 2008, "Data taking in Virtual Control Room: the SNfactory example," in Society of Photo-Optical Instrumentation Engineers (SPIE) Conference Series, Society of Photo-Optical Instrumentation Engineers (SPIE) Conference Series, vol. 7016, p. 70 161L–, doi:10.1117/12.789433. [27](#), [39](#)
- Arnett, WD 1982, "Type I supernovae. I - Analytic solutions for the early part of the light curve", ApJ, vol. 253, doi:10.1086/159681, p. 785–797. [10](#)
- Arsenijevic, V. et al. 2008, "Diversity of supernovae Ia determined using equivalent widths of Si II 4000", A&A, vol. 492, doi:10.1051/0004-6361:200810675, p. 535–544. [19](#), [71](#)
- Astier, P. et al. 1999, "A more sensitive search for  $\bar{\mu}\mu$   $\bar{\nu}\nu$   $\bar{\mu}\mu$   $\bar{\nu}\nu$  oscillations in NOMAD", Physics Letters B, vol. 453, doi:10.1016/S0370-2693(99)00303-2, p. 169–186. [92](#)
- Astier, P. et al. 2006, "The Supernova Legacy Survey: measurement of  $\bar{M}$ ,  $\bar{\Lambda}$  and  $w$  from the first year data set", A&A, vol. 447, doi:10.1051/0004-6361:20054185, p. 31–48. [17](#)
- Bailey, S. et al. 2009, "Using spectral flux ratios to standardize SN Ia luminosities", A&A, vol. 500, doi:10.1051/0004-6361/200911973, p. L17–L20. [15](#), [71](#)
- Bailey, S. et al. 2007, "How to Find More Supernovae with Less Work: Object Classification Techniques for Difference Imaging", ApJ, vol. 665, doi:10.1086/519832, p. 1246–1253. [20](#)

## BIBLIOGRAPHY

---

- Baldit, A. et al. 2000a, "Further information concerning P316", CERN-SPSC-2000-025. **93**
- Baldit, A. et al. 2000b, "Study of prompt dimuon and charm production with proton and heavy ion beams at the CERN SPS", CERN-SPSC-2000-010. **93**
- Baltay, C. et al. 2007, "The QUEST Large Area CCD Camera", PASP, vol. 119, doi: 10.1086/523899, p. 1278–1294. **20**
- Benedict, GF et al. 2002, "Astrometry with the Hubble Space Telescope: A Parallax of the Fundamental Distance Calibrator RR Lyrae", AJ, vol. 123, doi:10.1086/338087, p. 473–484. **6**
- Benetti, S. et al. 2005, "The Diversity of Type Ia Supernovae: Evidence for Systematics ?" ApJ, vol. 623, doi:10.1086/428608, p. 1011–1016. **10**
- Blanc, N. 2006, Extraction of standard stars for flux calibration of the SNIFS instrument in the Nearby Supernova Factory experiment, doctoral thesis, Claude Bernard University - Lyon I. **30**, **31**, **54**
- Blondin, S., KS Mandel and RP Kirshner. 2011, "Do spectra distance measurements of Type Ia supernovae ?", A&A, vol. 526, doi:10.1051/0004-6361/201015792, p. A81–+. **71**
- Bloom, JS, DA Frail, and SR Kulkarni. 2003, "Gamma-Ray Burst Energetics and the Gamma- Ray Burst Hubble Diagram: Promises and Limitations", ApJ, vol. 594, doi:10.1086/377125, p. 674– 683. **5**
- Bohlin, RC 2007, "HST Stellar Standards with 1% Accuracy in Absolute Flux", in The Future of Photometric, Spectrophotometric and Polarimetric Standardization, Astronomical Society of the Pacific Conference Series, vol. 364, edited by C. Sterken, p. 315–+. **27**
- Bongard, S. 2005, Radiative transfer and spectral study of SNels in the context of Supernovae factory, doctoral thesis, University of Lyon-I. **67**
- Bongard, S. et al. 2006, "Type Ia Supernova Spectral Line Ratios as Luminosity Indicators", ApJ, vol. 647, doi:10.1086/505322, p. 513–524. **74**
- Branch, D., LC Dang, and E. Baron. 2009, "Comparative Direct Analysis of Type Ia Supernova Spectra. V. Insights from a Larger Sample and Quantitative Subclassification," PASP, vol. 121, doi:10.1086/597788, p. 238–247. **14.71**
- Branch, D. et al. 2006, "Comparative Direct Analysis of Type Ia Supernova Spectra. II. Maximum Light," PASP, vol. 118, doi:10.1086/502778, p. 560–571. **10, 71, 72**
- Branch, D. et al. 1995, "In Search of the Progenitors of Type IA Supernovae", PASP, vol. 107, doi:10.1086/133657, p. 1019–+. **9**
- Brandt, TD et al. 2010, "The Ages of Type Ia Supernova Progenitors", AJ, vol. 140, doi:10.1088/0004-6256/140/3/804, p. 804–816. **11**
- Bronder, TJ et al. 2008, "SNLS spectroscopy: testing for evolution in type Ia supernovae", A&A, vol. 477, doi:10.1051/0004-6361:20077655, p. 717–734. **71**
- Buchert, T. 2008, "Dark Energy from structure: a status report", General Relativity and Gravitation, vol. 40, doi:10.1007/s10714-007-0554-8, p. 467–527. **8**

---

BIBLIOGRAPHY

---

- Buton, C.** 2009, Spectrophotometric calibration of the SuperNova Integral Field Spectrograph in the framework of the Nearby Supernova Factory project, doctoral thesis, Claude Bernard University - Lyon I. **33**
- Cardelli, JA, GC Clayton and JS Mathis.** 1989, “The relationship between infrared, optical, and ultraviolet extinction”, *ApJ*, vol. 345, doi:10.1086/167900, p. 245–256. **5, 14, 80**
- Cavadore, C. and RJ Dorn.** 1999, “Charge coupled devices at ESO - Performances and results”, in *Optical Detectors for Astronomy II: State-of-the-Art at the Turn of the Millennium. 4th ESO CCD Workshop*, held in Garching, Germany, edited by Paola Amico and James W. Beletic, Kluwer Academic Publishers, PO Box 17, 3300 AA Dordrecht, p. 25. **42**
- Charpak, G. et al.** 1979, “High-accuracy localization of minimum ionizing particles using the cathode-induced charge center-of-gravity read-out”, *Nuclear Instruments and Methods*, vol. 167, doi:10.1016/0029-554X(79)90227-1, p. 455–464. **93**
- Childress, M. et al.** 2011, “Keck Observations of the Young Metal-poor Host Galaxy of the Super-Chandrasekhar-mass Type Ia Supernova SN 2007if”, *ApJ*, vol. 733, doi:10.1088/0004-637X/733/1/3, p. 3–+. **15**
- Chotard, N.** 2011, Scientific analysis of data from The Nearby Supernova Factory collaboration , doctoral thesis, Université Claude Bernard - Lyon I. **19, 50, 76, 79, 86**
- Chotard, N. et al.** 2011, “The reddening law of type Ia supernovae: separating intrinsic variability from dust using equivalent widths”, *A&A*, vol. 529, doi:10.1051/0004-6361/201116723, p. L4–+. **15, 16, 19, 67, 79, 86**
- Conley, A. et al.** 2008, “SiFTO: An Empirical Method for Fitting SN Ia Light Curves”, *ApJ*, vol. 681, doi:10.1086/588518, p. 482–498. **14**
- Copeland, EJ, M. Sami, and S. Tsujikawa.** 2006, “Dynamics of Dark Energy”, *International Journal of Modern Physics D*, vol. 15, doi:10.1142/S021827180600942X, p. 1753–1935. **7**
- Copin, Y.** 2000, Dynamics of Early-Type Galaxies: 3D Observations and Modeling, doctoral thesis, Claude Bernard University (Lyon I). **30**
- Copin, Y. et al.** 2006, “The Nearby Supernova Factory”, *New Astron. Rev.*, vol. 50, doi:10.1016/j.newar.2006.02.035, p. 436–438. **39**
- Courtois, HM et al.** 2011, “Cosmic Flows: Green Bank Telescope and Parkes HI observations”, *MNRAS*, doi:10.1111/j.1365-2966.2011.18515.x, p. 466–+. **6**
- Dellacasa, G. et al.** 1999, “ALICE technical design report of the dimuon forward spectrometer”, CERN-LHCC- **99-22.93**
- Dunkley, J. et al.** 2009, “Five-Year Wilkinson Microwave Anisotropy Probe Observations: Likelihoods and Parameters from the WMAP Data”, *ApJS*, vol. 180, doi:10.1088/0067-0049/180/2/306, p. 306–329. **6**
- Ellis, RS et al.** 2008, “Verifying the Cosmological Utility of Type Ia Supernovae: Implications of a Dispersion in the Ultraviolet Spectra”, *ApJ*, vol. 674, doi:10.1086/524981, p. 51–69. **74**

## BIBLIOGRAPHY

---

- Fakhouri, H. et al. 2011, "Twin Supernova Studies with SNe Ia from SNfactory," in American Astronomical Society Meeting Abstracts #217, Bulletin of the American Astronomical Society, vol. 43, p. 337.13+. **19**
- Freedman, WL and BF Madore. 2010, "The Hubble Constant," ARA&A, vol. 48, doi: 10.1146/annurev-astro-082708-101829, p. 673–710. **4**
- Freedman, WL et al. 2001, "Final Results from the Hubble Space Telescope Key Project to Measure the Hubble Constant", ApJ, vol. 553, doi:10.1086/320638, p. 47–72. **4**
- Frieman, JA et al. 2008, "The Sloan Digital Sky Survey-II Supernova Survey: Technical Summary", AJ, vol. 135, doi:10.1088/0004-6256/135/1/338, p. 338–347. **17**
- Gilfanov, M. and A. Bogdan. 2010, "An upper limit on the contribution of accreting white dwarfs to the type Ia supernova rate", Nature, vol. 463, doi:10.1038/nature08685, p. 924–925. **10**
- Goobar, A. 2008, "Low RV from Circumstellar Dust around Supernovae", ApJ, vol. 686, doi: 10.1086/593060, p. L103–L106. **15**
- Guy, J. et al. 2007, "SALT2: using distant supernovae to improve the use of type Ia supernovae as distance indicators", A&A, vol. 466, doi:10.1051/0004-6361:20066930, p. 11–21. **13, 36, 7**
- Guy, J. et al. 2010, "The Supernova Legacy Survey 3-year sample: Type Ia supernovae photometric distances and cosmological constraints", A&A, vol. 523, doi:10.1051/0004-6361/ 201014468, p. A7–+. **15, 17, 83, 86**
- Hachinger, S., PA Mazzali and S. Benetti. 2006, "Exploring the spectroscopic diversity of Type Ia supernovae", MNRAS, vol. 370, doi:10.1111/j.1365-2966.2006.10468.x, p. 299–318. **72**
- Hachisu, I., M. Kato, and K. Nomoto. 2010, "Supersoft X-ray Phase of Single Degenerate Type Ia Supernova Progenitors in Early-type Galaxies", ApJ, vol. 724, doi:10.1088/2041-8205/724/2/ L212, p. L212–L216. **10**
- Heath, ST 1913, Aristarchus of Samos, the ancient Copernicus; a history of Greek astronomy to Aristarchus, together with Aristarchus's Treatise on the sizes and distances of the sun and moon: a new Greek text with translation and notes., London: Oxford University Press. **3**
- Hicken, M. et al. 2009a, "CfA3: 185 Type Ia Supernova Light Curves from the CfA", ApJ, vol. 700, doi:10.1088/0004-637X/700/1/331, p. 331–357. **17, 20**
- Hicken, M. et al. 2009b, "Improved Dark Energy Constraints from ~100 New CfA Supernova Type Ia Light Curves", ApJ, vol. 700, doi:10.1088/0004-637X/700/2/1097, p. 1097–1140. **14**
- Hoeflich, P., JC Wheeler and FK Thielemann. 1998, "Type IA Supernovae: Influence of the Initial Composition on the Nucleosynthesis, Light Curves, and Spectra and Consequences for the Determination of Omega M and Lambda", ApJ, vol. 495, doi:10.1086/305327, p. 617–+. **74**
- Howell, DA et al. 2009, "The Effect of Progenitor Age and Metallicity on Luminosity and 56Ni Yield in Type Ia Supernovae", ApJ, vol. 691, doi:10.1088/0004-637X/691/1/661, p. 661–671. **10, 12**
- Howell, SB 2000, Handbook of CCD Astronomy, Cambridge Observing Handbooks for Research Astronomers, Cambridge University Press. **42**

---

BIBLIOGRAPHY

---

- Hoyle, F. and W. A. Fowler. 1960, "Nucleosynthesis in Supernovae.", *ApJ*, vol. 132, doi:10.1086/146963, p. 565–+. 9
- Humphreys, EML et al. 2008, "Toward a New Geometric Distance to the Active Galaxy NGC 4258. II. Centripetal Accelerations and Investigation of Spiral Structure," *ApJ*, vol. 672, doi:10.1086/523637, p. 800–816. 6
- Iben, I., Jr. and AV Tutukov. 1984, "Supernovae of type I as end products of the evolution of binaries with components of moderate initial mass ( $M$  not greater than about 9 solar masses)", *ApJS*, vol. 54, doi:10.1086/190932, p. 335–372. 9
- Ihara, Y. et al. 2007, "Searching for a Companion Star of Tycho's Type Ia Supernova with Optical Spectroscopic Observations", *PASJ*, vol. 59, p. 811–826. 11
- Jha, S., AG Riess and RP Kirshner. 2007, "Improved Distances to Type Ia Supernovae with Multicolor Light-Curve Shapes: MLCS2k2", *ApJ*, vol. 659, doi:10.1086/512054, p. 122–148. 13
- Kasen, D., FK Röpke and SE Woosley. 2009, "The diversity of type Ia supernovae from broken symmetries", *Nature*, vol. 460, doi:10.1038/nature08256, p. 869–872. 12
- Kerschhagi, M. et al. 2011, "Cosmology with the Nearby Supernova Factory", *Progress in Particle and Nuclear Physics*, vol. 66, doi:10.1016/j.ppnp.2011.01.030, p. 335–339. 15
- Kessler, R. et al. 2009, "First-Year Sloan Digital Sky Survey-II Supernova Results: Hubble Diagram and Cosmological Parameters", *ApJS*, vol. 185, doi:10.1088/0067-0049/185/1/32, p. 32–84. 17.74
- Khokhlov, AM 1991, 'Delayed detonation model for type IA supernovae', *A&A*, vol. 245, p. 114–128. 12
- Komatsu, E. et al. 2009, "Five-Year Wilkinson Microwave Anisotropy Probe Observations: Cosmological Interpretation", *ApJS*, vol. 180, doi:10.1088/0067-0049/180/2/330, p. 330–376. 4, 6, 7
- Kotak, R. 2008, "Progenitors of Type Ia Supernovae", in RS Ophiuchi (2006) and the Recurrent Nova Phenomenon, *Astronomical Society of the Pacific Conference Series*, vol. 401, edited by A. Evans, MF Bode, TJ O'Brien, & MJ Darnley, p. 150–+. 9
- Kromer, M. et al. 2010, "Double-detonation Sub-Chandrasekhar Supernovae: Synthetic Observables for Minimum Helium Shell Mass Models", *ApJ*, vol. 719, doi:10.1088/0004-637X/719/2/1067, p. 1067–1082. 13
- Lampeitl, H. et al. 2010, "The Effect of Host Galaxies on Type Ia Supernovae in the SDSS-II Supernova Survey", *ApJ*, vol. 722, doi:10.1088/0004-637X/722/1/566, p. 566–576. 11
- Lantz, B. et al. 2004, "SNIFS: a wideband integral field spectrograph with microlens arrays," in Society of Photo-Optical Instrumentation Engineers (SPIE) Conference Series, *Society of Photo-Optical Instrumentation Engineers (SPIE) Conference Series*, vol. 5249, edited by L. Mazuray, PJ Rogers, & R. Wartmann, p. 146–155, doi:10.1117/12.512493. 22, 39
- Law, N.M. et al. 2009, "The Palomar Transient Factory: System Overview, Performance, and First Results", *PASP*, vol. 121, doi:10.1086/648598, p. 1395–1408. 18

## BIBLIOGRAPHY

---

- Lee, MG, WL Freedman and BF Madore. 1993, "The Tip of the Red Giant Branch as a Distance Indicator for Resolved Galaxies", *ApJ*, vol. 417, doi:10.1086/173334, p. 553–+. 4
- Lentz, EJ et al. 2000, "Metallicity Effects in Non-LTE Model Atmospheres of Type IA Supernovae", *ApJ*, vol. 530, doi:10.1086/308400, p. 966–976. 74
- Li, W. et al. 2003, "SN 2002cx: The Most Peculiar Known Type Ia Supernova", *PASP*, vol. 115, doi:10.1086/374200, p. 453–473. 10
- Linde, AD 1983, "Chaotic inflation", *Physics Letters B*, vol. 129, doi:10.1016/0370-2693(83)90837-7, p. 177–181. 4
- Linder, EV 2006, "Importance of supernovae at  $z < 0.1$  for probing dark energy", *Phys. Rev. D*, flight. 74, no. 10, doi:10.1103/PhysRevD.74.103518, p. 103,518–+. 18
- Madore, BF and WL Freedman. 1991, "The Cepheid distance scale", *PASP*, vol. 103, doi:10.1086/132911, p. 933–957. 4, 5
- Maeda, K. et al. 2010, "An asymmetric explosion as the origin of spectral evolution diversity in type Ia supernovae", *Nature*, vol. 466, doi:10.1038/nature09122, p. 82–85. 13
- Maoz, D. and F. Mannucci. 2008, "A search for the progenitors of two Type Ia Supernovae in NGC 1316", *MNRAS*, vol. 388, doi:10.1111/j.1365-2966.2008.13403.x, p. 421–428. 11
- Maoz, D., K. Sharon and A. Gal-Yam. 2010, "The Supernova Delay Time Distribution in Galaxy Clusters and Implications for Type-Ia Progenitors and Metal Enrichment", *ApJ*, vol. 722, doi:10.1088/0004-637X/722/2/1879, p. 1879–1894. 11
- Marietta, E., A. Burrows and B. Fryxell. 2000, "Type Ia Supernova Explosions in Binary Systems: The Impact on the Secondary Star and Its Consequences", *ApJS*, vol. 128, doi:10.1086/313392, p. 615–650. 11
- McLean, I. 1997, *Electronic Imaging in Astronomy: Detectors and Instrumentation, Wiley-Praxis Series in Astronomy & Astrophysics*, Praxis Publishing. 42
- Napiwotzki, R. et al. 2004, "Double degenerates and progenitors of supernovae type Ia", in *Spectroscopically and Spatially Resolving the Components of the Close Binary Stars, Astronomical Society of the Pacific Conference Series*, vol. 318, edited by RW Hilditch, H. Hensberge, & K. Pavlovski, p. 402–410. 11
- Nomoto, K., F.-K. Thielemann and K. Yokoi. 1984, "Accreting white dwarf models of Type I supernovae. III - Carbon deflagration supernovae", *ApJ*, vol. 286, doi:10.1086/162639, p. 644–658. 12
- Nugent, P. et al. 1995, "Evidence for a Spectroscopic Sequence among Type Ia Supernovae", *ApJ*, vol. 455, doi:10.1086/309846, p. L147–+. 19, 67, 74
- O'Donnell, JE 1994, 'Ry-dependent optical and near-ultraviolet extinction', *ApJ*, vol. 422, doi:10.1086/173713, p. 158–163. 80
- Patat, F. et al. 2007, "Detection of Circumstellar Material in a Normal Type Ia Supernova", *Science*, vol. 317, doi:10.1126/science.1143005, p. 924–. 10

---

BIBLIOGRAPHY

- Percival, WJ et al. 2010, "Baryon acoustic oscillations in the Sloan Digital Sky Survey Data Release 7 galaxy sample", MNRAS, vol. 401, doi:10.1111/j.1365-2966.2009.15812.x, p. 2148–2168. **4**
- Pereira, R. 2008, **Nearby Supernova Factory: Calibration of SNIFS data and spectrophotometric light curves of type supernovae**, doctoral thesis, Université Paris- Diderot - Paris VII. **25, 33, 58**
- Perlmutter, S. et al. 1999, "Measurements of Omega and Lambda from 42 High-Redshift Supernovae", ApJ, vol. 517, doi:10.1086/307221, p. 565–586. **7**
- Perryman, MAC et al. 2001, "GAIA: Composition, formation and evolution of the Galaxy", A&A, vol. 369, doi:10.1051/0004-6361:20010085, p. 339–363. **4**
- Perryman, MAC et al. 1997, "The HIPPARCOS Catalogue", A&A, vol. 323, p. L49–L52. **4**
- Poon, S. et al. 2008, "Context-Linked Virtual Assistants for Distributed Teams: An Astrophysics Case Study," in CSCW 2008: ACM Conference on Computer Supported Cooperative Work. **27**
- Riess, AG et al. 1998, "Observational Evidence from Supernovae for an Accelerating Universe and a Cosmological Constant", AJ, vol. 116, doi:10.1086/300499, p. 1009–1038. **7**
- Riess, AG et al. 2011, "A 3% Solution: Determination of the Hubble Constant with the Hubble Space Telescope and Wide Field Camera 3", ApJ, vol. 730, doi:10.1088/0004-637X/730/2/119, p. 119–+. **6**
- Rizzi, L. et al. 2007, "Tip of the Red Giant Branch Distances. II. Zero-Point Calibration," ApJ, vol. 661, doi:10.1086/516566, p. 815–829. **4**
- Röpke, FK et al. 2011, "Modeling Type Ia supernova explosions", Progress in Particle and Nuclear Physics, vol. 66, doi:10.1016/j.ppnp.2011.01.026, p. 309–318. **12**
- Ruiz-Lapuente, P. et al. 2004, "The binary progenitor of Tycho Brahe's 1572 supernova", Nature, vol. 431, doi:10.1038/nature03006, p. 1069–1072. **11**
- Sandage, A. et al. 2006, "The Hubble Constant: A Summary of the Hubble Space Telescope Program for the Luminosity Calibration of Type Ia Supernovae by Means of Cepheids", ApJ, vol. 653, doi:10.1086/508853, p. 843–860. **5**
- Scalzo, RA et al. 2010, "Nearby Supernova Factory Observations of SN 2007if: First Total Mass Measurement of a Super-Chandrasekhar-Mass Progenitor", ApJ, vol. 713, doi: 10.1088/0004-637X/713/2/1073, p. 1073–1094. **10, 15**
- Schmidt, BP, RP Kirshner, and RG Eastman. 1992, "Expanding photospheres of type II supernovae and the extragalactic distance scale", ApJ, vol. 395, doi:10.1086/171659, p. 366–386. **5**
- Sim, SA et al. 2010, "Detonations in Sub-Chandrasekhar-mass C+O White Dwarfs", ApJ, vol. 714, doi:10.1088/2041-8205/714/1/L52, p. L52–L57. **12**
- Sorensen, A. 2000, "MAT/EEV CCD 44-82", research notebook, ESO. **42**

## BIBLIOGRAPHY

---

- Sotiriou, TP and V. Faraoni.** 2010, “f(R) theories of gravity”, *Reviews of Modern Physics*, vol. 82, doi:10.1103/RevModPhys.82.451, p. 451–497. [8](#)
- Stritzinger, M. et al.** 2006, “Consistent estimates of 56Ni yields for type Ia supernovae”, *A&A*, flight. 460, doi:10.1051/0004-6361:20065514, p. 793–798. [10](#)
- Sullivan, M. et al.** 2010, “The dependence of Type Ia Supernovae luminosities on their host galaxies”, *MNRAS*, vol. 406, doi:10.1111/j.1365-2966.2010.16731.x, p. 782–802. [11](#)
- Thomas, RC et al.** 2007, “Nearby Supernova Factory Observations of SN 2006D: On Sporadic Carbon Signatures in Early Type Ia Supernova Spectra”, *ApJ*, vol. 654, doi:10.1086/510780, p. L53–L56. [15](#)
- Timmes, FX, EF Brown and JW Truran.** 2003, “On Variations in the Peak Luminosity of Type Ia Supernovae”, *ApJ*, vol. 590, doi:10.1086/376721, p. L83–L86. [12](#)
- Tully, R.B. and J.R. Fisher.** 1977, “A new method of determining distances to galaxies”, *A&A*, vol. 54, p. 661–673. [6](#)
- USNO, HMNAO and UKHO.** 2011, *The Astronomical Almanac for the year 2011*, US Government Printing Office, Washington, and the UK Hydrographic Office. [4](#)
- van Leeuwen, F.** 2007, “Validation of the new Hipparcos reduction”, *A&A*, vol. 474, doi:10.1051/0004-6361:20078357, p. 653–664. [4](#)
- Walder, R., D. Folini and SN Shore.** 2008, “3D simulations of RS Ophiuchi: from accretion to nova blast,” *A&A*, vol. 484, doi:10.1051/0004-6361:200809703, p. L9–L12. [11](#)
- Wang, X. et al.** 2009, “Improved Distances to Type Ia Supernovae with Two Spectroscopic Subclasses”, *ArXiv e-prints*. [19.72](#)
- Webbink, RF** 1984, “Double white dwarfs as progenitors of R Coronae Borealis stars and Type I supernovae”, *ApJ*, vol. 277, doi:10.1086/161701, p. 355–360. [9](#)
- Whelan, J. and I. Iben, Jr.** 1973, “Binaries and Supernovae of Type I”, *ApJ*, vol. 186, doi:10.1086/152565, p. 1007–1014. [9](#)
- Wood-Vasey, WM et al.** 2004, “The Nearby Supernova Factory”, *New Astron. Rev.*, vol. 48, doi:10.1016/j.newar.2003.12.056, p. 637–640. [39](#)
- Woosley, SE et al.** 2007, “Type Ia Supernova Light Curves”, *ApJ*, vol. 662, doi:10.1086/513732, p. 487–503. [13](#)